© Copyright 2024

Priti Mulimani

# Investigating Periodontal Mechanobiology at Cellular and Tissue Levels Using Novel *In Vitro* Bioengineering Techniques

Priti Mulimani

A dissertation

submitted in partial fulfillment of the

requirements for the degree of

Doctor of Philosophy

University of Washington

2024

Reading Committee:

Tracy E. Popowics, Co-chair

Nathan J. Sniadecki, Co-chair

Sue Herring

Program Authorized to Offer Degree:

Oral Biology / Oral Health Sciences

University of Washington

**Abstract**

# Investigating Periodontal Mechanobiology at Cellular and Tissue Levels Using Novel *In Vitro* Bioengineering Techniques

Priti Mulimani

Co-chairs of the Supervisory Committee:

Tracy E. Popowics
Oral Health Sciences

Nathan J. Sniadecki
Mechanical Engineering

The periodontal ligament (PDL) is a specialized connective tissue, that anchors teeth to alveolar bone lining the tooth sockets. PDL is crucial for transmitting mechanical loads from teeth to bone during oral functions like mastication. Several mechanical and biochemical regulators like Rho/ROCK signaling and inflammatory cytokines, intersect to regulate periodontal cellular and tissue behavior during health and disease. Hence, research like the current study, that explores the effects of mechanical loads and inflammatory mediators is key to develop clinical interventions for periodontal applications like regeneration and facilitating efficient orthodontic tooth movement. However, the *in vivo* complexity and inaccessibility of human PDL has necessitated the use of *in*

*vitro* models for PDL research. In the present study, aspects of periodontal mechanobiology in both 2- and 3-dimensions have been studied, by employing latest bioengineering advancements to develop multiple novel *in vitro* PDL models. In chapter 2 of this thesis, I investigate the effects of inflammatory cytokine tumor necrosis factor-alpha (TNF-α) with and without the involvement of the Rho/ROCK signaling pathway on single cells using a novel reference free traction force microscopy technique called as 'Black dots'. This chapter also demonstrates the presence of the myofibroblast phenotype with alpha smooth muscle actin stress fibers and details myofibroblast properties and their regulation by TNF-α. These crucial findings highlight the link between TNF-α induced alterations in cells' mechanical and morphometric properties, such as actin cytoskeleton, contractile force and cell area, with functional outcomes like cell differentiation.

Understanding cellular mechanisms at the 3-dimensional (3D) level is necessary to gain insights on cell-cell and cell-matrix cross-talks that are closer to *in vivo* reality. In Chapter 3, I have developed a novel 3D *in vitro* PDL model that reproduces certain key *in vivo* periodontal design features and can be potentially used to test drugs, signaling molecules & various biological agents on the PDL. This model is also equipped to apply tensile loads with built-in magnets, thus providing a platform to test tensile loading effects on PDL as during mastication or orthodontic tooth movement. The expected effects of tensile loading on cell number, collagen remodeling, cytoskeletal changes and osteogenic gene expression are also demonstrated using this model. In Chapter 4, using the suspended tissue open microfluidic patterning (STOMP) system, I have spatially patterned tissue constructs with embedded entheses made up of PDL and osteoblastic cells, as an *in vitro* cellular representation of the *in vivo* PDL-alveolar bone enthesis. This model provides a potentially valuable platform to investigate cell biomechanics, mechanotransduction and tissue behaviour at the junction of disparate cell types. Overall, the current research project showcases three new *in vitro* models that can enable new discoveries in the field of periodontics and orthodontics.

# TABLE OF CONTENTS

# LIST OF FIGURES

# LIST OF TABLES

# ACKNOWLEDGEMENTS

I would first like to thank my advisors, Dr. Tracy Popowics and Dr. Nathan Sniadecki, who took a chance on me and gave me all the support I needed to crossover from my clinical background to the biomedical sciences field and help me grow into the scientist that I am today. Thank you for your tough questions, for your gentle encouragement and for always challenging me to become a better thinker and a scientist. I am truly grateful for the profound positive contributions you have made to help me create my desired professional and scientific career trajectory.

Many thanks to the other members of my supervisory committee, Dr. Sue Herring, Dr. Michael Cunningham, and Dr. Anne-Marie Bollen, for their significant role in navigating me towards the successful completion of my PhD program. Thank you for your faith in me and supporting me through some tough personal challenges I encountered as a graduate student. I am most grateful to my PIs and my supervisory committee for their patience as I whittled down the vision for my research project from an onerous one to a manageable one.

I owe a special thanks to my mentors Dr. Tracy Popowics and Dr. Sue Herring. Dr. Popowics, in addition to being a fantastic professional, scientific and personal role model, I would like to thank you for being my family and friend during my hardships and personal losses that I had to endure during my PhD training. I will be forever grateful for your kindness, care and presence during these crucial times. Dr. Herring, you and your life are a source of eternal joy and inspiration to me. Thank you for your guidance and mentoring throughout this journey. From you I have learnt so many things - the best scientific practices, critical thinking, scientific rigor, history of all things and importantly to have a zest for everything life has to offer and to enjoy the ride! I am incredibly grateful that life made our paths cross, and that I had the privilege of learning from you and spending time with you.

To all the members of the Cell Biomechanics Lab past and present, thank you for your being a fantastic scientific community to learn from, to collaborate with and to grow in. I am grateful for your camaraderie and for your scientific inputs that helped me develop protocols, refine techniques and troubleshoot issues. These people include Dr. Kevin Beussman, Dr. Molly Mollica, Dr. Samantha Bremner, Dr. Deema Alroweilly, Ty Higashi, Alex Goldstein, Thomas Leahy, Ruby Padgett, Ava Obenaus, Michael Malone and Trevor Mollot.

I am incredibly thankful for my under-graduate research assistant, Natalie Mazzawi, who was instrumental in assisting me with several experimental techniques and data analyses. Natalie, I admire you for all the skill, efficiency, professionalism and work ethics you embodied. I couldn't have asked for a better team member to lean on, professionally and personally, during this arduous journey. It was a privilege working with you and interacting with a human as wonderful as you. I am also grateful to my under-graduate research assistant, Oren Koefler, who was pivotal to assist me with experiments during the crucial dissertation writing phase. Oren's joie-de-vivre and infectious enthusiasm for research always reminded me of my own love for science and how worthwhile undertaking this journey was.

I am very thankful for getting the opportunity to work with and learn from amazing collaborators and scientists in the ISCRM community. Thank you to Lauren Brown and Amanda Haack from the Theberge lab for collaborating with me to develop novel modalities of research for my PhD project. I am incredibly grateful to Dr. Dale Hailey, Director of the ISCRM Garvey imaging core for training me on various imaging techniques and for troubleshooting when needed. A special thanks to Wei Ming Chien from the Yang Lab for helping me with several assays, techniques and troubleshooting. I am also very grateful to Drs. Ron Kwon and Daniel Yang for their invaluable professional advice, mentorship and career guidance that I truly appreciated.

I have been very fortunate to have been supported by an exceptional community in the Oral Health Sciences department who have been invaluable sources of resources, guidance and mentorship. The following is an incomplete list of these individuals: Dr. Kristopher Kerns, Dr. Sun Oh Chung, Dr. Robert Cornell, Dr. Douglas Ramsay, Dr. Richard Presland, Dr. Donald Chi, Dr. Jeffrey McLean, Dr. Cameron Randall, Dr. Jonathan An, Lora Brewsaugh, Maggie Dean, Natascha Trias, Julianna M. Duso and Wendy Kramer.

Lastly and most importantly, my deepest gratitude and boundless love to my beloved family – my Dad, my Mom and my sister. And to my beloved close friends who stood by me throughout this journey. Your unwavering love and steadfast support keep me going and make it all worthwhile.

# DEDICATION

*In loving memory of my extraordinary Dad*

# CHAPTER 1. INTRODUCTION

## 1.1 PERIODONTAL LIGAMENT AND NEED FOR MECHANOBIOLOGY RESEARCH

The periodontal ligament (PDL) is a specialized, fibrous connective tissue, interposed between the outermost cementum layer surrounding tooth roots and alveolar bone lining the tooth socket. It is encased within a mostly hour-glass shaped space, ranging from 150-400 microns in width and is highly vascularized and innervated (Nanci 2012). The PDL's extra-cellular matrix (ECM) is richly embedded with a heterogenous cell population that includes fibroblasts, osteoblasts, osteoclasts, epithelial cell rests of Malassez, monocytes, macrophages, undifferentiated mesenchymal stem cells (MSCs), cementoblasts and odontoclasts (Figure 1.1) (Marchesan et al. 2011, Nanci 2012). The ECM consists of well-defined collagen fiber bundles embedded in an amorphous ground substance composed of proteoglycans, glycosaminoglycans and glycoproteins. PDL collagen is of predominantly types I, III and XII. A unique feature of the PDL is that the collagen fibrils are arranged in definite and distinct fiber bundles, which are continuously remodeled to adapt to the perpetual mechanical stresses they are exposed to. Collagen bundles that extend from their insertion into the root cementum to their insertion into the alveolar bone, are referred to as the principal fiber bundles of the PDL (Figure 1.1, B).

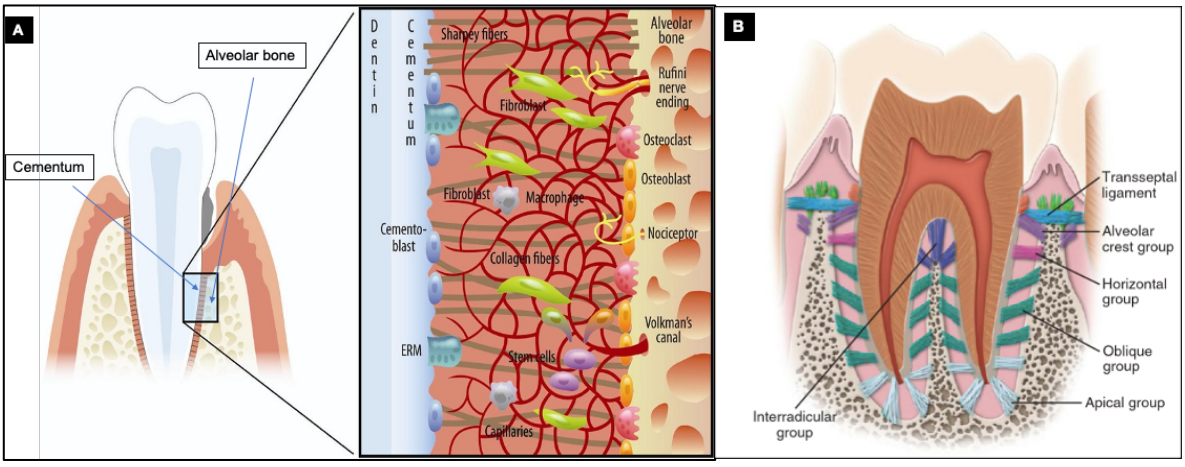


**Figure 1.1. Schematic of PDL.** (**A**) Structure & composition of PDL. ERM – epithelial cell rests of Malassez (Image from Marchesan et al. 2011). (**B**) Principal fiber bundles of PDL (Image from Nanci 2012).

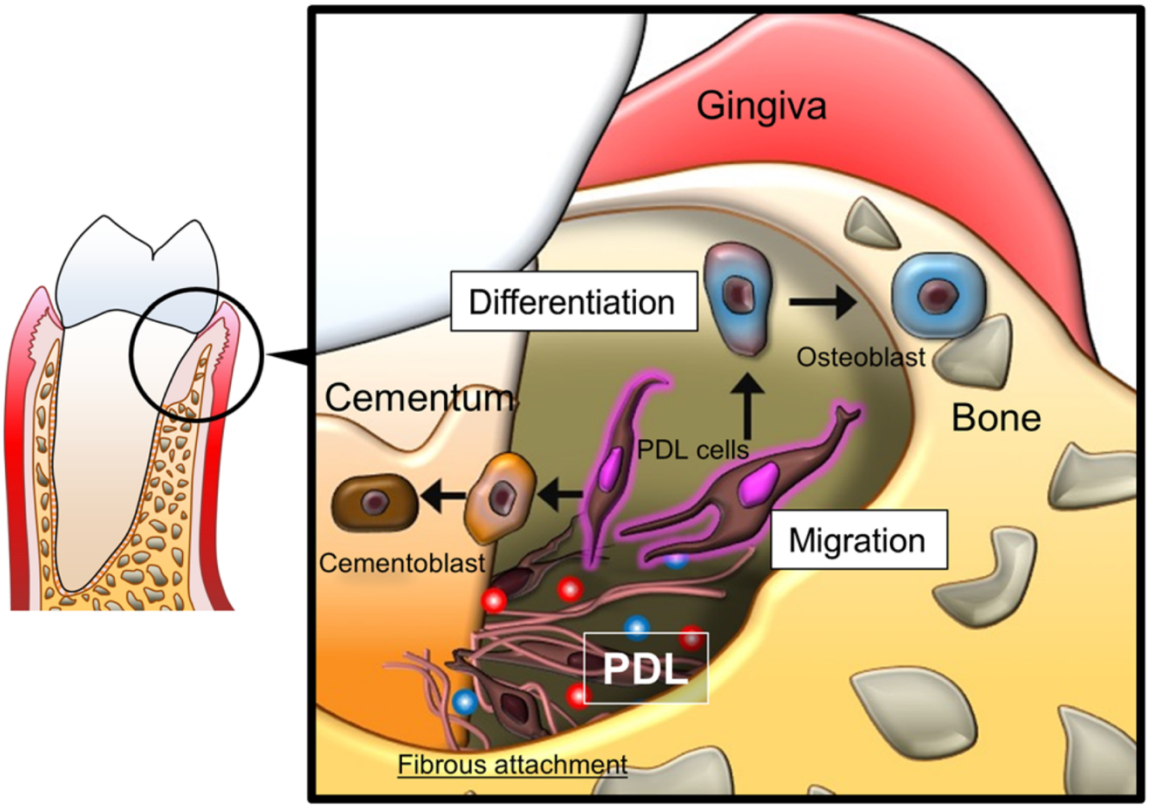


**Figure 1.2. Schematic of main PDL cell types in the three layers of periodontium.** (Image from Yamamoto et al. 2018).

PDL is the main conduit for transmission of mechanical loads arising from crowns of teeth in the oral cavity due to day-to-day activities like chewing, swallowing or therapeutic interventions like orthodontic treatment, to surrounding bone. A critical feature facilitating the mechanical load processing is the region-specific cell differentiation within the PDL which maintains its structural and functional integrity in health and disease (Figure 1.2). This is especially true when the dentoalveolar socket along with the periodontium is entirely remodeled and translocated during orthodontic tooth movement (OTM) (Meikle 2005). Re-establishing the multi-layered structure of the periodontium while repopulating the PDL layers lost to periodontal disease with the native cell types remains a key but yet unfulfilled goal of periodontal regeneration (Gallie et al. 2021). Additionally, inflammatory mediators like tumor necrosis factor-alpha (TNF-a) disrupt biological processes central for PDL homeostasis, health and function (Nanes 2003). Local increase in TNF-

a levels is commonly seen during a) periodontal disease, b) systemic diseases like diabetes and c) orthodontic treatment with braces (Hotamisligil and Spiegelman 1994, Graves 1999, Papadopoulou et al. 2020). Hence, research that explores effects of mechanical loads and inflammatory mediators is key to develop clinical interventions that will maintain PDL homeostasis, prevent and repair periodontal disease, regenerate periodontium and facilitate efficient OTM.

Investigating the mechanical and biochemical pathways that regulate periodontal cellular and tissue behavior, are essential for developing and improving clinical interventions for periodontal disease. Periodontal disease including periodontitis, destroys periodontal tissues resulting in loosening of tooth within the jaws and eventual loss of teeth. People with periodontal disease face an inability to chew, malnutrition, loss of self- esteem and social interactions, a significantly diminished quality of life and huge healthcare costs. As the 6th most prevalent disease worldwide, periodontal disease is a public health problem afflicting at least 1.1 billion patients globally (Tonetti et al. 2017). Marginalized social groups like Black and Hispanic populations, people living below the federal poverty level (65.4%) and those with less than a high school education (66.9%) are disproportionately affected (Chen et al. 2019, Eke et al. 2020). Additionally, there exists a bidirectional link between periodontal diseases and several systemic conditions like diabetes, Alzheimer's disease, colon cancer, preterm labor etc., which is a cause for serious concern (Pihlstrom et al. 2005). TNF-α is a key mediator involved in periodontal pathogenesis and tissue destruction (Graves 1999). Consequently, understanding the effects of TNF-α on periodontal cells is critical for developing interventions to mitigate its deleterious effects on periodontal health, more so for individuals with pre-existing systemic issues who are more vulnerable for developing periodontitis. Hence, one of the objectives of the current study was to investigate effects of TNF-a on PDL cell structure and function.

Another significant area necessitating biological insights into periodontal response to mechanical loads is orthodontic treatment. Orthodontic treatment with appliances involves application of continues mechanical loads of varying magnitudes, duration and frequency to move teeth and jaws to more desirable positions, for optimal dental function, health and aesthetics. In the United States alone, at least 3.2 million people undergo orthodontic treatment, on which they collectively spend around 17 billion dollars annually (AAO 2017). For a treatment so pervasive among the general public, and on which billions of dollars are being spent, the research into its biological aspects unfortunately has not increased on the same scale. The efficiency, speed, and manner of OTM is a vital clinical issue as patients pay a price for prolonged treatment in terms of costs incurred and more importantly through the dental health risks they are exposed to, such as enamel decalcification, root resorption, periodontal disease, dental caries and loss of tooth vitality (Wishney 2017).

The critical biological factors that determine an individual's periodontal response to applied mechanical loads during orthodontic treatment remain under-investigated. The periodontal response during OTM depends on release of signaling molecules including cytokines, that will resorb bone in the direction of applied force and deposit bone in the opposite direction to remodel the PDL and move teeth to desired positions (Figure 1.3) (Meikle 2005, Graber et al. 2012).

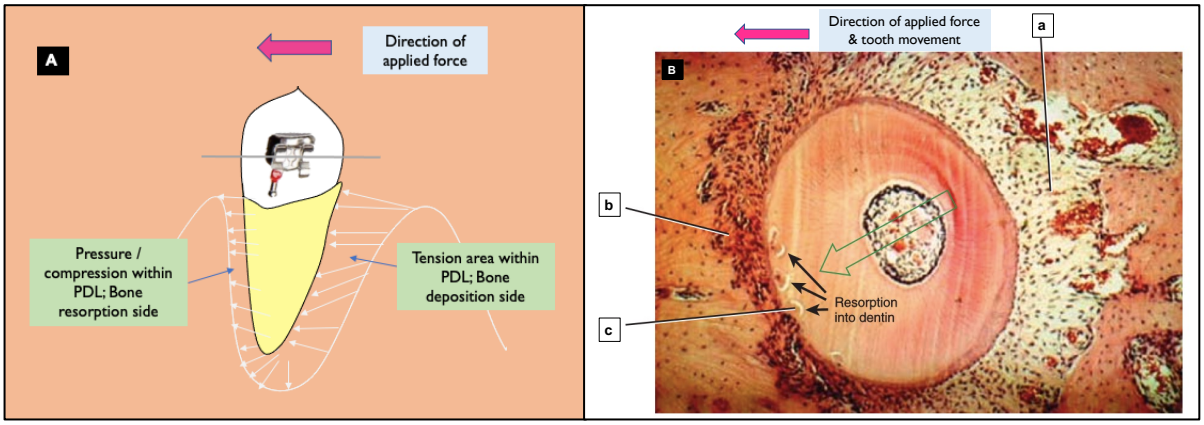


**Figure 1.3. Orthodontic tooth movement (OTM). (A)**<u>*Schematic of pressure and tension areas within PDL on orthodontic force application*</u>**. (B)** Coronal section through root of premolar being moved to left; a –Tension zone, dilation of blood vessels & osteoblastic activity; b- Compression zone, osteoclasts resorbing bone; c-root being resorbed (B- image from Graber et al. 2012)

Clinical studies have demonstrated a variation in expression levels of key cytokines across individual patients and linked them to clinical response. Equivalent orthodontic forces caused a higher and more sustained production of TNF- α and IL-1 β in adults compared to adolescents, which also correlated with higher levels of pain, discomfort and slower tooth movement in adults (Alikhani et al. 2018). Additionally, individuals with faster tooth movement were found to possess a specific genotypic variant of IL-1β (Iwasaki et al. 2005, Iwasaki et al. 2006). There also exist variations in gene expression across individuals, due to individual heterogeneity of the relative proportions of different cell types within the same tissue (Xu et al. 2011). Even within individuals of the same population under identical environmental conditions, 18-48% genes were found to be differentially expressed (Whitehead and Crawford 2005, Oleksiak 2002). Undoubtedly, this link between variation in production of biological mediators, link with specific genetic variants and their association with clinical outcomes like rate of tooth movement and pain experienced during treatment are crucial factors yet research on them is scant. Identifying these variations at the molecular level remains the pivotal first step needed to address the unexplained adverse tissue reactions, refractory tissue behavior and unexpected treatment response experienced in clinical orthodontics. Identification of variations would also eventually help in developing a personalized diagnostic approach and treatment plan for each patient based on their comprehensive molecular and tissue response profile. Thus, identifying donor-dependent variations in PDL behavior at tissue and cellular levels, holds the key to precision orthodontics. Developing a thorough understanding of periodontal mechanobiology is central towards this endeavor.

## 1.2 PERIODONTAL MECHANOBIOLOGY

Study of the underlying biological processes in response to external mechanical forces is referred to as the “mechanobiology”. A critical aspect of periodontal mechanobiology is to understand the link between mechanical force induced changes in biomechanical properties such as cell shape, area, cytoskeletal contractility, and activation of biochemical signaling pathways responsible for

downstream regulation of cellular functions. PDL mechanobiology encompasses three main biological processes (Figure 1.4) (2005, Vogel and Sheetz 2006) - i) mechanosensing – applied mechanical forces cause local perturbations such as ECM deformation and conformational changes in cell surface receptors, ion channels, cell membrane etc. activating downstream intracellular cascades for mechanical force transmission, ii) mechanotransduction – force effects are transmitted via the mechanosensors to the nucleus either indirectly through signaling pathways associated with or directly via physical perturbations of the cytoskeleton and nucleoskeleton and iii) mechanoresponses – mechanotransduction-induced intra-nuclear forces or transcription factors modify the genome and cause gene expression changes that drive mechanoresponses like cell proliferation, differentiation, migration and function.

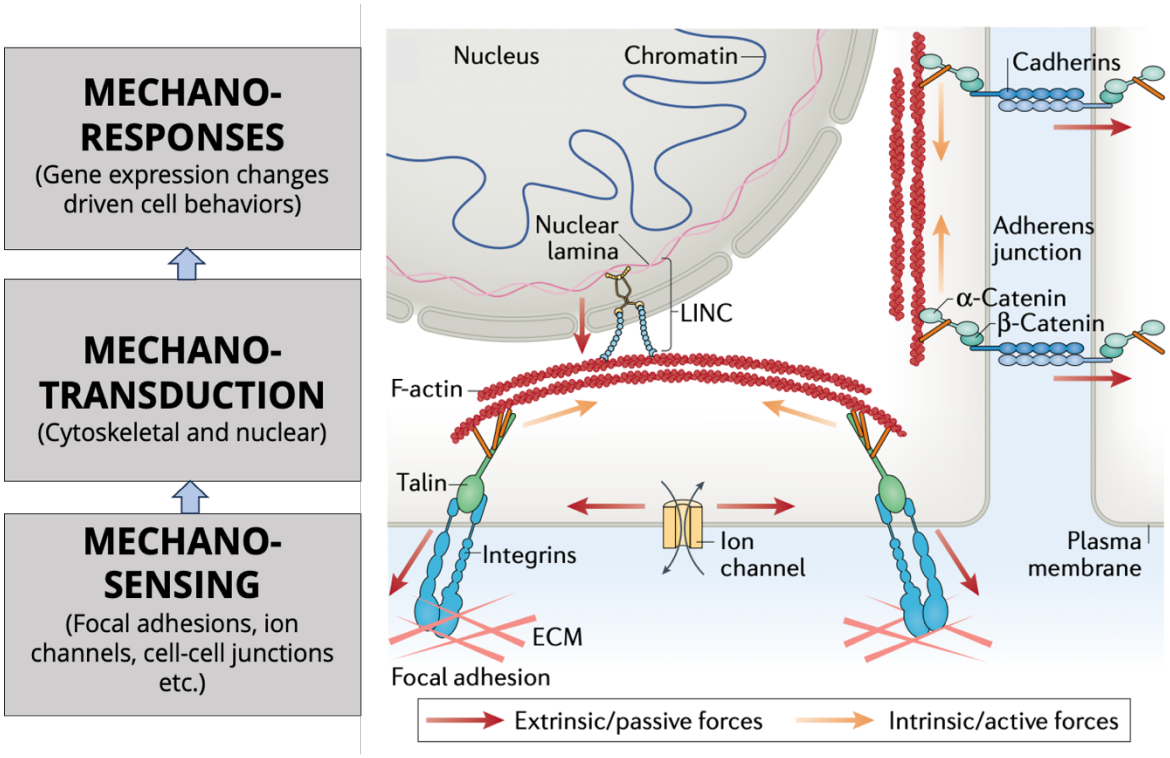


**Figure 1.4. Biological processes in periodontal mechanobiology**. Extrinsic forces propagate to the actin cytoskeleton through adhesion complexes (focal adhesions and adherens junctions) and to nucleus via linker of nucleoskeleton and cytoskeleton (LINC) complexes. External forces can also be mechanotransduced via several mechanosensitive plasma membrane structures like receptors, ion channels and signaling modules that trigger downstream mechanoresponses. All the while, the processes activated by extrinsic forces are also interacting with, modifying and getting regulated by the intrinsic cytoskeletal forces produced by cells through their actin cytoskeleton contractility (Figure adapted from Romani et al. 2021).

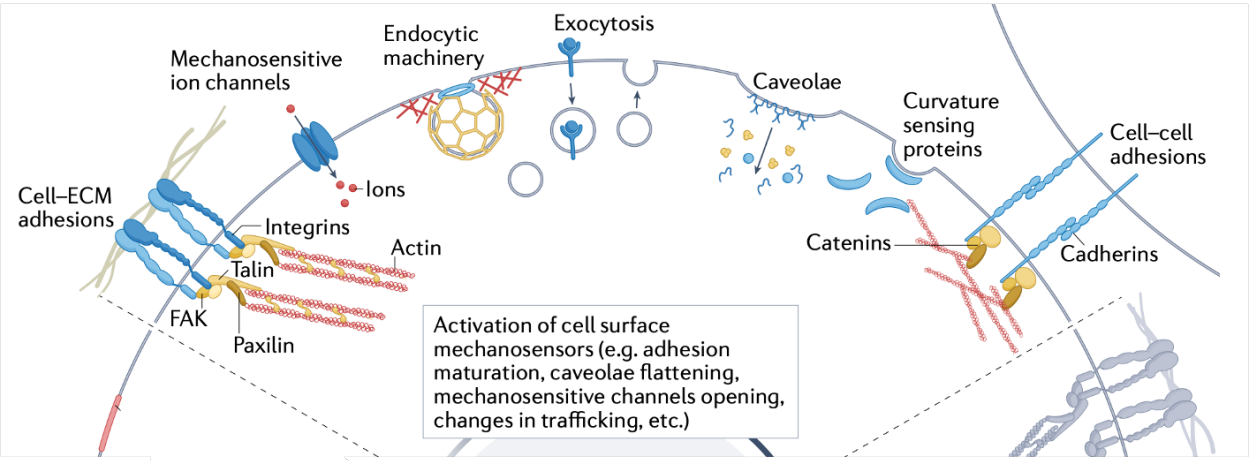


**Figure 1.5. Cellular mechanosensors** (Image from De Belly et al. 2022).

*i) Mechanosensing:* Mechanical loads activate several mechanosensitive cell surface molecules like ion channels, receptors, adhesion complexes, trafficking complexes etc., which are referred to as mechanosensors (Figure 1.5) (De Belly et al. 2022). Among these, transmembrane receptors like integrins and protein complexes like the focal adhesions (FAs) that attach to the actin cytoskeleton comprise a crucial cellular mechanism for sensing biomechanical changes in the ECM. Integrins are heterodimeric receptors with several isoforms composed from an alpha and beta subunit each. Eight β subunits can interact with 18 α subunits to form 24 distinct integrins, which can be classified into several subfamilies based on their ECM ligand specificity (Kechagia et al. 2019). Periodontal cells mainly express integrin α2β1, α3β1, and α5β1, whereas this pattern can change under disease conditions (Jakhu et al. 2018).The cytosolic domains of integrins form a complex with actin-associated cytoskeletal proteins like talin, vinculin, alpha-actinin and paxillin (Kanchanawong and Calderwood 2023). These complexes further associate with F-actin and kinases like focal adhesion kinase (FAK) and Src family kinases to give rise to FAs (Figure 1.6., A). FAs thus aid in cellular mechanosensing by forming a complex of supporting proteins that connect actin cytoskeleton to ECM components like fibronectin,

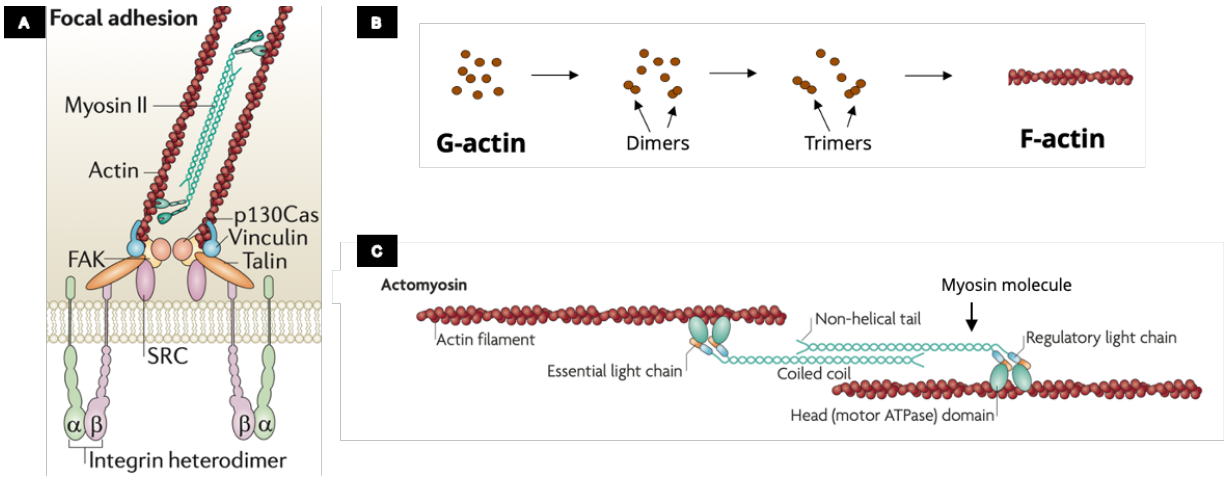


**Figure 1.6. Structure of focal adhesions and actomyosin molecule.** (**A**) Focal adhesion structure. FAK-focal adhesion kinase. (**B**) Polymerization of monomeric globular actin (G-actin) into filamentous actin (F-actin). (**C**) Myosin heads bind with F-actin filaments to form actomyosin constituted stress fibers in a cell. Actomyosin bundles generate cellular forces necessary for adhesion, survival, differentiation, migration, cell division, morphogenesis etc. (Image elements adapted from Vicente-Manzanares et al. 2009.)

vitronectin, collagens, laminins via integrins. The actin filaments attached to FAs are in the form of stress fibers, made up of contractile actomyosin structures created by pulling of myosin II motor heads on actin filaments (Figure 1.6., B, C). Cytoskeletal contractility mediated by actomyosin bundles is a key determinant of cell-ECM interactions and cellular parameters like shape, spread, area and phenotype. Cellular contractile forces generated via actomyosin contractility are involved in at least 49 distinct cellular functions that range from providing cell architecture to signal transduction and nuclear activity (Zaidel-Bar et al. 2015). Especially, non-muscle myosin II (NMMII) is thought to be key for environmental mechanosensing and generating cytoskeletal force. When NMMII was inhibited, substrate stiffness failed to influence cell phenotype, indicating the necessity of the contractile apparatus to sense ECM changes and respond to environmental cues (Pellegrin and Mellor 2007). Mechanosensing by cellular structures like FAs and actomyosin bundles, is effectuated into responses such as cell fate and function determination, by the mechanotransduction process.

*ii) Mechanotransduction:* Mechanical stimuli mediated alterations in cellular FAs and actin cytoskeleton trigger downstream mechanotransduction pathways that continue processing the mechanical loads into biological signals. The Ras homologous (Rho)/Rho associated protein kinase (ROCK) pathway is key for the conversion of mechanical cues from the ECM into biological signals via cellular cytoskeleton (Figure 1.7). The Rho family belongs to the small GTPases protein family that have inherent GTP hydrolytic enzymatic activity. They function as molecular

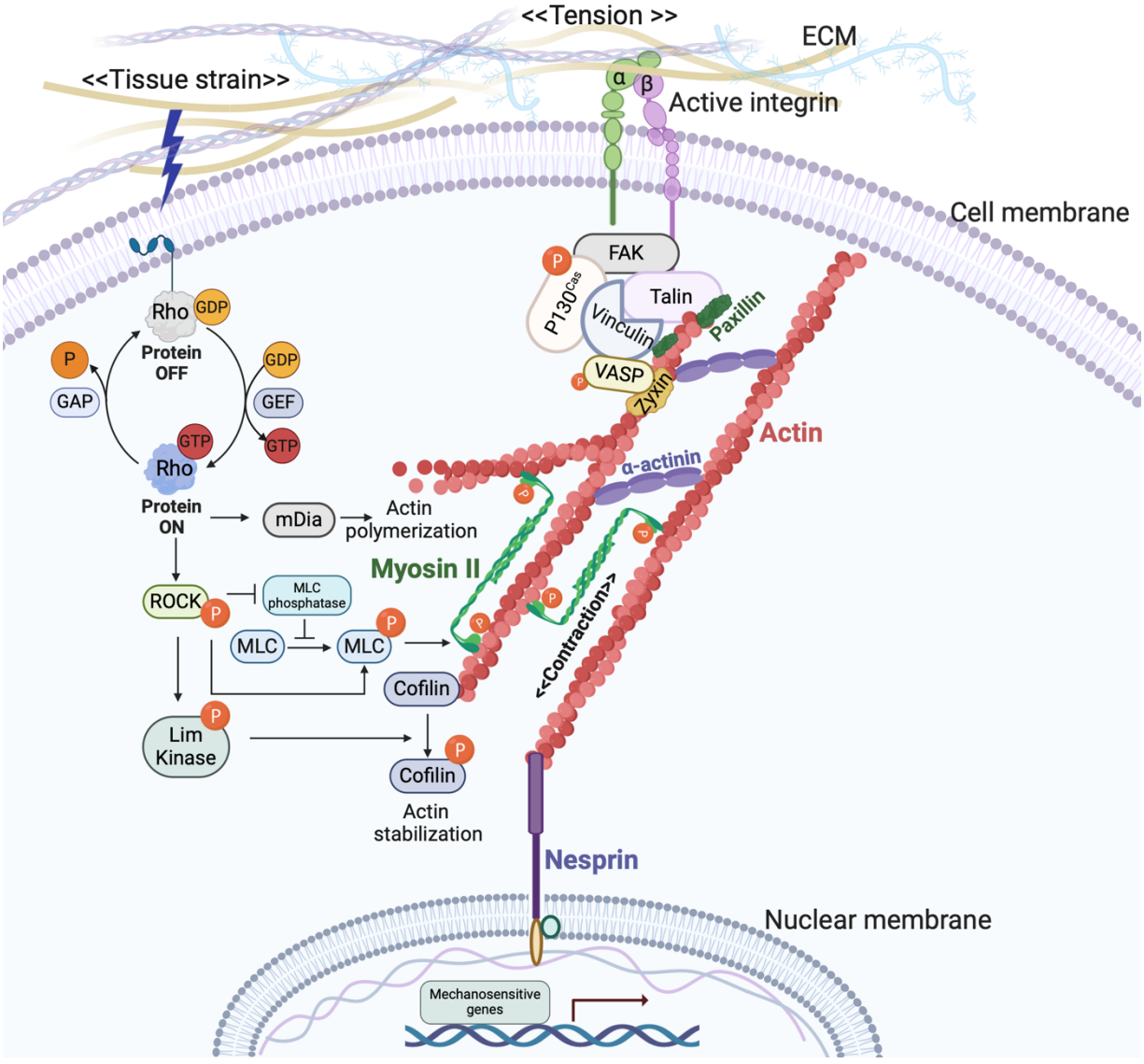


**Figure 1.7. Schematic representation of cellular mechanotransduction via Rho/ROCK pathway.** FAK, focal adhesion kinase; mDia, Diaphanous-related formin-1; MLC, Myosin light chain; ROCK, Rho-associated protein kinase; VASP, vasodilator-stimulated phosphoprotein (Figure created using BioRender and adapted from Putra et al. 2023).

switches in the cell to turn on or off several intracellular signaling pathways by cycling between a GDP-bound, inactive state and a GTP-bound, active state. The activated Rho-GTP binds to specific targets and exerts its biological function until it inactivates itself by hydrolysis of GTP to GDP through its inherent enzymatic action when triggered by GTPase-activating proteins (GAPs). The molecules are activated again when guanine nucleotide exchange factors (GEFs) replace the GDP in the GDP-bound inactive with GTP.

When bound to GTP, Rho activates the kinase ROCK which increases actomyosin assembly and contractility through following mechanisms (Vicente-Manzanares et al. 2009, Martino et al. 2018)-

a. phosphorylates NMMII light chain and activates myosin

b. inhibits myosin-light-chain phosphatase (MLCP) by phosphorylating it; function of MLCP is to inhibit phosphorylation of NMMII light chain required for its activation

c. phosphorylates and activates LIM-kinase; phosphorylated LIM-kinase in turn phosphorylates and inactivates cofilin, which will prevent the breakdown and recycling of actin filaments, maintaining the integrity of the actomyosin stress fibers.

This enhanced actomyosin contractility mediated by ROCK modifies cell shape and spreading, which have been shown to determine cell behaviour, function and fate. McBeath et al., (2004) demonstrated that the shape-dependent control of lineage commitment was dependent on an intact cytoskeleton and mediated by RhoA activity in the Rho/ROCK pathway, specifically via its effects on ROCK-mediated cytoskeletal tension. High levels of ROCK-mediated cytoskeletal tension correlated to spread cells and osteogenic conditions and low levels to rounded cells and adipogenic conditions even in the absence of soluble differentiation factors. In PDL cells (PDLCs), cyclic mechanical strain was found to activate the Rho/ROCK pathway which upregulated cytoskeletal remodeling (Pan et al. 2014). Inactivation of ROCK was shown to direct PDL cells to an adipogenic fate whereas activation led to an osteogenic fate through two mechanisms – a) direct activation of osteogenic molecules and b) indirect activation of osteogenesis by

upregulating phosphorylated myosin light chain 2 (MLC2)-mediated cytoskeletal contractility and tension (Yamamoto et al. 2018). Such changes in cell fate and behavior, referred to as mechanoresponses, are mediated by gene expression changes explained in the section below.

*iii) Mechanoresponses:* Mechanical signals transduced by mechanotransduction pathways are transmitted to the nucleus either by soluble factors or by mechanical coupling of cytoplasmic structural elements with the nuclear membrane (Figure 1.8). This leads to downstream events like intra-nuclear epigenetic modifications in the chromatin and/or activation or inhibition of transcription factors. The consequent gene expression changes then accordingly regulate cell proliferation, differentiation, migration and function, collectively referred to as mechanoresponses. In PDLCs, activation of the Rho/ROCK pathway by mechanical stresses has been associated with osteogenic gene expression and osteoblastic differentiation through the following two mechanisms –

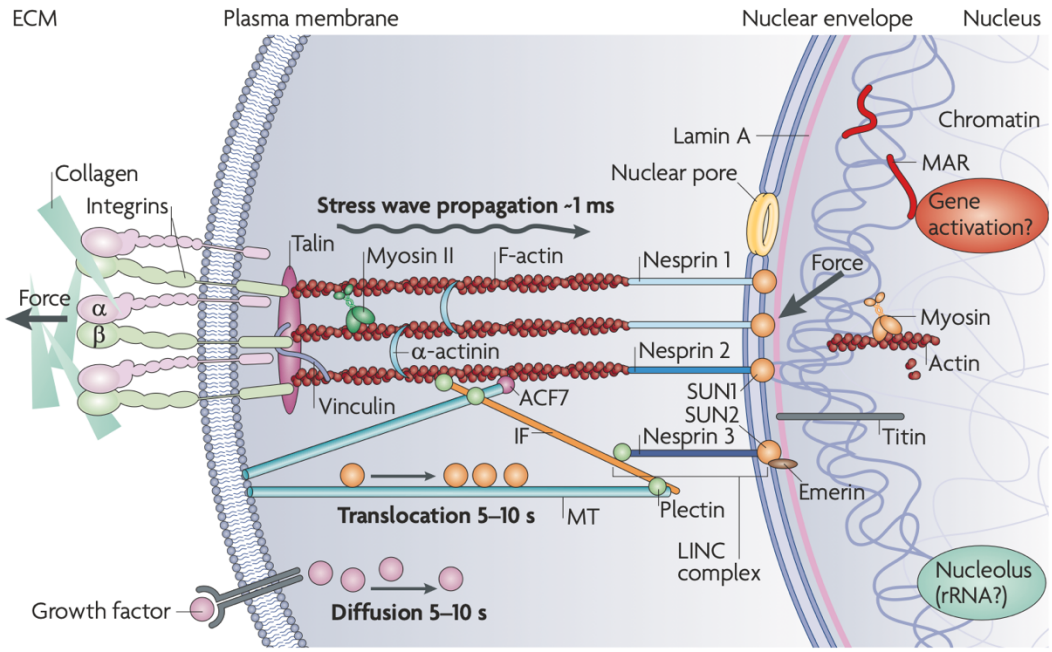


**Figure 1.8. Schematic representation of nuclear mechanotransduction and mechanoresponses.** Cytoplasmic F-actin is linked to nuclear membrane proteins like SUN, Nesprin and LINC complex which in turn connect with chromatin and DNA. Force transmission to the nucleus may occur via the cytoplasmic-nuclear cytoskeletal network rapidly in milliseconds or slowly in seconds via soluble signaling factors. (Figure from Wang et al. 2009).

a) ROCK- mediated activation of mechanoresponsive cotranscription factors Yes-associated protein 1 (YAP1) and transcriptional coactivator with PDZ motif (TAZ) (Yamamoto et al. 2018)

b) Rho/ROCK signaling linked expression of osteogenic molecules, like osteopontin, activator protein-1 and receptor activator of nuclear factor-kappa B ligand (RANK) (Kletsas et al. 2002, Yamashiro et al. 2007, Wongkhantee et al. 200, Hong et al. 2010, Pan et al. 2014).

Together, the transmission of biophysical cues from cytoskeleton and biochemical signaling from soluble signaling factors (Figure 1.8), co-regulate cellular response to mechanical loads. However, cytoplasmic viscosity lowers the rate of signal transmission by soluble signaling factors to seconds as compared to transmission via the cytoskeletal network that occurs rapidly in about a millisecond (Wang et al. 2009). The role of soluble factors in periodontal biology has been extensively studied, while emphasis on the role played by cytoskeletal component has been increasing only in recent times. Hence, this chapter will focus more on the cytoskeletal component and its role in altering cellular responses related to periodontal mechanobiology.

## 1.3 ACTIN CYTOSKELETON AS A REGULATOR OF CELL FATE AND FUNCTION

The cell cytoskeleton is a critical intermediary for transmission of mechanical cues from the ECM to the nucleus. Cytoskeleton-induced mechanotransduction of forces into biological signals is mediated by the Rho/ROCK pathway. Application of cyclic mechanical strain to hPDLCs was found to activate the Rho/ROCK pathway which upregulated cytoskeletal remodeling (Pan et al. 2014). In addition to ROCK-mediated contractility, ECM stiffness, also referred to as matrix elasticity, is also a critical determinant of cellular properties like cell shape, contractility and tension. In the presence of low resisting forces or soft ECM, the intracellular domain of integrin is loosely attached to F-actin forming transient focal points (Figure 1.9). As substrate resistance or

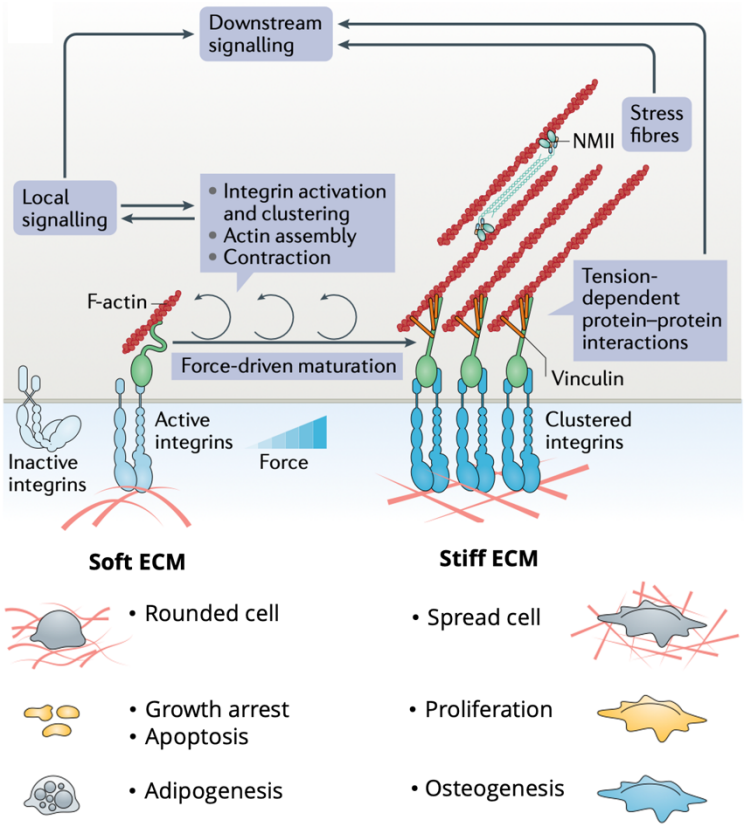


**Figure 1.9.** Effect of substrate stiffness on FA recruitment, stress fiber formation and cell shape, behavior and fate. (Figure adapted from Romani et al. 2021).

stiffness increases, local signaling via FAKs and SRCs causes integrin clustering and eventually adapter proteins like talin, vinculin etc. promote assembly of thicker F-actin and formation of actomyosin contractile bundles at focal adhesion sites (Romani et al. 2021). Thus, stiffer ECMs offer greater grip to outwardly pulling FAs, compared to inherent cytoskeletal tension, causing cells to spread over a wider area and assume a flatter shape. Deformability of softer substrates does not provide the same level of anchoring for the FAs, causing them to move closer in response to the greater inward pull of internal cytoskeletal tension, thus reducing cell spread area that leads cells to round up (Sims et al. 1992). Such cell shape changes determine cell survival. Cells that were allowed to spread underwent growth and dedifferentiation whereas those that were constrained to remain rounded in culture underwent either apoptosis or differentiation (Chen et al. 1997).

Mechanosensing environmental stiffness through elements like FAs and integrins, also causes cells to self-regulate their shape through modifications in cytoskeletal contractility and thus influence their own lineage specification. Engler et al (2009) found that when MSCs were seeded on cross-linked gel matrices of varying stiffnesses, they differentiated into the cell type

corresponding to the native tissue whose elasticity was matched by the substrate stiffness. For example, cells seeded on soft matrices that mimicked brain (< 1 kPa) differentiated into neurons, those on stiffer, muscle-mimicking matrices (~ 10 kPa) differentiated into myocytes, and those on comparatively rigid matrices that mimicked collagenous bone (~ 30 kPa), differentiated into osteoblasts. Independent of ECM stiffness, McBeath et al (2004) by using a micropatterning technique to modify cell shape, identified cell shape as a key regulator of human mesenchymal stem cells (hMSCs) commitment to the osteoblast or adipocyte lineages.

The shape-dependent control of lineage commitment was found to be dependent on the actin cytoskeleton and ROCK-mediated actomyosin contractility (McBeath et al. 2004). Distinct hallmarks of actin cytoskeletal structure have been found associated with cell phenotype (Putra et al. 2023). Yourek et al. 2007 found long, thin, parallel stress fibers in undifferentiated hMSCs, which transformed into robust, criss-crossed thicker stress fibers when differentiated into osteoblasts (Figure 1.10). High density and prominent actomyosin stress fibers were similarly found in osteoblasts resulting from PDL cells treated with osteogenic induction media by

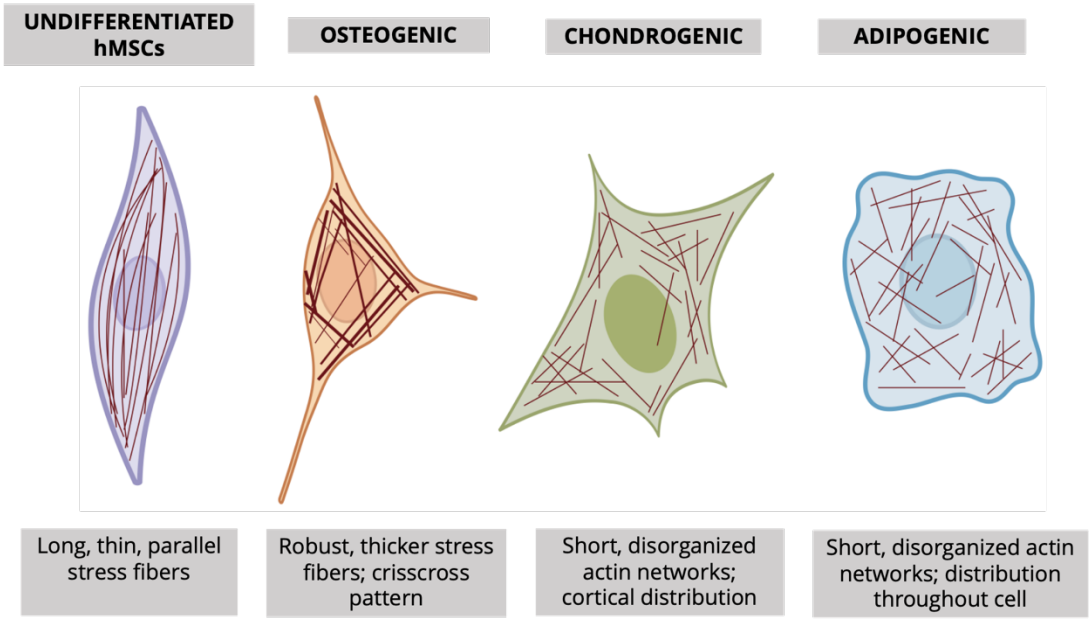


**Figure 1.10. Phenotype-specific stress fiber characteristics.** (Figure created using BioRender and adapted from Putra et al. 2023).

Yamamoto et al. 2018. Untreated control PDL cells in this study also had thinner and parallel aligned F-actin stress fibers. Thicker actin filaments in differentiated mesenchymal stem cells (MSCs) and thinner, parallel filaments in undifferentiated MSCs have similarly been observed in other studies as well (Rodriguez et al., 2004; Arnsdorf et al., 2009). These studies have shown that such stress fiber structure and osteogenic differentiation are caused by activation of the Rho-ROCK pathway. During chondrogenic differentiation, Tvorogova et al., (2018) detected reorganization of actin into a chaotic network of thin cortical fibers. Whereas adipocytic differentiation was favored by cells with a less-organized and less-stiff actin stress fibers (McBeath et al. 2004, Mathieu et al. 2012).

In very high mechanically active environments, in addition to dimensional changes of actin stress fibers, there is a qualitative change in their composition as well. Specifically, the usual beta- and gamma-isomers in stress fibers of non-muscle cells get replaced by the alpha variant characteristic of smooth muscle cells, known as alpha-smooth muscle actin (aSMA). Fibroblasts in which aSMA gets localized to the stress fibers undergo phenotypic conversion to a highly contractile myofibroblast cell type (Figure 1.11). Distinct morphological and biomechanical features associated with each stage of the myofibroblast phenoconversion process are depicted in Figure 1.12

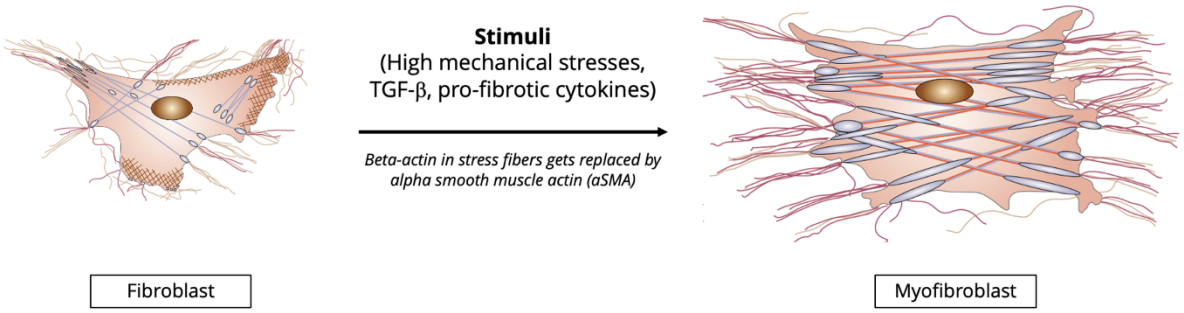


**Figure 1.11. Myofibroblast phenoconversion** (Figure adapted from Tomasek et al. 2002).

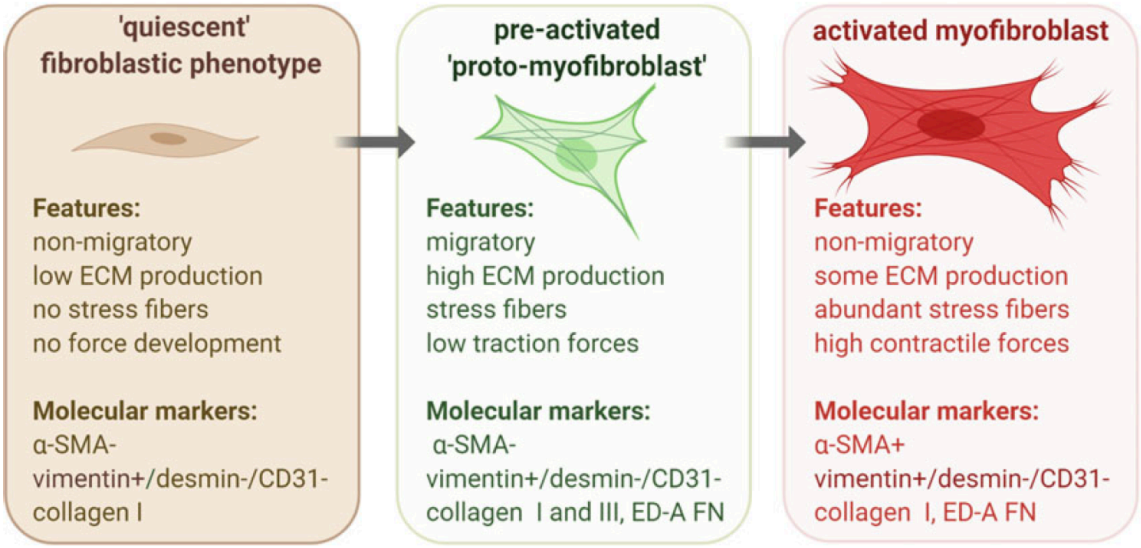


**Figure 1.12. Cellular properties in the myofibroblast conversion spectrum.** αSMA – alpha smooth muscle actin; ED-A FN – Fibronectin domain ED-A. (Figure from Hinz 2016).

Myofibroblast differentiation is mediated by high mechanical tension and by the transforming growth factor- beta 1 (TGF-β1) pathway. Myofibroblast differentiation is commonly seen in areas of high tension found during wound healing and tissue repair (Tomasek et al. 2002). *In vivo* studies on mice periodontium have demonstrated that aSMA expressing cells are in fact progenitor cells, which can differentiate into osteoblasts, cementoblasts, and periodontal ligament fibroblasts (Meng et al. 2010, San Miguel et al. 2010, Roguljic et al. 2016, Matthews et al. 2020). Orthodontic tooth movement studies also found high levels of aSMA positive cells on the tension side of tooth movement in a rat model (Meng et al. 2010). In an extensive molecular and genetic investigation of a-SMA expressing cells, an investigation established that expression of aSMA is not simply a marker for myofibroblast activation, but it is also the driver of cell function and fate (Talele et al. 2015). Thus, aSMA stress fibers act as crucial mechanosensors and aSMA mediated contraction plays a critical role in mechanically regulating stem cell fate and differentiation.

## 1.4 *IN VITRO* MODELS FOR STUDYING PERIODONTAL MECHANOBIOLOGY

Due to the sheer number of biological pathways and mediators involved, and their complex inter-relationships, the study of periodontal mechanobiology becomes very challenging. For *in vivo* study, the PDL presents itself as an extremely inaccessible, narrow tissue (150 to 380 microns), confined between two hard tissues – bone and cementum. It is not possible to directly measure real time PDL changes in live subjects as non-destructive measurement techniques are unavailable. Additionally, PDL is not only heterogeneous in composition and material properties, but it also varies widely across individuals, age, tooth type, root anatomy and different areas within the same tooth. This adds an extra layer of complexity to the unknown biological patient variables that exist *in vivo*. As a result, investigators commonly use animal models, *in vitro* models, or finite element biomechanical models in PDL research.

*In vitro* PDL models have been extensively used in periodontal research to investigate cellular response to mechanical loading (Li et al. 2019). They provide a valuable platform for reducing a complex phenomenon like OTM to a single, isolated variable for the purpose of hypothesis testing, referred to as experimental reductionism. They can also be used for developing diagnostic tools and testing therapeutic agents on the PDL. *In vitro* models based on human cells offset some disadvantages of animal models, findings from which may often be not directly comparable with humans due to differences in tissue physiology and growth rate (Mulimani and Popowics 2019). The two-dimensional (2D) models that have been used extensively thus far consist of a cellular monolayer growing in a petri dish or culture plate which is subjected to tensile or compressive loads by an attached electronic mechanical testing device (Yang et al. 2015, Li et al. 2019). Since mechanotransduction is vastly dependent on the ECM-integrin-actin cytoskeleton attachments which are multi-dimensional, a three-dimensional (3D) model could be considered more biomimetic and its results more representative of the *in vivo* responses. Kang et al. (2013) found that though there were no inherent gene expression differences at baseline between 2D and 3D

cultures, on mechanical stimulation the 3D model was found to be more sensitive, thus responding in a faster and more extensive manner than 2D cultures. They attributed this to the observation that since intercellular and/or cell-to-matrix attachment played an important role in cellular mechanotransduction, the 3D environment allows rapid regulation of the cellular response to mechanical stimulus.

A 3D model not only provides a reproducible, controlled microenvironment that mimics *in vivo* conditions, but also lends itself to modification of the complex variables for experimentation, which is not possible *in vivo*. A 3D tissue model also recreates a differential gradient of signaling molecules similar to *in vivo* conditions, arising due to molecular diffusion which is dependent on the thickness of tissues and point of origin of the signaling molecules within the tissue (Griffith and Swartz 2006). It is especially important to understand this spatial gradient in relation to the point of origin of stimulus (ex. compressive strain or tensile strain) with respect to OTM, as orthodontic force is known to create intermingling areas of compressive and tensile strains within the PDL (Melsen et al. 2007). How bone resorbs in the direction of tooth movement despite having conflicting areas of compressive strain which is osteoresorptive and tensile strain which is osteoproliferative in close proximity, has not yet been resolved in orthodontic research. To address such questions, *in vitro* models provide a valuable platform to explore the spatial and temporal gradients of the molecular response to different types of stresses and assess how they co-operate with or cancel each other out. Additionally, externally applied mechanical loads can be carefully calibrated in an *in vitro* model to determine optimal force levels that will generate the appropriate osteogenic or osteoclastic response for clinical application.

7

Significant advances in tissue engineering and biofabrication techniques have led to development of newer models like organ-on-a-chip, and 3D printed prototypes (Aveic 2021). Of late, 3D *in vitro* models are also being considered as complementary to and even as a valid alternatives for animal models (Koledova 2017, Jensen 2020). *In vitro* models also have the added advantage of being amenable to genetic manipulation, biochemical analysis, and imaging not possible in animal

models. Current 3D PDL models fall into two categories based on their intended purposes – one for inducing periodontal regeneration and another for testing mechanical loading response. 3D models for PDL regeneration are meant for *in vivo* implantation and consist of PDL cells seeded in either a scaffold-free matrix or scaffold of biomimetic polymers, ceramics, hydrogels or self-assembling peptides (Aveic et al. 2021). For mechanical testing, PDL cells have been variously seeded in a matrix of collagen, hyaluronan, gelatin, and type I collagen within receptacles, in an attempt to recreate a 3D inter-relationship between cells and ECM (Yang et al. 2015). A model based on poly-lactic-co-glycolic acid (PLGA) scaffold, thought to have physical characteristics more similar to PDL, was also designed to replace collagen-based scaffolds (Li et al. 2016). Despite the importance of 3D architecture in the cross-talk between cells, ECM and collagen fibers, a 3D PDL model that incorporates the principal fibers has not been attempted to a satisfactory extent until now. Such a model can be expected to provide a more accurate response of PDL cells to local biomechanical cues and their activation of signaling pathways. One of the goals of the current research project will be to bioengineer a biomimetic *in vitro* 3D PDL model and devise a method to study effects of mechanical loading on the model. By applying novel bioengineering techniques, periodontal mechanobiology can be investigated at both single cell and 3D tissue levels. This was accomplished in the current research project by executing the specific aims in the next section.

## 1.5 DISSERTATION SPECIFIC AIMS

**Specific Aim 1: Determine the effect of TNF- α and Rho/ROCK pathway on contractility and osteogenic differentiation potential of donor PDL cell populations in single cells**

TNF-α is a multi-functional cytokine with a wide-range of biological activities in different organ systems. It is produced within the PDL during OTM and in periodontal disease where it has been demonstrated to have pro-inflammatory and osteoresorptive effects. On a cellular level, TNF-α

was shown to upregulate actin stress fiber formation via Rho/ROCK pathway in hPDLCs, which in turn inhibited their migration. However, the effect of such TNF-α mediated upregulation of actin cytoskeleton on hPDLC morphology, biomechanical properties such as contractile force and cytoskeletal composition and their association with the osteoinhibitory effect of TNF- α remain unknown. Hence, the objective of this aim was to quantify TNF-α mediated modifications in cellular cytoskeleton, contractile properties and osteogenic potential. The hypothesis was that TNF-α would increase cytoskeleton formation, cellular contractility and stimulate osteogenic differentiation of PDL cells. Chapter 2 details these effects of TNF-α with and without the involvement of the Rho/ROCK pathway on single cells using the reference free traction force microscopy technique – the 'Black dots' method. These findings are crucial since they link TNF-α induced alterations in cells' mechanical and morphometric properties with functional outcomes like cell differentiation. These findings can have important applications for potential therapeutic interventions that target cellular contractile function to modify osteogenic differentiation in PDL for regenerative or orthodontic purposes.

**Specific Aim 2: To develop a novel 3D *in vitro* model of the PDL and test the mechanobiological response of the 3D tissue constructs to tensile mechanical loading**

The PDL is one of the main conduits for transmitting mechanical loads from dental functions and the sole mechanism to firmly anchor teeth to alveolar bone for life-long functionality. Understanding the molecular and cellular mechanisms that facilitate these periodontal functions is key to prevent and treat periodontal disease and to facilitate therapeutic tooth movement with orthodontics. However, since in its native *in vivo* form the PDL is inaccessible and not amenable for direct experimental investigations, *in vitro* models are indispensable for periodontal mechanobiology studies. Especially the 3D models that recreate the *in vivo* spatial orientation between cells, fibers and other ECM components to closely mimic physiologic mechanotransduction, have thus far been lacking. Hence, this study aimed to develop a 3D

PDL model that reproduces *in vivo* periodontal design features and would also lend itself to mechanobiological investigations. I hypothesized that by seeding patient-derived PDL cells in a matrix of collagen and suspending them between flexible silicone posts with magnet-embedded tips, one can create a 3D *in vitro* tissue construct on which magnetic tensile stretch can be applied. Indeed, chapter 3 describes the successful fabrication of this model and also demonstrates the biological effects of mechanical tensile loading this 3D model with built-in magnets. In this chapter I have demonstrated that the structural arrangement of cells and fibers within the 3D tissue constructs is similar to that found *in vivo*. The expected effects of tensile loading on cell number, ECM remodeling, cytoskeletal changes and osteogenic gene expression are also documented in this chapter.

**Specific Aim 3: To develop a bone-PDL-bone cellular enthesis model of the PDL**

The PDL-bone enthesis is a critical transition zone that facilitates stress distribution and functional adaptation. The interplay between key cell types at this junction determines mechanotransduction and signalling. Cellular events occurring at the PDL-bone enthesis remain under-investigated, partly due to the absence of 3D *in vitro* models. Hence, one of the objectives of this study was to engineer a 3D *in vitro* periodontal tissue construct model with embedded PDL-bone cellular entheses. I hypothesized that by using the suspended tissue open microfluidic patterning (STOMP) system, spatially patterned tissue constructs with an embedded enthesis made up of PDL and osteoblastic cells can be engineered. Chapter 4 details the fabrication and characterization of this STOMP-based cellular enthesis periodontal tissue construct model. Our model provides a potentially valuable platform to investigate cell biomechanics, mechanotransduction and tissue behaviour at the junction of disparate cell types. This model has significant translational potential for periodontal therapeutic and regenerative applications.

## 1.6 REFERENCES

AAO, American Association of Orthodontists. St. Louis, (MO). 2017 Orthodontic Workforce Report (2019). Available at https://webcache.googleusercontent.com/search?q=cache:1QXPMvDJU-8J:https://www.aaoinfo.org/sites/default/files/Orthodontic%2520Workforce%2520Report_April%25202018.pdf+andcd=1andhl=enandct=clnkandgl=us (accessed February 1, 2020).

Alikhani M, Chou MY, Khoo E, Alansari S, Kwal R, Elfersi T, Almansour A, Sangsuwon C, Al Jearah M, Nervina JM, Teixeira CC. Age-dependent biologic response to orthodontic forces. Am J Orthod Dentofac Orthop. 2018;153(5):632-44.

Arnsdorf EJ, Tummala P, Kwon RY, Jacobs CR. Mechanically induced osteogenic differentiation—the role of RhoA, ROCKII and cytoskeletal dynamics. J Cell Sci. 2009;122:546–553.

Aveic S, Craveiro RB, Wolf M, Fischer H. Current Trends in In Vitro Modeling to Mimic Cellular Crosstalk in Periodontal Tissue. Advanced Healthc Mater. 2021;10(1):2001269.

Chen CS, Mrksich M, Huang S, Whitesides GM, Ingber DE. Geometric control of cell life and death. Science. 1997;276(5317):1425-8.

Chen MX, Zhong YJ, Dong QQ, Wong HM, Wen YF (2021). Global, regional, and national burden of severe periodontitis, 1990–2019: An analysis of the Global Burden of Disease Study 2019. J Clin Periodontol. 2021; 48( 9):1165– 1188. https://doi.org/10.1111/jcpe.13506

De Belly H, Paluch EK, Chalut KJ. Interplay between mechanics and signalling in regulating cell fate. Nat Rev Mol Cell Biol. 2022;23(7):465-80.

DuFort CC, Paszek MJ, Weaver VM. Balancing forces: architectural control of mechanotransduction. Nat Rev Mol Cell Biol. 2011;12(5):308-19.

Engler AJ, Sen S, Sweeney HL, Discher DE. Matrix elasticity directs stem cell lineage specification. Cell. 2006;126:677-689.

Eke PI, Borgnakke WS, Genco RJ. Recent epidemiologic trends in periodontitis in the USA. Periodontol 2000. 2020; 82: 257– 267. https://doi.org/10.1111/prd.12323

Galli M, Yao Y, Giannobile WV, Wang HL. Current and future trends in periodontal tissue engineering and bone regeneration. Plast Aesthet Res. 2021;8.

Graber LW, Vanarsdall RL, Vig KWL. Orthodontics: Current Principles & Techniques. Philadelphia, PA: Elsevier/Mosby, 2012.

Graves DT. The potential role of chemokines and inflammatory cytokines in periodontal disease progression. Clin Infect Dis 1999;28:482-490.

Griffith LG, Swartz MA. Capturing complex 3D tissue physiology in vitro. Nat Rev Mol Cell Biol. 2006;7(3):211-24

Hinz B. Myofibroblasts. Experimental eye research. 2016;142:56-70.

Hong SY, Jeon YM, Lee HJ et al. Activation of RhoA and FAK induces ERK-mediated osteopontin expression in mechanical force- subjected periodontal ligament fibroblasts. Mol Cell Biochem. 2010;335: 263–272. https://doi.org/10.1007/s11010-009-0276-1

Hotamisligil GS, Spiegelman BM. Tumor necrosis factor α: a key component of the obesity-diabetes link. Diabetes. 1994;43(11):1271-8.

Iwasaki LR, Crouch LD, Tutor A, Gibson S, Hukmani N, Marx DB, et al. Tooth movement and cytokines in gingival crevicular fluid and whole blood in growing and adult subjects. Am J Orthod Dentofac Orthop. 2005;128:483–91.

Iwasaki LR, Gibson CS, Crouch LD, Marx DB, Pandey JP, Nickel JC. Speed of tooth movement is related to stress and IL-1 gene polymorphisms. Am J Orthod Dentofac Orthop. 2006;130:698.e1-698.e9.

Jakhu H, Gill G, Singh A. 2018. Role of integrins in wound repair and its periodontal implications. J Oral Biol Craniofac Res. 8(2):122–125.

Jensen C, Teng Y. Is It Time to Start Transitioning From 2D to 3D Cell Culture? Front Mol Biosci. 2020;7:33. doi: 10.3389/fmolb.2020.00033

Kanchanawong P, Calderwood DA. Organization, dynamics and mechanoregulation of integrin-mediated cell–ECM adhesions. Nat Rev Mol Cell Biol. 2023;24(2):142-61.

Kang KL, Lee SW, Ahn YS, Kim SH, Kang YG. Bioinformatic analysis of responsive genes in two-dimension and three-dimension cultured human periodontal ligament cells subjected to compressive stress. J Periodontal Res. 2013;48(1):87-97.

Kechagia JZ, Ivaska J, Roca-Cusachs P. Integrins as biomechanical sensors of the microenvironment. Nat Rev Mol Cell Biol. 2019;20(8):457-73.

Kletsas D, Basdra EK, Papavassiliou AG (2002) Effect of protein kinase inhibitors on the stretch-elicited c-Fos and c-Jun up-regulation in human PDL osteoblast-like cells. J Cell Physiol 190:313–321. https://doi.org/10.1002/jcp.10052

Koledova Z (ed.), 3D Cell Culture: Methods and Protocols, Methods in Molecular Biology, vol. 1612, DOI 10.1007/978-1-4939-7021-6_1, © Springer Science+Business Media LLC 2017

Li M, Yi J, Yang Y, Zheng W, Li Y, Zhao Z. Investigation of optimal orthodontic force at the cellular level through three-dimensionally cultured periodontal ligament cells. Eur J Orthod. 2016;38(4):366-72

Li M, Zhang C, Yang Y. Effects of mechanical forces on osteogenesis and osteoclastogenesis in human periodontal ligament fibroblasts: A systematic review of in vitro studies. Bone Joint Res 2019;8:19-31. DOI: 10.1302/2046-3758.81.BJR-2018-0060.R1.

Marchesan JT, Scanlon CS, Soehren S, Matsuo M, Kapila YL. Implications of Cultured Periodontal Ligament Cells for the Clinical and Experimental Setting: A Review. Arch Oral Biol. 2011;56(10):933-43.

Martino F, Perestrelo AR, Vinarský V, Pagliari S, Forte G. Cellular mechanotransduction: from tension to function. Front Physiol. 2018;9:824.

Masella RS, Meister M. Current concepts in the biology of orthodontic tooth movement. Am J Orthod Dentofac Orthop. 2006 1;129(4):458-68.

Matthews BG, Wee NK, Widjaja VN, Price JS, Kalajzic I, Windahl SH. αSMA osteoprogenitor cells contribute to the increase in osteoblast numbers in response to mechanical loading. Calcif Tissue Int. 2020;106(2):208-17.

McBeath R, Pirone DM, Nelson CM, Bhadriraju K, Chen CS. Cell shape, cytoskeletal tension, and RhoA regulate stem cell lineage commitment. Dev Cell. 2004;6(4):483-95.

Meikle MC. The tissue, cellular, and molecular regulation of orthodontic tooth movement: 100 years after Carl Sandstedt. Eur J Orthod. 2005;28:221–40. doi:10.1093/ejo/cjl001.

Melsen B, Cattaneo PM, Dalstra M, Kraft DC. The importance of force levels in relation to tooth movement. In Seminars in Orthodontics 2007 Dec 1 (Vol. 13, No. 4, pp. 220-233). WB Saunders.

Meng Y, Han X, Huang L, Bai D, Yu H, He Y, Jing Y. Orthodontic mechanical tension effects on the myofibroblast expression of alpha-smooth muscle actin. Angle Orthod. 2010;80(5):912-8.

Mulimani P, Popowics TE. Understanding periodontal tissue responses to mechanical load through the use of the pig model, *Sus scrofa*. In Embracing novel technologies in dentistry and orthodontics. 2019;1001:86.

Nanci A. Ten Cate's Oral Histology. Development, Structure, & Function. Mosby, 2012

Nanes MS. Tumor necrosis factor-α: molecular and cellular mechanisms in skeletal pathology. Gene. 2003;321:1-5.

Oleksiak MF, Churchill GA, Crawford DL. Variation in gene expression within and among natural populations. Nat Genet. 2002;32(2):261-6.

Pan J, Wang T, Wang L, Chen W, Song M. Cyclic strain-induced cytoskeletal rearrangement of human periodontal ligament cells via the Rho signaling pathway. PLoS One. 2014;9(3):e91580.

Papadopoulou A, Cantele A, Koletsi D, Eliades T, Kletsas D. Short-and long-term treatment with TNF-α inhibits the induction of osteoblastic differentiation in cyclic tensile-stretched periodontal ligament fibroblasts. Eur J Orthod. 2020;42(4):396-406.

Pellegrin S, Mellor H. Actin stress fibres. J Cell Sci. 2007;120(20):3491-9.

Pihlstrom BL, Michalowicz BS, Johnson NW. Periodontal diseases. Lancet. 2005;366(9499):1809-20.

Putra VD, Kilian KA, Knothe Tate ML. Biomechanical, biophysical and biochemical modulators of cytoskeletal remodelling and emergent stem cell lineage commitment. Commun Biol. 2023;6(1):75.

Rodriguez, J.P., Gonzalez, M., Rios, S., Cambiazo, V., 2004. Cytoskeletal organization of human mesenchymal stem cells (MSC) changes during their osteogenic differentiation. J Cell Biochem. 93, 721–731.

Roguljic H, Matthews BG, Yang W, Cvija H, Mina M, Kalajzic I. In vivo identification of periodontal progenitor cells. J Dent Res. 2013;92(8):709-15.

Romani P, Valcarcel-Jimenez L, Frezza C, Dupont S. Crosstalk between mechanotransduction and metabolism. Nat Rev Mol Cell Biol. 2021;22(1):22-38.

San Miguel SM, Fatahi MR, Li H, Igwe JC, Aguila HL, Kalajzic I. Defining a visual marker of osteoprogenitor cells within the periodontium. J Periodontol Res. 2010;45(1):60-70.

Sims JR, Karp S, Ingber DE. Altering the cellular mechanical force balance results in integrated changes in cell, cytoskeletal and nuclear shape. J Cell Sci. 1992 Dec;103( Pt 4):1215–1222.

Talele NP, Fradette J, Davies JE, Kapus A, Hinz B. Expression of α-smooth muscle actin determines the fate of mesenchymal stromal cells. Stem Cell Reports. 2015;4(6):1016-30.

Tomasek JJ, Gabbiani G, Hinz B, Chaponnier C, Brown RA. Myofibroblasts and mechano-regulation of connective tissue remodelling. Nat Rev Mol Cell Biol.2002;3(5):349-63.

Tonetti MS, Jepsen S, Jin L, Otomo-Corgel J. Impact of the global burden of periodontal diseases on health, nutrition and wellbeing of mankind: A call for global action. J Clin Periodontol. 2017;44(5):456-62.

Tvorogova, AA, Kovaleva AV, Saidova AA. Reorganization of actin cytoskeleton and microtubule array during the chondrogenesis of bovine MSCs. Annu Res Rev Biol. 2018;29, 1–14.

Vicente-Manzanares M, Ma X, Adelstein RS, Horwitz AR. Non-muscle myosin II takes centre stage in cell adhesion and migration. Nat Rev Mol Cell Biol. 2009;10(11):778-90.

Vogel V, Sheetz M. Local force and geometry sensing regulate cell functions. Nat Rev Mol Cell Biol. 2006;7(4):265-75.

Wishney M. Potential risks of orthodontic therapy: a critical review and conceptual framework. Aust Dent J. 2017;62:86–96. doi:10.1111/adj.12486.

Wang N, Tytell JD, Ingber DE. Mechanotransduction at a distance: mechanically coupling the extracellular matrix with the nucleus. Nat Rev Mol Cell Biol. 2009;10(1):75-82.

Whitehead A, Crawford DL. Variation in tissue-specific gene expression among natural populations. Genome biol. 2005;6(2):1-4.

Wongkhantee S, Yongchaitrakul T, Pavasant P (2008) Mechanical stress induces osteopontin via ATP/P2Y1 in periodontal cells. J Dent Res. 2008;87:564–568. https://doi.org/10.1177/154405910808700601

Xu Q, Ni S, Wu F, Liu F, Ye X, Mougin B, Meng X, Du X. Investigation of variation in gene expression profiling of human blood by extended principle component analysis. PloS one. 2011;6(10):e26905.

Yamamoto T, Ugawa Y, Kawamura M, Yamashiro K, Kochi S, Ideguchi H, Takashiba S. Modulation of microenvironment for controlling the fate of periodontal ligament cells: the role of Rho/ROCK signaling and cytoskeletal dynamics. Cell Commun Signal. 2018;12(1):369-78

Yamashiro K, Myokai F, Hiratsuka K et al. Oligonucleotide array analysis of cyclic tension-responsive genes in human periodontal ligament fibroblasts. Int J Biochem Cell Biol. 2007; 39:910–921. https:// doi.org/10.1016/j.biocel.2007.01.015

Yang L, Yang Y, Wang S, Li Y, Zhao Z. In vitro mechanical loading models for periodontal ligament cells: From two-dimensional to three-dimensional models. Arch Oral Biol. 2015;60(3):416–424. doi:10.1016/j.archoralbio.2014.11.012.

Yourek G, Hussain MA, Mao JJ. Cytoskeletal changes of mesenchymal stem cells during differentiation. ASAIO J. 2007;53, 219–228.

Zaidel-Bar R, Zhenhuan G, Luxenburg C. The contractome–a systems view of actomyosin contractility in non-muscle cells. J Cell Sci. 2015;128(12):2209-17.

# CHAPTER 2. SINGLE CELL ANALYSIS OF TNF-α AND RHO/ROCK PATHWAY EFFECTS ON PDL CELL STRUCTURE, CONTRACTILITY AND OSTEOGENIC DIFFERENTIATION

## 2.1 INTRODUCTION

Maintaining the complex, multi-layered, hierarchical architecture of the PDL is critical in preserving periodontal homeostasis and function in the highly dynamic oral environment. Precise orchestration of region-specific cell differentiation in response to microenvironment alterations forms the basis of periodontal structural integrity and function maintenance. PDL cells respond to mechanical perturbations in the local microenvironment by undergoing deformation which mainly upregulates osteogenic gene expression leading to osteoblastic differentiation and bone deposition (Yamamoto et al. 2018). The cytoskeleton is a key structural component, through which such cellular responses to biochemical and biomechanical cues in the microenvironment occur. In undifferentiated MSCs, F-actin structure, composition and tension have been shown to determine cell shape, spreading, function and lineage commitment (McBeath et al. 2004, Putra et al. 2023). This highlights the vital link between cells' structural and mechanical properties and their lineage determination and function. Considering the near perpetual presence of mechanical loads in the PDL, investigating this link is indispensable for understanding PDL function in health and disease. This is especially needed to develop more effective and advanced therapeutic interventions for periodontal regeneration, orthodontic tooth movement and orthodontic retention.

Cellular contractile forces exerted by the cytoskeleton are crucial for a cell to sense its environment and to execute vital cellular functions like cell division, differentiation, migration and

survival (Chen et al. 1997, Polachek and Chen 2011). Consequently, these cellular forces are critical in ensuring homeostasis in tissue structure and function even amidst widely varying environmental factors. Aberrations in appropriate cellular force production can lead to developmental defects, poor tissue function, or diseased states (Obenaus et al. 2020). Cellular

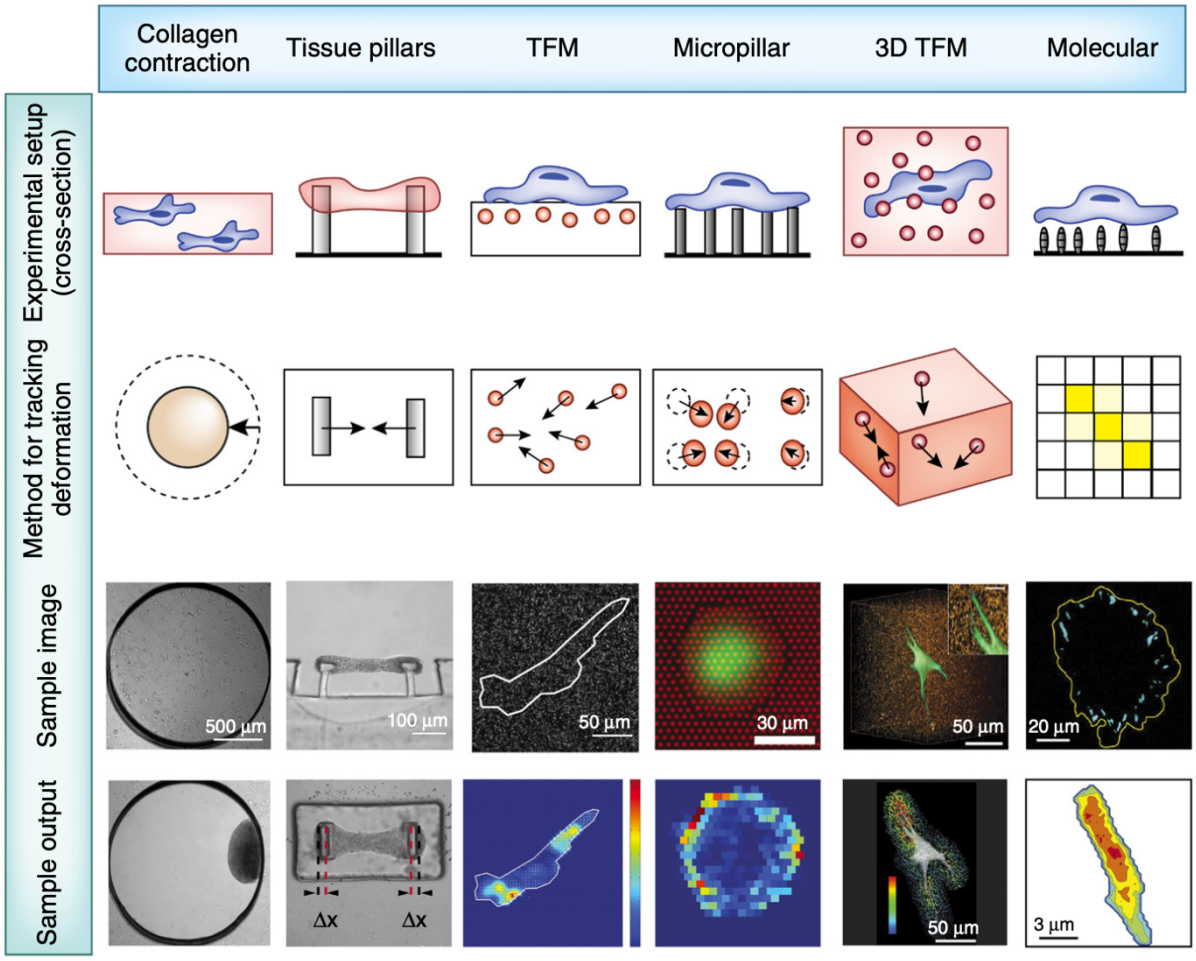


**Figure 2.1. Methods for measuring cellular forces.** 1) Collagen contraction methods measures collagen compaction by cellular forces; output measures reduction in collagen gel area. 2)Tissue pillars technique incorporates cantilevers of known stiffness into the system, so that as the tissue attached to the cantilevers contracts, the cantilevers bend, and the cantilever deflection is quantified to calculate tissue-generated force. 3)TFM (traction force microscopy technique) involves tracking the deformations of synthetic elastic polymer substrates that result from the exertion of cellular force. Contractility is measured by widefield microscopic imaging of fluorescent beads in the deformable substrate that get displaced by contraction of cells that are seeded on top of the substrates. 4) Micropillar assay is similar to TFM, but measures micropillar displacement by cells instead of fluorescent beads. 5) 3D TFM measures contractile forces by quantifying fluorescent bead displacement in all 3 dimensions through confocal imaging. 6) Molecular methods involve molecular tension sensors like a Förster resonance energy transfer (FRET) fluorophore pair which will emit a light spectrum as a function of strain exerted by the seeded cells. Techniques 1 and 2 measure tissue forces, techniques 4-6 measure single cell forces. (Image from Polachek and Chen et al. 2011).

forces at a tissue-level and single cell level have been quantified using several techniques depicted in Figure 2.1. Our lab has developed a high-yield reference-free traction force microscopy (TFM) technique to measure single cell forces, called the black dots (BD) technique (Beussman et al. 2023). Conventional TFM techniques measure displacement of randomly dispersed fluorescent beads within a deformable substrate on which the cells are seeded and exert contractile force. The technique requires two images to track forces - a reference image of the undeformed substrate and one or more images of the displacements caused by the cells. Hence, TFM becomes incompatible with immunofluorescent staining. To overcome this limitation, the BD technique involves using a patterned grid of dots stamped on a flexible, fluorescent substrate instead of randomly scattered fluorescent beads. Since the location and dimensions of grid dots are known beforehand, only one image is needed to record and calculate cell contractility. This makes our BD technique high yield and amenable to immunofluorescent cell staining. This technique has been used to measure platelet contractility and characterize different platelet types based on actin dispersion (Beussman et al. 2023). Currently, no such data or study exists on PDL cells' contractile forces, especially on a single cell level. In this chapter, I will demonstrate how the BD technique was used to calculate PDL cell contractile forces and also assess effects of certain biochemical mediators on cell contractility.

One of the periodontal responses to mechanical load application is elevated levels of cytokines like tumor necrosis factor-alpha (TNF- α), that then modulate local, stimulus-specific cell behavior, differentiation and function (Meikle 2006). TNF-α is a multi-functional cytokine involved in a wide-range of cellular effects under physiological conditions through its activation of the toll like receptor (TLR) signaling pathway (Kim et al. 2008, MacEwan 2002). Endogenous TNF-α is an important mediator of natural immunity necessary to recruit defense mechanisms to fight microbial infections. It is also involved in other diverse physiological functions like cell proliferation and differentiation, cell death, neuroprotection and neurotransmission (Leong and Karsan 2000). TNF-

α is primarily produced as a 233-amino acid-long transmembrane protein (mTNF), from which the soluble form (sTNF) is released via proteolytic cleavage by TNF alpha converting enzyme (TACE, also called ADAM17). It acts on 2 types of receptors – TNFR1 and TNFR2. TNFR1 is pro-inflammatory, apoptotic and activated by both mTNF and sTNF. TNFR2 on the other hand is anti-inflammatory, pro-cell proliferation and activated only by mTNF (MacEwan 2002). It was initially thought that TNF-α was secreted primarily by macrophages and endothelial cells. However, elevated tissue and plasma levels of TNF -α were also caused by its production by multiple other cell types like lymphoid cells, mast cells, cardiac myocytes, adipocytes, fibroblasts, and neuronal cells (Lee et al. 2011).

TNF-α effects are greatly dependent on the strength and duration of its expression. TNF-α plasma levels lower than 1 pg/mL are considered physiologic (Lee et al. 2011). Levels greater than 1 pg/mL are found in pathological conditions like atherosclerosis, tumorigenesis, diabetes and autoimmune disorders like rheumatoid arthritis, etc. (Lee et al. 2011, Leong and Karsan 2000). In the PDL, elevated TNF-α levels have been found play a central role in the pathogenesis and development of chronic periodontitis. These are mediated by TNF-α's roles of immune cell recruitment, stimulation of other pro-inflammatory cytokines and bone and periodontal tissue destruction (Yucel-Lindberg and Bage 2013, Algate et al. 2016, Liu et al. 2016). Additionally, elevated PDL levels of TNF-α are also found during OTM where its roles are predominantly pro-inflammatory and osteoresorptive (Jager et al. 2005, Basaran et al. 2006, Yoshimatsu et al. 2006, Ren et al. 2007, Grant et al. 2013, Papadopoulou 2020). TNF-α promotes osteoclast differentiation from progenitors by upregulating factors involved in transcriptional regulation of osteoclast-specific genes, such as interleukin-6 (IL-6) and macrophage colony stimulating factor (M-CSF). Importantly, it also increases responsiveness of receptor activator of nuclear factor kappa B (RANK) to its ligand - RANK ligand (RANKL) causing more precursor cells to differentiate into mature osteoclasts. TNF-α also has a well-established role as an inhibitor of osteoblastogenesis.

It does so by preventing osteoblast differentiation mainly by a) downregulating expression of key osteogenic genes such as alkaline phosphatase (ALP), runt-related transcription factor 2 (RUNX2), osteocalcin (OCN) and osterix (Osx) and b) inhibiting bone forming pathways such as Wingless-related integration site (Wnt) and bone morphogenetic protein (BMP) (Figure 2.2) (Nanes 2003, Algate et al. 2016, Papadopoulou 2020).

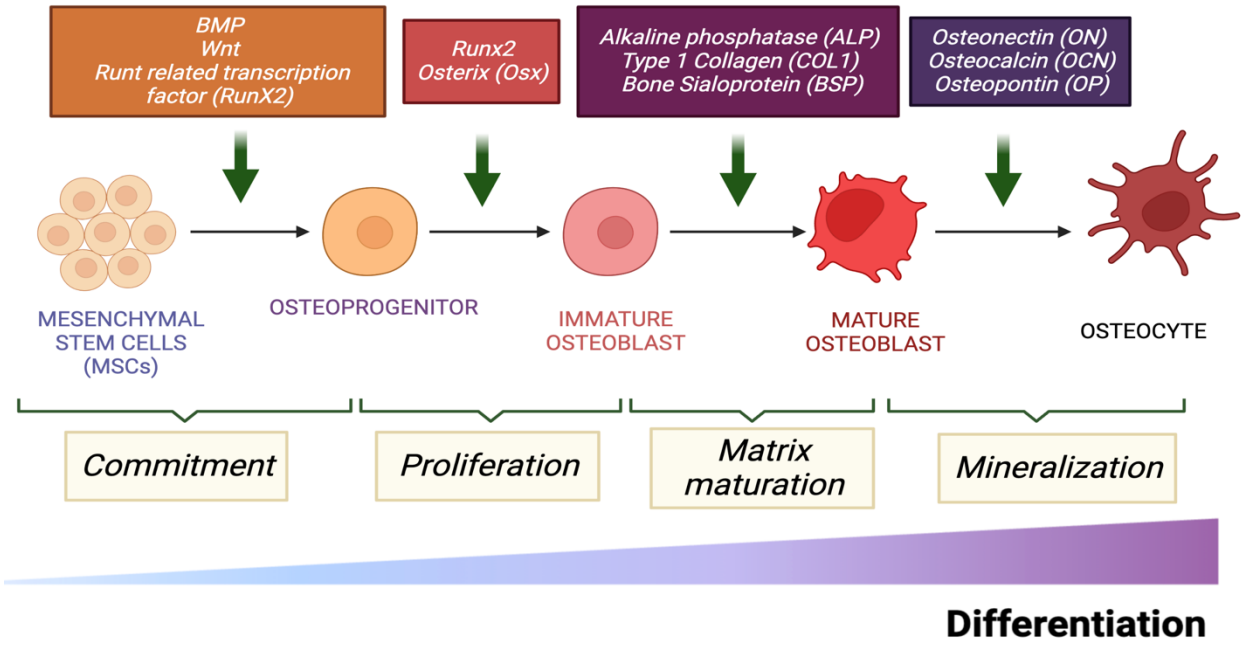


**Figure 2.2. Schematic of the osteoblast differentiation process.** TNF-α inhibits osteogenesis by blocking the BMP and Wnt bone forming pathways and by inhibiting osteogenic transcription factors like RUNX2 - runt-related transcription factor 2, ALP - alkaline phosphatase, OCN - osteocalcin and Osx – osterix. (Figure created using BioRender).

TNF-α also plays a significant role in altering cell structure and mechanical properties while activating mechanotransduction pathways. TNF-α enhanced endothelial monolayer tension and permeability by increasing Rho/ROCK-mediated cell contractility through upregulation of phosphorylated myosin light chain colocalization within actin stress fibers (Urbano et al. 2017). TNF-α treatment also increased F-actin fluorescence intensity and stress fiber number, density and thickness in endothelial cells (Campos et al. 2009, Lee et al. 2011). Additionally, TNF- α

reduced cell contractility by decreasing aSMA production, myofibroblast differentiation and TGF-β pathway activation (Goldberg et al. 2007). In PDLCs, TNF-α upregulated actin cytoskeleton and stress fiber formation by activating the Rho/ROCK pathway (Takemura 2009). Furthermore, TNF-α upregulated expression of integrin subunits and focal adhesion kinases in PDL cells. These TNF- α mediated structural changes led to change in PDL function by inhibiting their migration (Takemura 2009). Thus, cytoskeletal alterations seem to be an important mechanism through which TNF- α may modulate disease progression and treatment response in the periodontium.

The effect of TNF-α mediated upregulation of the actin cytoskeleton on PDLCs morphology and biomechanical properties such as contractile force remain unknown. Currently, the classical view of TNF-α is that of an established inducer of osteoclastogenesis and inhibitor of osteoblastogenesis in the periodontium. However, TNF-α also activates the Rho/ROCK pathway, a pathway that results in osteogenic gene expression (Takemura 2006, Martino et al. 2018, Yamamoto et al. 2018). Thus, TNF-α by activating Rho/ROCK pathway may also be assumed to increase actomyosin contractility, cause cells to assume a larger spread area and induce osteogenic differentiation (McBeath et al. 2004). Evidence for this assumption exists in the literature with the recent discovery that TNF-α also possesses osteogenic differentiation effects (Osta et al. 2014). These paradoxical effects were only described in *in vitro* models and were concentration- and time-dependent, and cell-type specific. However, the effect of TNF-α on none of these parameters of periodontal cells have been investigated. Investigations on them are especially needed in the periodontal field as mechanical loads which are pervasive in the periodontium, can also induce cytoskeletal alterations thus adding an extra layer of complexity to the biochemically mediated changes in cytoskeleton. It, hence, becomes necessary to delineate and characterize the effects of TNF-α on cytoskeletal alterations and cell contractility, considering their central role in determining cell differentiation and function (McBeath et al. 2004). Especially,

the effect of TNF-α on the structural and mechanical cell properties, the exact role played by Rho/ROCK pathway in mediating its downstream effects and the subsequent regulation of osteoblastic differentiation function have rarely been investigated. Hence, the objective of current study is to assess the effects of TNF-α and the Rho/ROCK pathway on PDL cell structure, contractility and osteogenic differentiation ability. My central hypothesis is that TNF- α increases F-actin production through Rho / ROCK pathway, increases cell contractility and cell spread area and induces osteogenic differentiation of PDL cells.

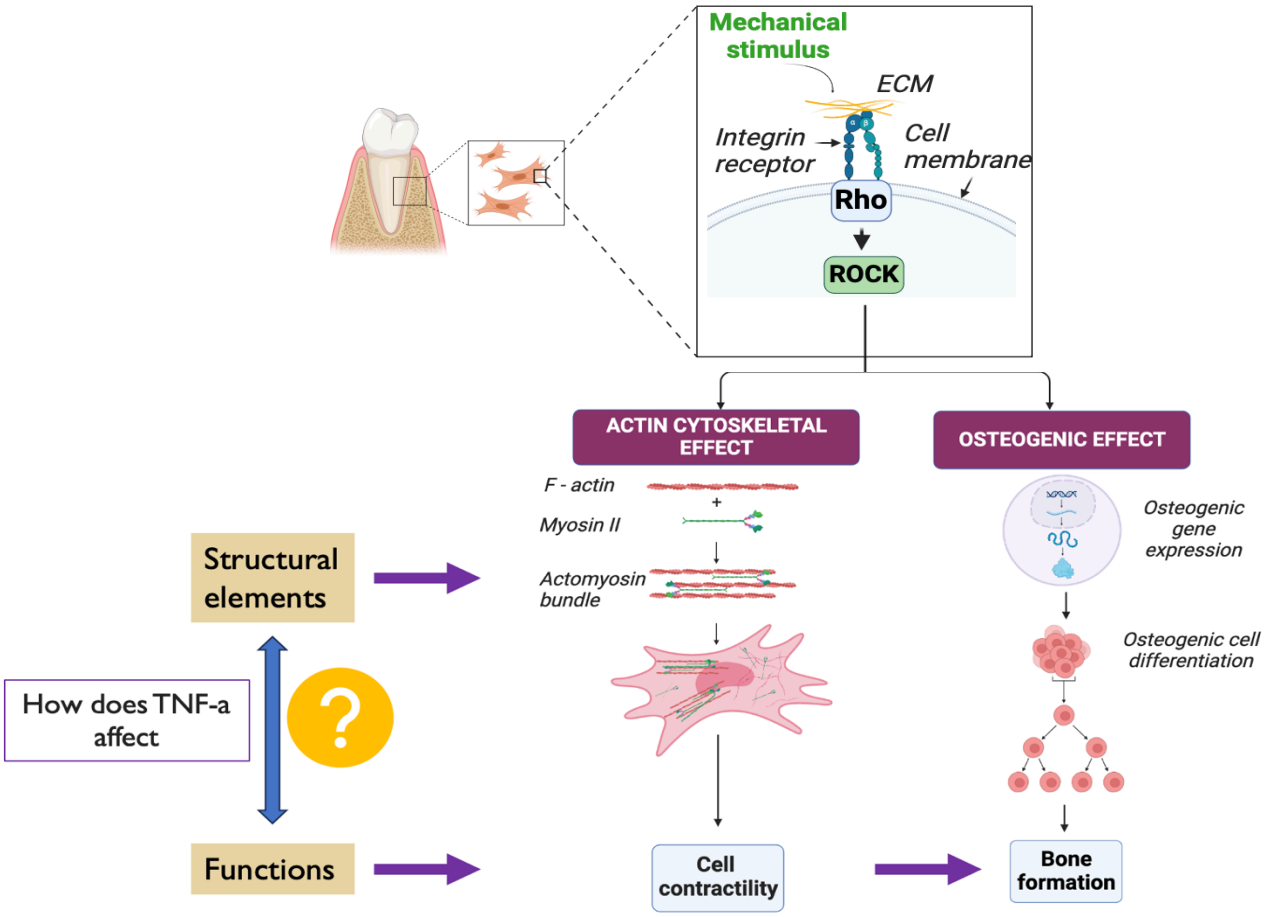


**Figure 2.3. Graphical abstract of Specific Aim 1 research question.** Mechanical stimuli cause Rho/ROCK activation and TNF-α production. How do the cell cytoskeleton and osteogenic differentiation change when both of them interact? (Figure created using BioRender).

## 2.2 MATERIALS AND METHODS

### *2.2.1 Single cell structure and contractility analysis using the black dots (BD) technique*

#### *2.2.1.1 Microfabrication of patterned stamp*

First, a silicon master mold with an array of vertical pillars was created with the desired pattern size by photolithography as described previously (Feghhi et al. 2016). Briefly, photoresist was spun onto a silicon wafer and an e-beam lithography system was used to pattern circles of the desired diameter and center-to-center spacing. The photoresist was then developed and etched to create a master containing an array of vertical silicon pillars. Since PDL cells are large, we used a pattern with dot diameter of 3 μm and dots' center-to-center spacing of 6 μm, and the final etched pattern had a height of 10 μm.

To generate the stamps for patterning the fluorescent protein, PDMS (Sylgard 184, Dow Corning) at a 10:1 base to curing agent ratio is poured onto the master mold and cured in a 110°C oven for 20 minutes. The cured PDMS is peeled from the master mold, revealing a negative version of the original pattern: a grid of holes instead of pillars. Edges of the stamp were trimmed with sharp razors and stored in enclosed petri dishes prior to use.

#### *2.2.1.2 Sacrificial PVA film production*

Polyvinyl alcohol (PVA) films for transferring the fluorescent pattern were made following previously described protocols (Beussman et al. 2023). A mixture of 0.55 g PVA powder (Sigma) was mixed with 15 mL DI water and heated for 30 minutes at 110°C until the powder fully dissolved. A standard 10 cm Petri dish was plasma treated for 10 seconds to help the final film remain attached to the dish. After cooling down to room temperature, the liquid PVA mixture was poured into the plasma-treated dish. The dish was left uncovered in a 65°C oven overnight to

allow the liquid to completely evaporate. The next day, the dish was removed from the oven revealing a thin, dried PVA film loosely attached to the bottom of the Petri dish. The film was cut into appropriate sized pieces and used as needed, or the dish was covered and sealed with parafilm for longer term storage.

#### *2.2.1.3 Flexible PDMS substrate preparation*

Flexible 7.7 kPa polydimethyl siloxane (PDMS) substrates were manufactured as previously published (Palchesko et al. 2012, Rodriguez et al. 2019, Beussman et al. 2023). PDMS was used in this study because its stiffness can be tuned within a biologically relevant range, it is amenable to microcontact printing, and it can be coated with proteins of interest relevant to numerous cell types (Wang et al. 2010, Palchesko et al. 2012, Rodriguez et al. 2019). Soft PDMS (Sylgard 527, 1:1 ratio of parts A and B, Dow Corning) and normal PDMS (Sylgard 184, 10:1 ratio of base to curing agent) were first prepared separately and allowed to degas for at least 20 minutes under vacuum. The two types of PDMS were then mixed to form a mixture of 2.5% Sylgard 184 and 97.5% Sylgard 527 by weight, and the mixture was degassed for 20 minutes under vacuum. Round glass coverslips (25 mm diameter, #1 thickness, VWR) were plasma treated for 30 seconds (Plasma Prep II, SPI Supplies) and a 100-130 µL droplet of the PDMS mixture was placed onto each of the plasma-treated glass coverslips. The PDMS droplets were allowed to spread across the glass coverslips on a level countertop for at least 30 minutes, resulting in a PDMS layer that is approximately 250 µm in height. The PDMS-coated coverslips were degassed for 30 minutes before transferring to a 65°C oven overnight to cure. The following day, the PDMS substrates were removed from the oven and cooled at room temperature. To extract unpolymerized monomers, the PDMS substrates were submerged in 100% ethanol for at least 3 hours, followed by multiple rinses with DI water before drying in a 65°C oven overnight.

#### *2.2.1.4 Microcontact printing*

The patterned PDMS stamps and PVA film were used to deposit a layer of fluorescent protein onto the flexible PDMS substrates similar to previously published techniques (Yu et al. 2012, MacNearney et al. 2016, Beussman et al. 2023). All steps were performed at room temperature and preferably in a standard tissue culture hood. First, Alexa-Fluor 647-conjugated-BSA (5 mg/mL, Life Technologies) was diluted 1:2000 in PBS (1X without calcium or magnesium, Life Technologies), and a 400 µL droplet was gently placed onto a patterned stamp (about 1 $cm^2$ area) within a petri dish. The droplet was left on the stamp for 45 minutes to allow the fluorescent BSA to adsorb onto the surface. Fresh PBS was slowly added to the petri dish until the liquid level rose above the stamp. The stamp was removed from the PBS and rinsed 3 times in fresh PBS dishes by gently submerging the stamp. After the final rinse, the stamp was dried with a gentle stream of nitrogen gas.

Next, the PVA film was used to transfer the fluorescent pattern from the stamp to the flexible substrate. A PVA film was trimmed to a size slightly larger than the stamp. The film was plasma treated for 60 seconds to facilitate protein transfer from the stamp. Using a pair of tweezers, the film was then lowered onto the dried stamp. The film was gently pressed onto the stamp using rounded-tip tweezers to remove any air gaps, and a thin piece of glass slide was placed on top of the film. A 50-gram weight was placed onto the glass slide to maintain close contact between the film and stamp. After 20 minutes, the weight and glass slide were removed and the PVA film was gently peeled from the stamp and transferred to the flexible PDMS substrate. Again, rounded-tip tweezers were used to gently press the film onto the substrate and remove any air gaps. The film was left on the flexible PDMS substrate for 20 minutes. The substrate was then submerged in PBS for up to 5 minutes, causing the film to rehydrate and float away from the surface where it can be discarded. The final substrate containing the pattern of fluorescent BSA, dubbed “black

dots," was stored in PBS overnight at 4°C before cell seeding and can be stored for at least one week.

#### *2.2.1.5 Primary PDL cell isolation*

PDL cells were harvested using pre-established protocols (Somerman et al. 1988) from the roots of healthy premolars, which had been extracted for orthodontic purposes in a 13 year-old male patient. Briefly, PDL tissue was gently dissected from the middle third of the tooth root surface in a culture dish containing wash buffer [Hanks' balanced salt solution (HBSS; Gibco) supplemented with 5% (v/v) fetal bovine serum (FBS; HyClone) and 50 U/mL penicillin and 50 µg/mL streptomycin]. The suspension was centrifuged at 400×g for 10 min at 4ºC. After aspirating the supernatant, PDL tissue was digested in collagenase I (3 mg/mL, Sigma- Aldrich) and dispase II (4 mg/mL; Sigma-Aldrich) for 1 hour at 37ºC. After digestion, the suspension was passed through a 70 µm strainer to obtain a single-cell suspension. The cell population was expanded by seeding the single-cell suspension in 24-well plates. Cells were grown in standard PDL cell culture medium of Dulbecco's Modified Eagle Medium (DMEM; Gibco) supplemented with 10% FBS (HyClone) and 1% penicillin/ streptomycin (Gibco) at 37ºC with 5% $CO_2$. On reaching confluence, cells were washed with PBS, trypsinized with 0.25% trypsin-EDTA (Gibco) and passaged progressively into T-75 and T-175 flasks. Cells at passage numbers 1 to 3 were stored in freezing media Cryostor (1 mL per 10 million cells) in a liquid nitrogen freezer then thawed, plated, and expanded as needed in T-75 and T-175 flasks. PDL cells between passage numbers 3 and 6 were used for the experiments.

#### *2.2.1.6 PDL cell seeding and treatment with reagents*

On the day of cell seeding, Fibronectin (Corning, CB40008) was diluted in PBS to 5 µg/mL and was pipetted onto the black dots substrates in a 6-well plate and allowed to incubate for 1-1.5 hours at room temperature. Fibronectin solution was then aspirated and replaced with 3 ml/well

culture medium. PDL cells were trypsinized in 0.25% trypsin-EDTA, lifted and counted. Cell solution containing 15,000 cells was then dispensed onto the black dots substrates in each well. After allowing 24 hrs for cells to spread, the culture medium was replaced with serum starved medium (DMEM supplemented with 0.1% FBS and 1% penicillin/ streptomycin) for the next 24 hours. Subsequently, substrates were divided into triplicates of 6 experimental groups. Each group was then treated for either 4 hrs or 24 hours with 3 ml culture medium supplemented with one of the following reagents – 1) TNF-$\alpha$- 10 ng/ml (Sigma Aldrich, H8916_10UG), 2)TNF- $\alpha$ inhibitor (EMD Millipore, 654527_10MG) – 0.5 $\mu$M, 3) ROCK inhibitor - Y-27632 - 5 $\mu$M (Tocris Bioscience, TB1254-GMP), 4) TNF- $\alpha$ - 10 ng/ml + ROCK inhibitior - Y-27632 - 5 $\mu$M, 5) DMSO Control – DMSO 0.5 $\mu$M, 6) Control – regular culture medium with no reagents added. At each step black dot substrates with cells were incubated at 37$^{o}$C with 5% $CO_2$. Three independent experiments were carried out on different batches of cells from the same donor, in the same manner.

#### *2.2.1.7 Immunofluorescent staining and imaging*

After 24 hours of reagent treatment, the BD substrates were fixed with 4% paraformaldehyde for 20 minutes, permeabilized with 0.1% Triton X-100 for 5 minutes at room temperature, and blocked with 10% goat serum (Life Technologies, diluted in PBS) for 1 hour. To label cells for aSMA, substrates were incubated for 1 hour with mouse primary antibodies for alpha-smooth muscle actin (aSMA, Santa Cruz Biotechnology, 1:500), followed by 3X, 5 min PBS rinses at room temperature. They were then treated with goat anti-mouse Alexa Fluor 647 (Invitrogen A21235, 1:500), Alexa Fluor 488 phalloidin (Invitrogen A12379, 1:500), and Hoechst 33342 (ThermoFisher, 1:2000) for 1 hour at room temperature. Substrates were then rinsed thrice in PBS for 5 min each and mounted using Fluoromount-G mounting medium (Life Technologies). Fixed and stained cells were imaged with a Nikon Ti-E widefield microscope using a 40X oil

objective. Images of single cells that were surrounded by at least 2-3 rows of undeformed black dots were taken. At least 30 images per experimental group were taken.

#### *2.2.1.8 Cell structure analysis*

Analysis to quantify cellular structure was carried out according to the technique described by Beussman et al. (2023) based on a modification of a prior technique for tracking objects (Blair and Dufresne 2008), using MATLAB code. The cell boundary, F-actin intensity and cell area were determined in MATLAB using a user-adjusted threshold and shape fill on the fluorescent F-actin image. To quantify the F-actin cytoskeletal structures, stress fiber analysis was carried out using the FilamentSensor (Eltzner et al. 2020) software. The algorithm carries out local binarization of detected stress fibers and adapts the semi local line sensor approach to fingerprint analysis to extract stress fiber features like thickness, length, number and distribution. Cells were screened manually for aSMA containing stress fibers and any cell with more than two aSMA positive stress fibers was classified as a myofibroblast. Myofibroblast count for each experimental group was thus generated.

#### *2.2.1.9 Cell contractility analysis*

Image analysis to quantify the deformation of the black dots, was carried out according to the technique described by Beussman et al. (2023) based on a modification of a prior technique for tracking objects (Blair and Dufresne 2008), using MATLAB code. Dot centroids are identified using peak finding algorithm and their deviation, if any, from the zero-displacement states are calculated. Traction forces are then calculated from the surface displacements using regularized Fourier Transform Traction Cytometry (FTTC). Traction stress outputs from FTTC were then converted to contractile force by multiplying each stress by the area it is applied over. Total force is calculated by summing the force magnitudes from each dot underneath the cell. Net force is similarly calculated by simply adding the force vectors from each dot together.

### *2.2.2 Osteogenic differentiation experiments*

To induce osteoblast differentiation, 22,000 cells/well of PDL cells were seeded in a 12-well plate with culture medium changes every 2-3 days. After cells reached up to 80-90% confluence, they were treated with osteogenic induction medium (OIM) (control medium supplemented with 50 μM

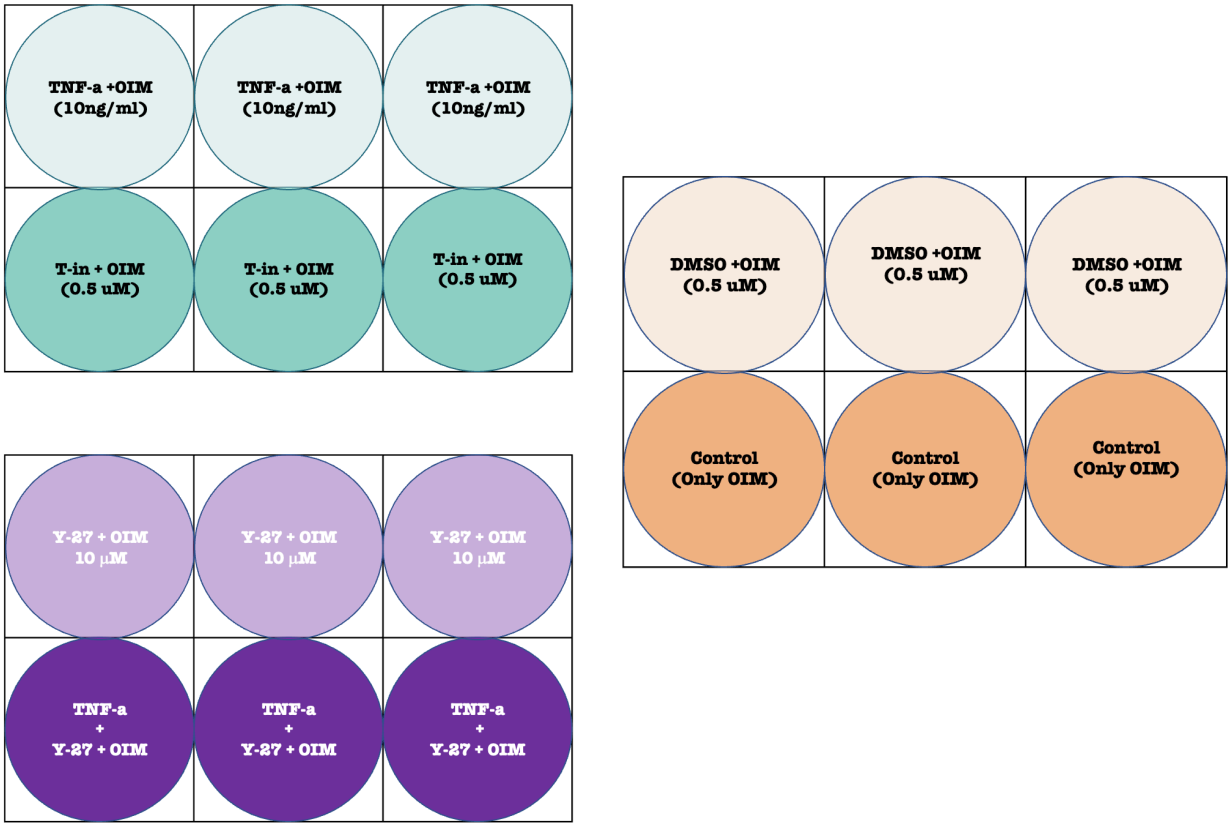


**Figure 2.4. Schematic of the experimental set-up for osteogenic differentiation experiments.** OIM – osteogenic induction medium; T-in – TNF-α inhibitor; Y-27 – ROCK inhibitor Y-27632.

ascorbic acid- 2-phosphate, 10 mM β-glycerophosphate, and 10 nM dexamethasone) supplemented with one of the following reagents – 1) TNF-α - 10 ng/ml (Sigma Aldrich, H8916_10UG), 2) TNF-α inhibitor (EMD Millipore, 654527_10MG) – 0.5 μM, 3) ROCK inhibitor - Y-27632 - 5 μM (Tocris Bioscience, TB1254-GMP), 4) TNF-α - 10 ng/ml + ROCK inhibitor - Y-27632 - 5 μM, 5) DMSO Control – DMSO 0.5 μM, 6) Control – osteogenic induction medium with no reagents added (Figure 2.4). There were three wells per experiment group and three such

independent experiments were carried out on different batches of cells from the same donor. On day 10 alkaline phosphatase assay and on day 28 alizarin red assay were carried out on each experimental group as described below.

#### *2.2.2.1 Alkaline phosphatase assay*

On day 10, cells were lifted using 0.25% trypsin-EDTA and $1 \times 10^5$ cells per experimental group were lysed in 0.1% Triton on a shaker for 20 mins. Lysate was then used to measure ALP activity assayed according to the instruction of the ALP activity assay kit (BioAssay Systems' QuantiChrome). This method utilizes p-nitrophenyl phosphate that is hydrolyzed by ALP in an alkaline environment (pH 10.5) into yellow colored p-nitrophenol, which is detected at 405 nm. In a 96-well plate, to 150 μL of the ALP assay working solution, 50 μL of cell lysate for each experimental group was added in triplicate, and the plate was run through the spectrophotometer (Molecular Devices SpectraMax M2 v0.008). ALP activity in [IU/L = μmol/(L·min)] was calculated by multiplying the spectrophotometer optical density (OD) reading with a constant k [k = Reaction volume / (Sample volume X reaction time X difference between OD of calibrator and water)]. ALP activity was normalized by dividing ALP activity values by protein levels within each experimental group. Protein levels were quantified by Bradford assay (Bio-rad, Quick Start), in which Coomassie blue stain binding with the protein content in the sample was measured spectrophotometrically at a wavelength of 595 nm. Increased absorbance at 595 nm is proportional to the amount of bound dye, and thus to the concentration of protein present in the sample.

#### *2.2.2.2 Alizarin red assay*

On day 28, cells were washed with PBS, fixed with 4% formaldehyde and incubated at room temperature for 15 min. Cells were then washed with DH2O, and incubated in alizarin red solution (pH 4.1 to 4.3) (Sigma-Aldrich) for 45 min at room temperature and washed 4x with DH2O. At the end, PBS was added to prevent cells from drying and for microscopic visualization and imaging.

Differentiated cells containing calcium phosphate deposits stained bright red. Brightfield microscope images at 4X were taken (at least 30 per experimental group) and their red staining intensity was calculated using FIJI image analysis software.

### *2.2.3 Statistical analysis*

Data were collected from three independent experiments. All values are expressed as mean ± standard error of mean. Results were compared using an unpaired two-tail t-test or repeated measures ANOVA or one-way ANOVA with post-hoc comparisons using GraphPad Prism. Differences with p-values <0.05 were considered statistically significant.

## 2.3 RESULTS

### *2.3.1 Single cell structure and contractility analysis using the black dots (BD) technique*

A total of 1617 single cells were analyzed for their cytoskeletal structure and contractility analysis using the BD technique. At least 90 cells in each experimental group were analyzed at two different time-points and with three independent experiments each (Table 2.1). Cells displayed in all experimental groups had morphologies like fusiform, spindle-shaped or polygonal. However, cells in the group treated with ROCK inhibitor had a characteristic dendritic appearance (Figure 2.5)

**Table 2.1. Number of single cells analyzed per experimental group**

| | Control | TNF-α | DMSO | TNF-in | Y-27 | TNF-α +Y-27 | Total |
|---|---|---|---|---|---|---|---|
| **4 hr** | 123 | 152 | 90 | 161 | 123 | 144 | 793 |
| **24 hr** | 137 | 129 | 152 | 137 | 127 | 142 | 824 |
| | | | | | | | 1617 |

(TNF-in – TNF-α inhibitor, Y-27 – ROCK inhibitor Y-27632)

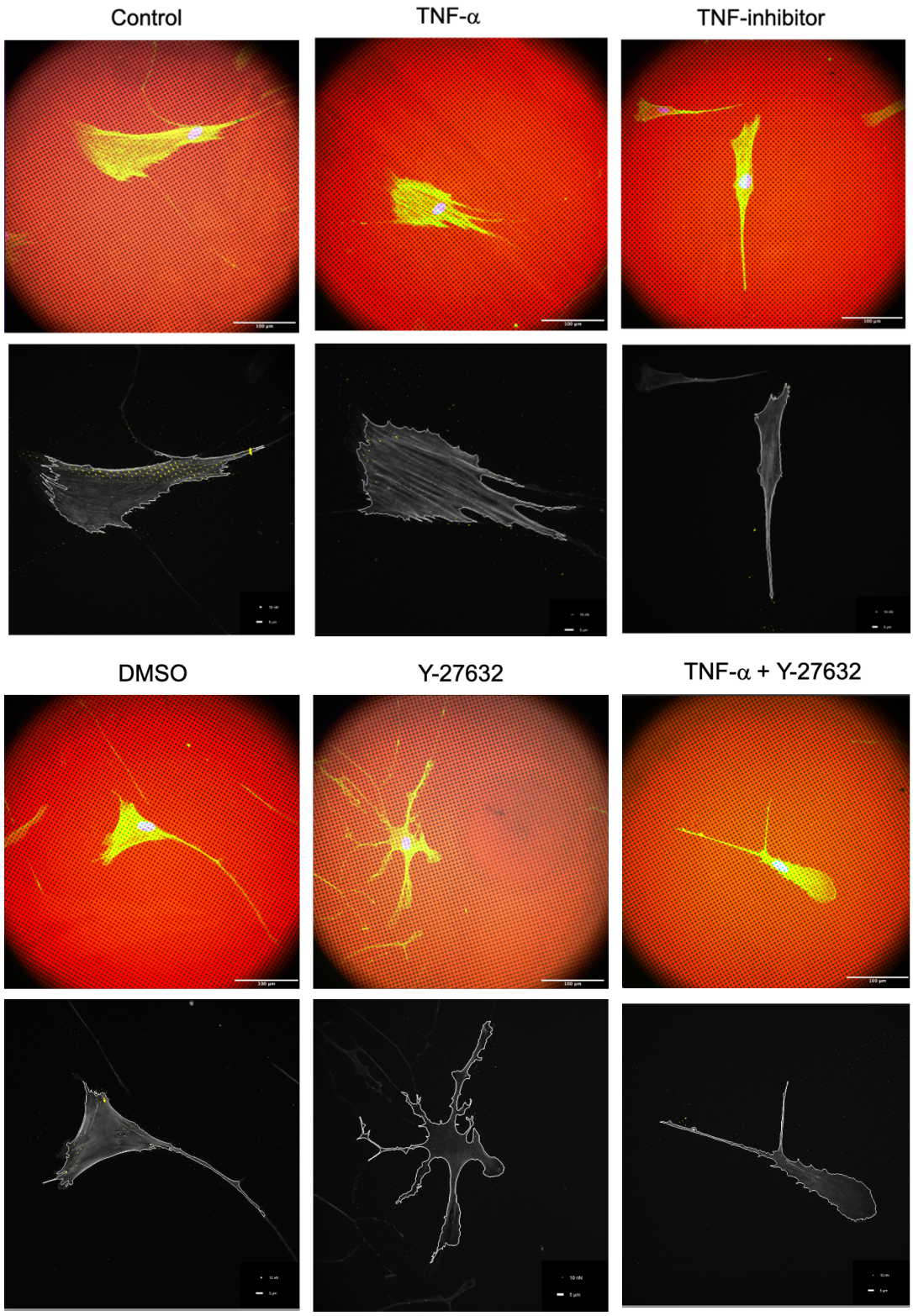


**Figure 2.5. Single cell images in each experimental group.** Top row in each group shows image of cells stained with Alexa Fluor 488 phalloidin for F-actin and Hoechst 33342 for nuclei against the fluorescent orange (Alexa Fluor 647) black dots substrates. Bottom row shows MATLAB output of cell images after contractile force calculation. Y-27632 - ROCK inhibitor.

#### *2.3.1.1 TNF-α increases F-actin intensity and inhibiting ROCK reduces it*

After treatment with reagents for both 4- and 24- hours, Y-27632 significantly reduced F-actin intensity compared to control, TNF-α and TNF-inhibitor groups (Figure 2.7).

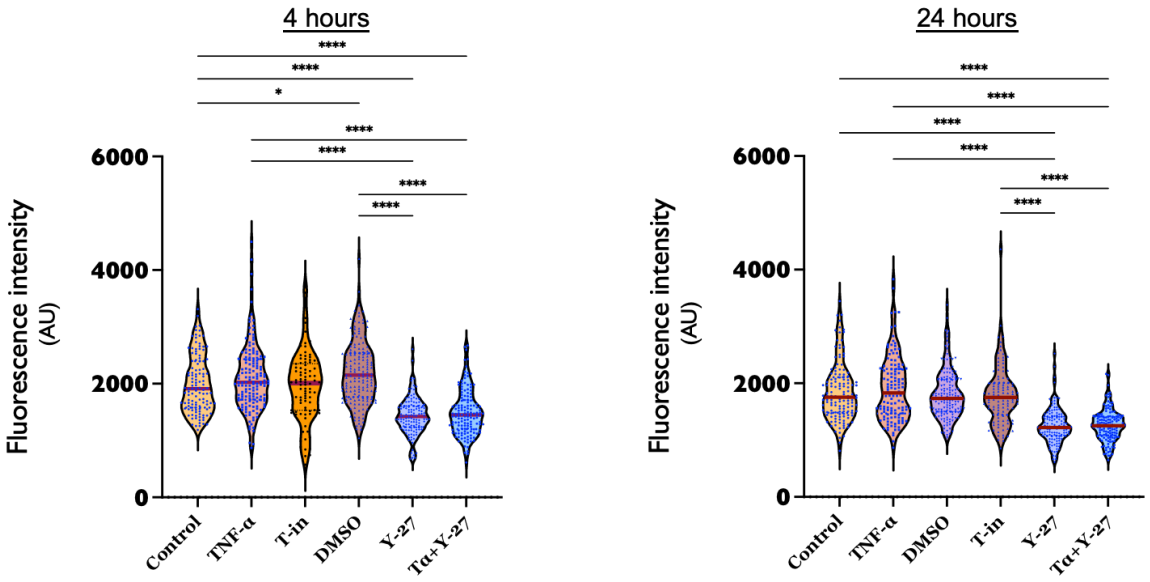


**Figure 2.7. Differences in F-actin intensity of PDLCs.** Data are mean ± SEM, *p<0.05, **p<0.01, ***p<0.001, ****p<0.0001 by one-way ANOVA with Tukey's multiple comparisons. TNF-in – TNF-α inhibitor, Y-27 – ROCK inhibitor Y-27632, Tα +Y-27 - TNF-α inhibitor + ROCK inhibitor Y-27632.

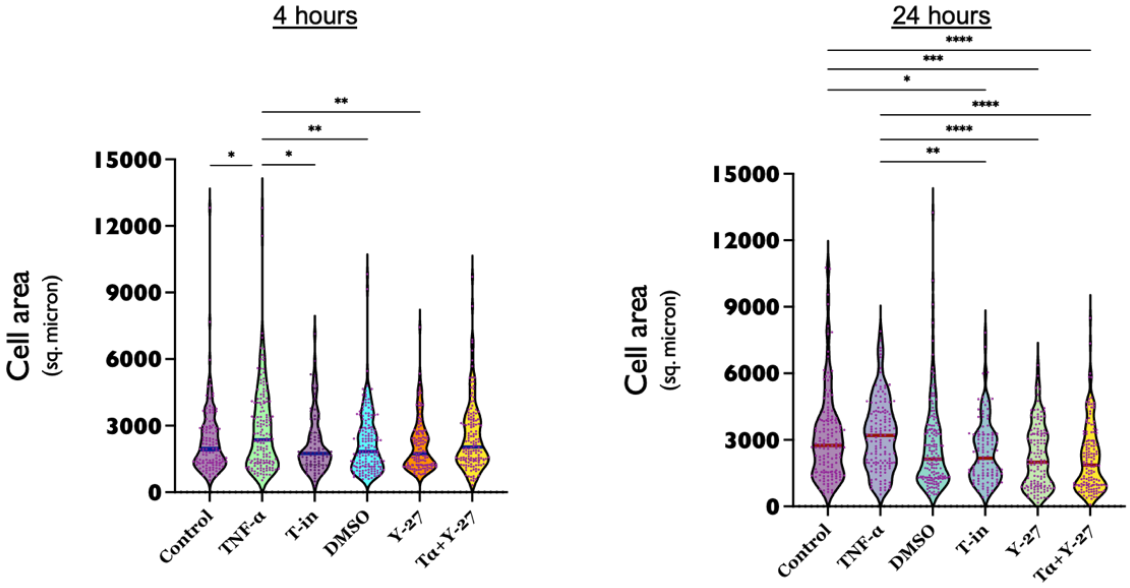


**Figure 2.6. Differences in cell surface area of PDLCs.** Data are mean ± SEM, *p<0.05, **p<0.01, ***p<0.001, ****p<0.0001 by one-way ANOVA with Tukey's multiple comparisons. TNF-in – TNF-α inhibitor, Y-27 – ROCK inhibitor Y-27632, Tα +Y-27 - TNF-α inhibitor + ROCK inhibitor Y-27632.

#### *2.3.1.2 TNF-α increases cell surface area*

Cells treated with TNF-α showed an increase in surface area compared to controls and TNF-inhibitor at 4 hrs and compared to Y-27632 treated cells at both 4- and 24- hours (Figure 2.6).

#### *2.3.1.3 TNF-α increases cellular contractility and inhibiting ROCK reduces it*

Contractile forces generated by PDL cells ranged from 0.4 to 1.3 μN. Cells treated with TNF-α showed increases in cellular contractile forces as compared to TNF-inhibitor at 4 hours. At 24 hours, cells in the control, TNF-α and TNF-inhibitor groups had greater contractility compared to cells treated with Y-27632 and Y-27632 with TNF-α (Figure 2.8).

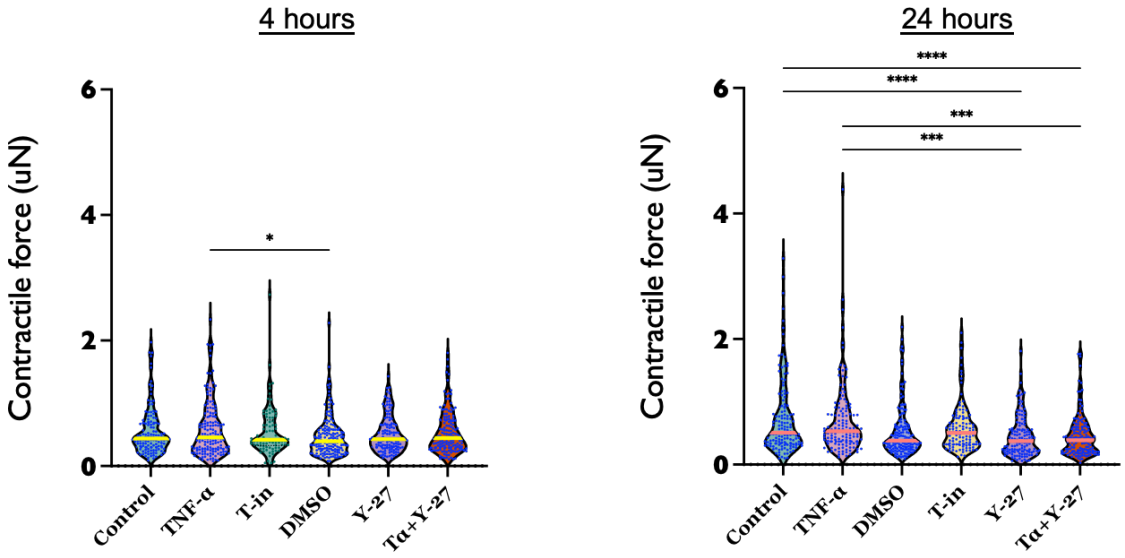


**Figure 2.8. Differences in contractile force of PDLCs.** Data are mean ± SEM, *p<0.05, **p<0.01, ***p<0.001, ****p<0.0001 by one-way ANOVA with Tukey's multiple comparisons. TNF-in – TNF-α inhibitor, Y-27 – ROCK inhibitor Y-27632, Tα +Y-27 - TNF-α inhibitor + ROCK inhibitor Y-27632.

#### *2.3.1.4 TNF-α increases number of stress fibers*

Stress fiber analysis of cells using FilamentSensor (Figure 2.10) showed increase in number of stress fibers in TNF-α compared to all groups at 24 hours. However, inhibiting ROCK, giving rise to dendritic morphology of cells, seemed to increase number, thickness and length of stress fibers (Figure 2.9).

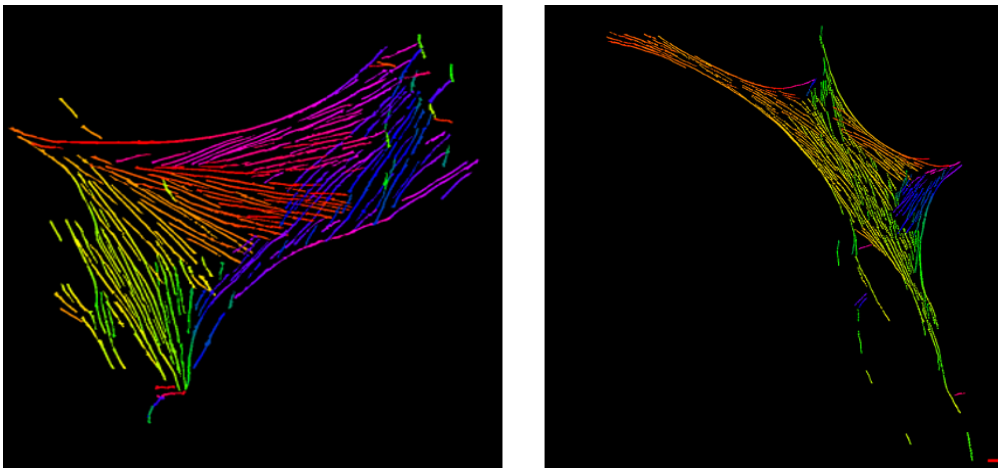

**Figure 2.10. Output images of stress fiber analysis by FilamentSensor.** Colors indicate change in orientation of stress fibers.

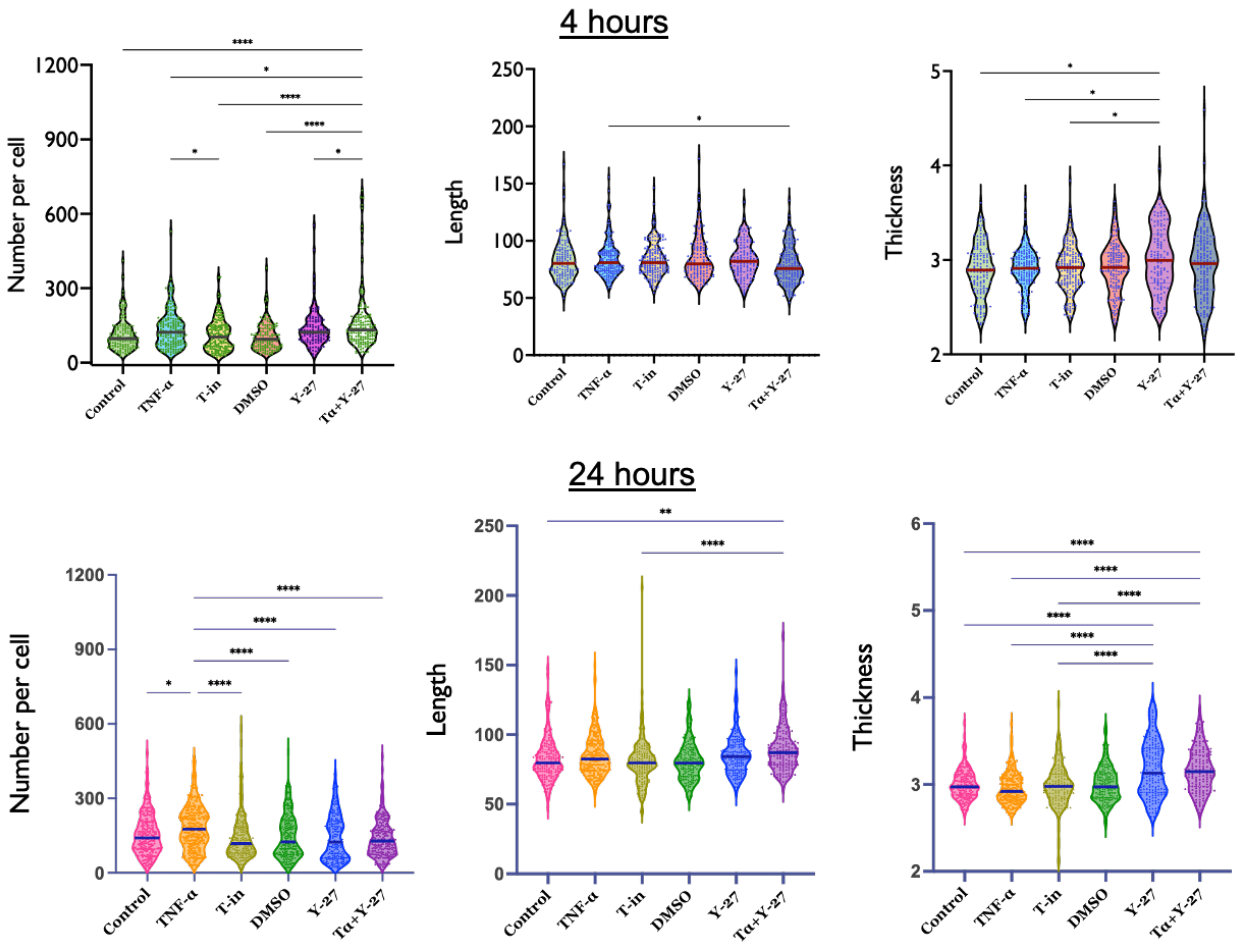


**Figure 2.9. Quantitative stress fiber analysis by FilamentSensor.** FAS- F-actin structures. Top row depicts data for 4 hours and bottom row for 24 hours reagent treatment. Data are mean ± SEM, *p<0.05, **p<0.01, ***p<0.001, ****p<0.0001 by one-way ANOVA with Tukey's multiple comparisons. TNF-in – TNF-α inhibitor, Y-27 – ROCK inhibitor Y-27632, Tα +Y-27 - TNF-α inhibitor + ROCK inhibitor Y-27632.

#### *2.3.1.5 TNF-α increases aSMA positive myofibroblast differentiation*

Analysis of aSMA staining and its association with stress fibers, led to detection of aSMA positive cells in almost all experimental groups (Figure 2.11). However, the percentage in each group varied (Table 2.2).

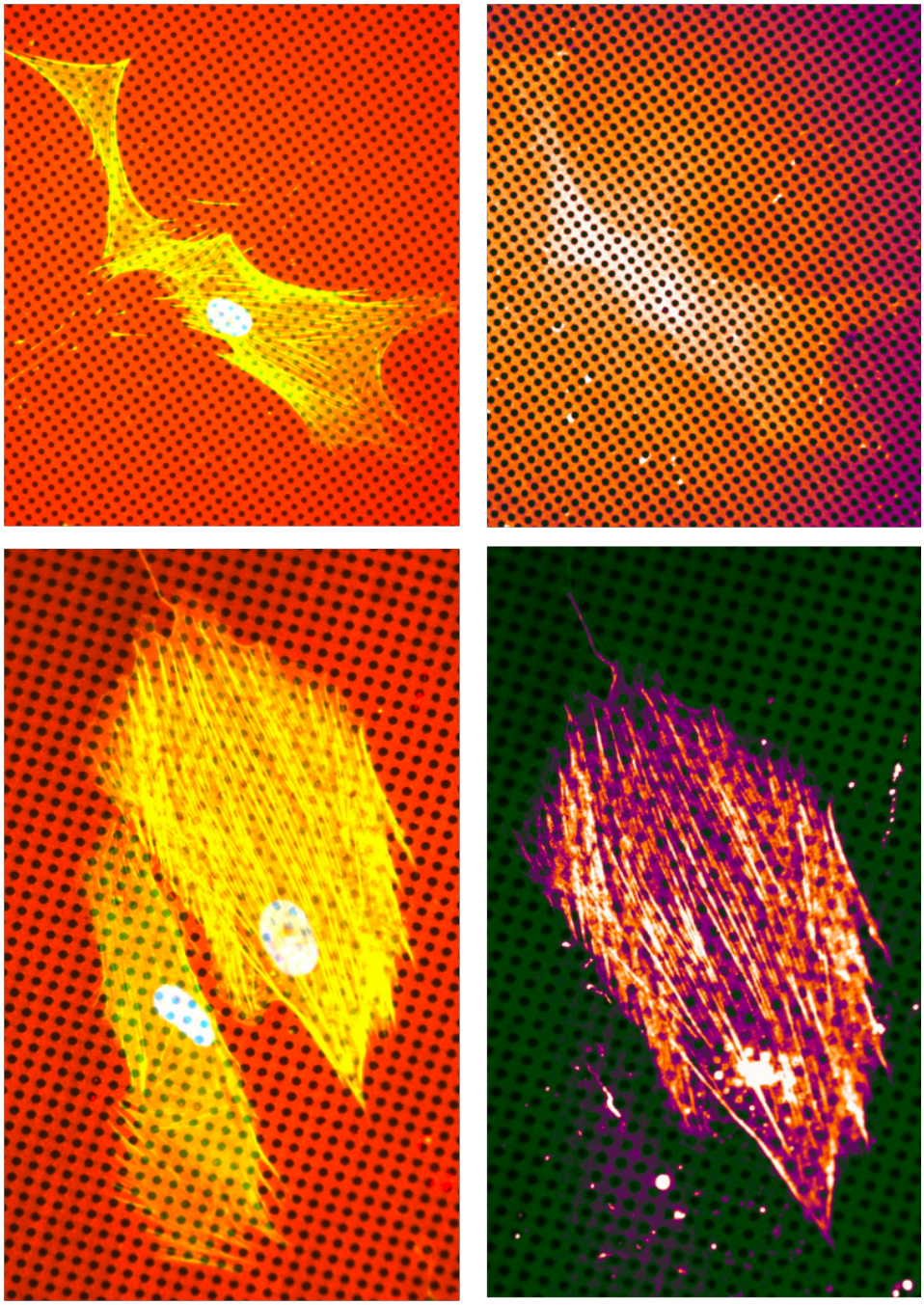

**Figure 2.11. Criteria for aSMA positive classification.** Top row depicts cell with F-actin staining (left) and aSMA staining (right) which is diffuse. Hence, this cell is considered to be aSMA negative. Bottom panel shows aSMA staining associated with stress fibers in the cell on the right image, hence it is considered to be aSMA positive.

**Table 2.2. Number of aSMA positive cells per experimental group**

| | Control | TNF-α | T-in | DMSO | Y-27 | Tα + Y-27 |
|---|---|---|---|---|---|---|
| **aSMA positive cells (%)** | 20.00 | 35.19 | 22.58 | 16.67 | 6.06 | 13.79 |
| | 10.42 | 22.64 | 13.64 | 7.69 | 8.93 | 14.10 |
| | 3.03 | 15.22 | 7.27 | 7.41 | 0.00 | 13.51 |

(TNF-in – TNF-α inhibitor, Y-27 – ROCK inhibitor Y-27632, Tα+Y-27 - TNF-α inhibitor + ROCK inhibitor Y-27632.)

TNF-α had the highest number of aSMA positive myofibroblasts amongst all groups. The number of aSMA positive cells were significantly higher in both TNF-α and TNF-inhibitor groups compared to the control group (Figure 2.12).

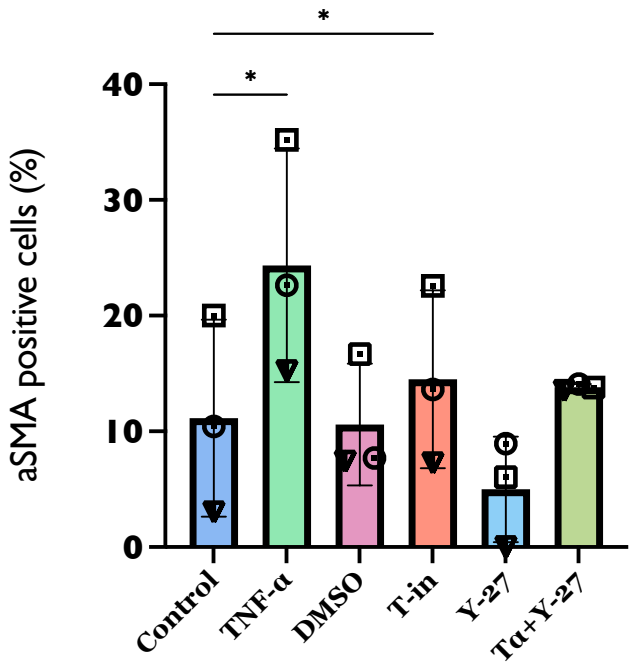


**Figure 2.12. Number of aSMA positive cells in experimental groups after 4 hours of reagent treatment.** Data are mean ± SEM, *p<0.05, **p<0.01, ***p<0.001, ****p<0.0001 by repeated measures one-way ANOVA with Tukey's multiple comparisons **.** TNF-in – TNF-α inhibitor, Y-27 – ROCK inhibitor Y-27632, Tα +Y-27 - TNF-α inhibitor + ROCK inhibitor Y-27632.

### 2.3.1.6 *ASMA positive cells in control group are significantly larger, highly contractile with longer and more stress fibers*

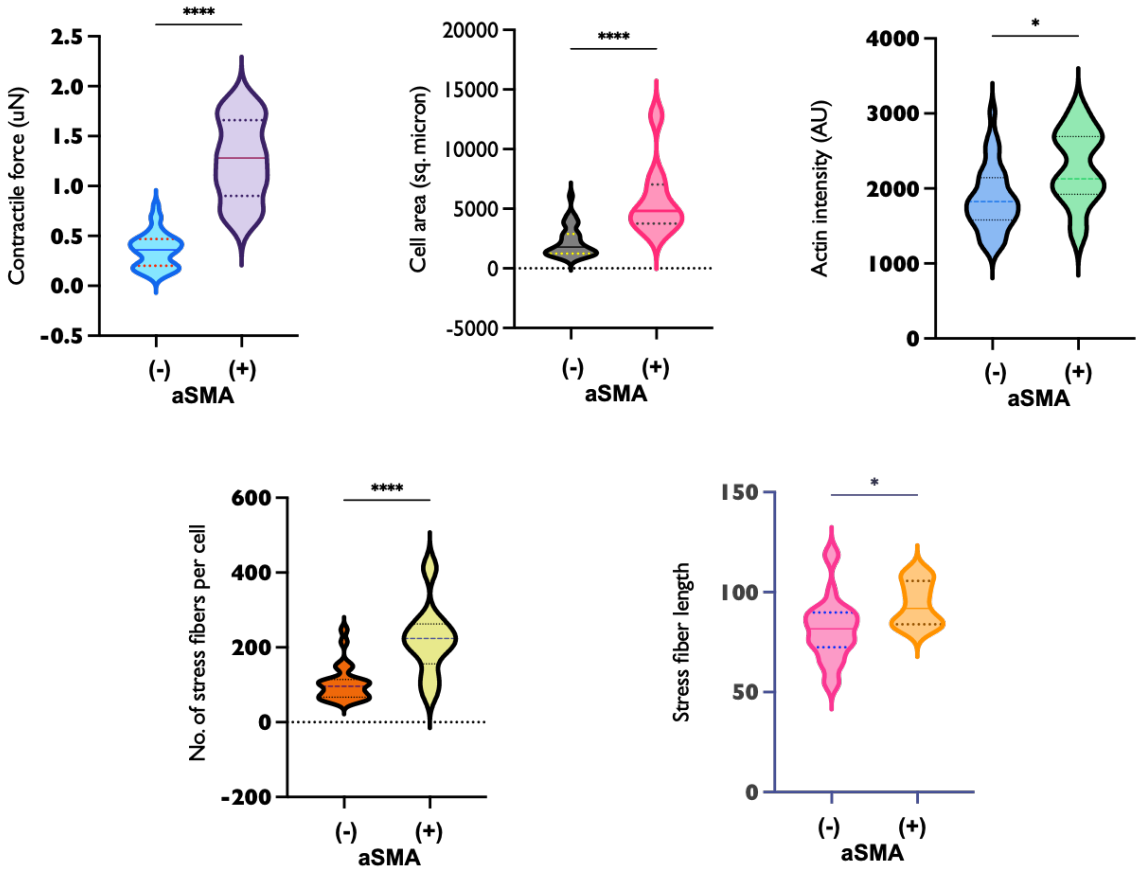


**Figure 2.13. Characteristics of aSMA positive cells in untreated control group.** Data are mean ± SEM, *p<0.05, **p<0.01, ***p<0.001, ****p<0.0001 by unpaired t-test.

When aSMA positive cells in the control group were compared with aSMA negative cells, they were significantly larger and generated significantly greater contractile forces. ASMA positive cells or myofibroblasts also had a significantly greater number of stress fibers which also were longer and stained more intensely compared to the aSMA negative cells (Figure 2.13).

### *2.3.1.7 ASMA positive cells in TNF-α treated group were significantly larger and more contractile*

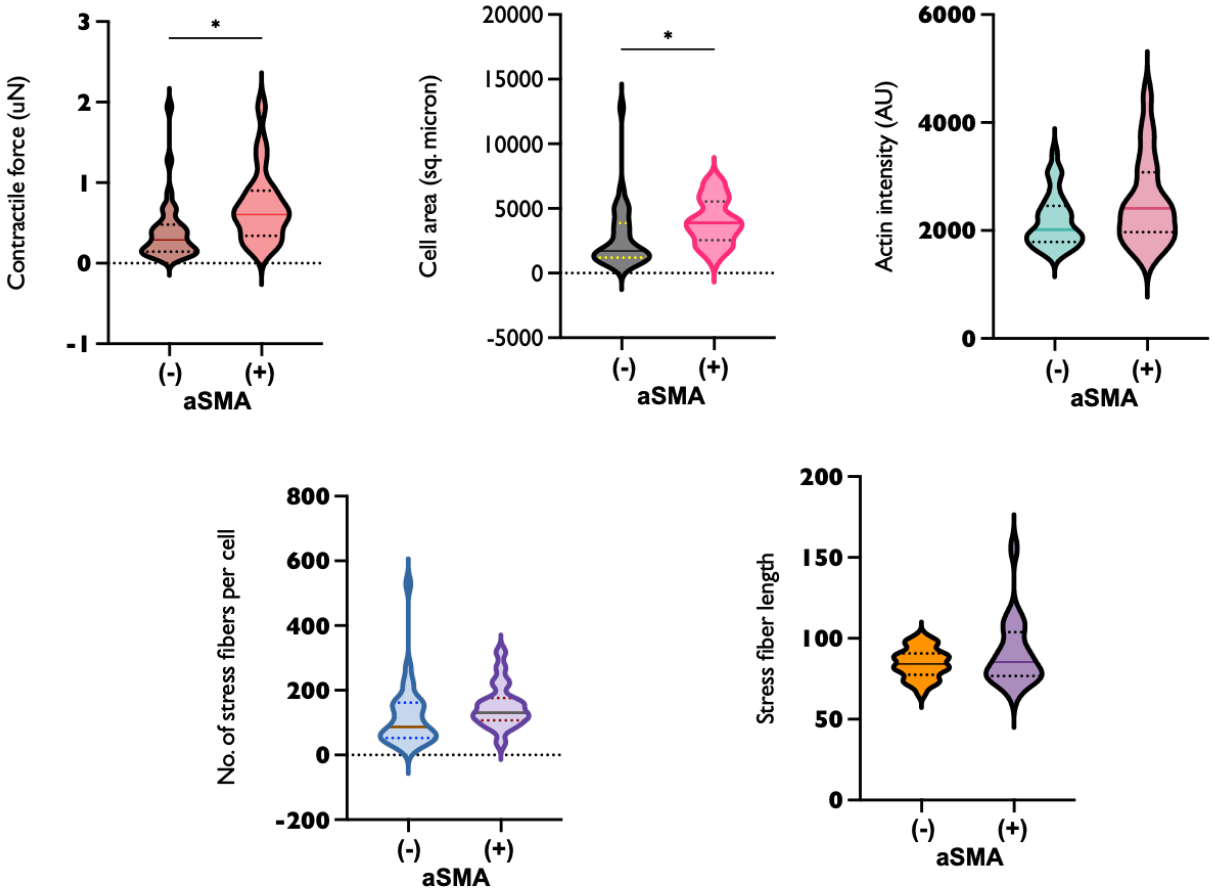


**Figure 2.14. Characteristics of aSMA positive cells in TNF-α treated group.** Data are mean ± SEM, *p<0.05, **p<0.01, ***p<0.001, ****p<0.0001 by unpaired t-test.

Myofibroblasts that were aSMA positive in the TNF-α treated group were also significantly larger and highly contractile compared to the aSMA negative controls in the group. However, no significant differences in F-actin intensity, and number and length of stress fibers were found between the aSMA positive and negative cells in the TNF-α treated group (Figure 2.14).

### 2.3.1.8 *Myofibroblasts in TNF-α group had significantly lower contractile force and stress fiber numbers compared to untreated controls*

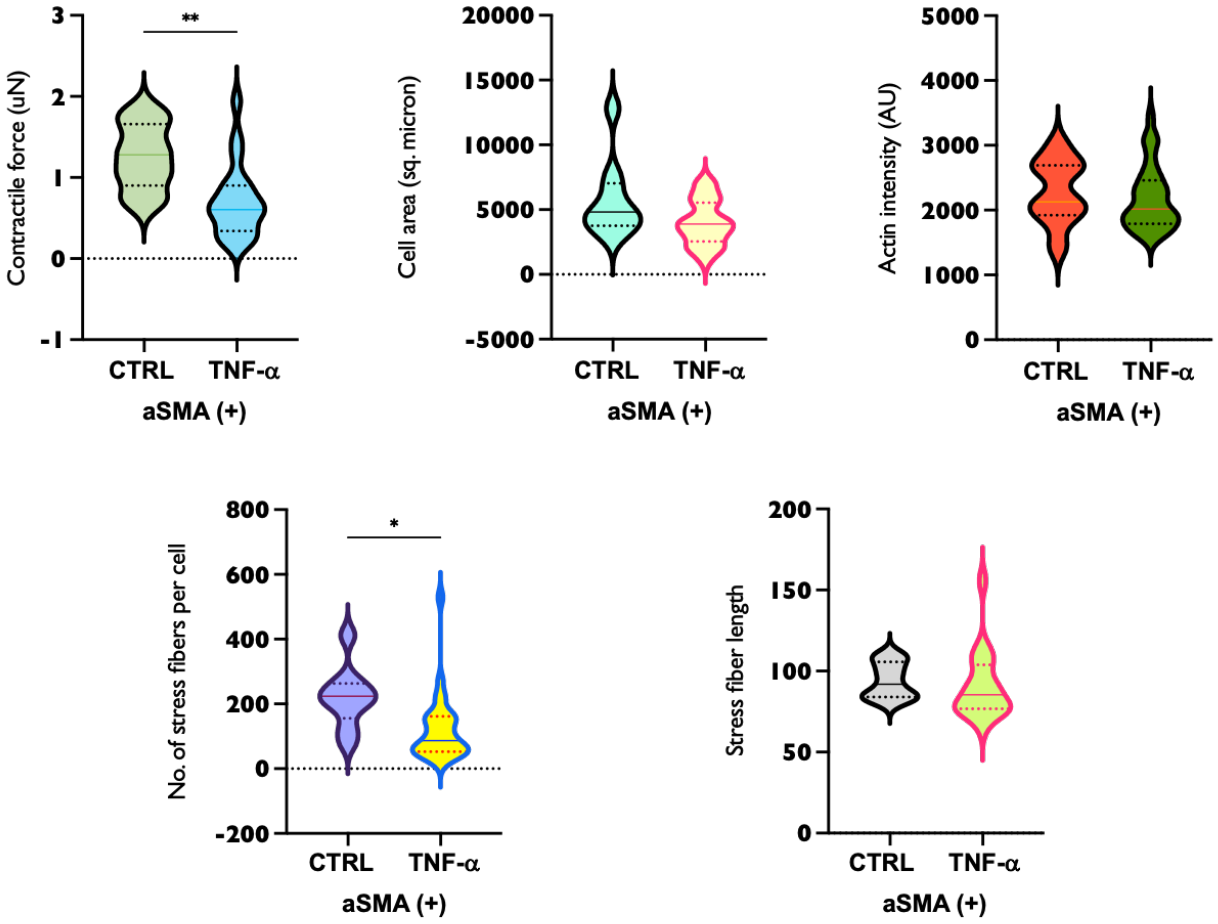


**Figure 2.15. Comparison of aSMA positive cells in control versus TNF-α treated group.** Data are mean ± SEM, *p<0.05, **p<0.01, ***p<0.001, ****p<0.0001 by unpaired t-test. CTRL – Control.

When myofibroblasts that were aSMA positive in the TNF-α treated group were compared with aSMA positive myofibroblasts in the untreated control group, there was statistically significant lowering of contractile force and stress fiber numbers in the TNF-α treated group. However, cell area, F-actin intensity and stress fiber length were not significantly different between the two myofibroblast groups (Figure 2.15).

### 2.3.2 Osteogenic differentiation experiments

#### 2.3.2.1 Alkaline phosphatase levels

After treating experimental groups with OIM for 10 days, an ALP assay was carried out to detect osteoblast differentiation. No significant differences in ALP levels amongst any of the groups were noted (Figure 2.16).

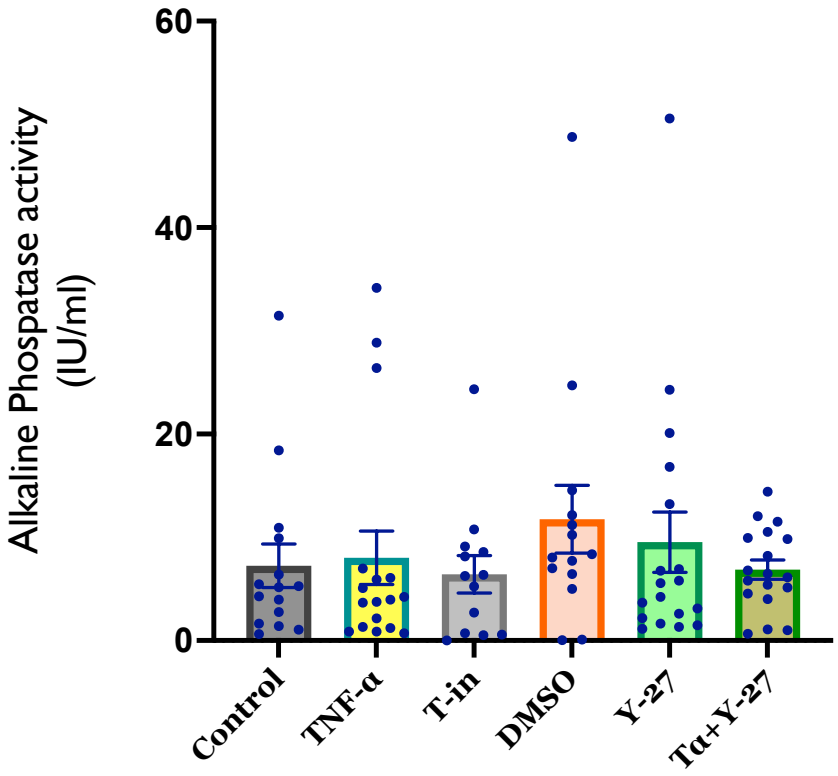


**Figure 2.16. Alkaline phosphatase assay.** Data are mean ± SEM, *p<0.05, **p<0.01, ***p<0.001, ****p<0.0001 by repeated measures one-way ANOVA with Tukey's multiple comparisons. TNF-in – TNF-α inhibitor, Y-27 – ROCK inhibitor Y-27632, Tα +Y-27 - TNF-α inhibitor + ROCK inhibitor Y-27632.

#### *2.3.2.2 Alizarin red assay*

To detect mineral deposition by differentiated osteoblasts, alizarin red assay was carried out after treating each experimental group with OIM for 28 days. Mineral deposits in all groups were found to be significantly lower compared to the control group (Figure 2.17).

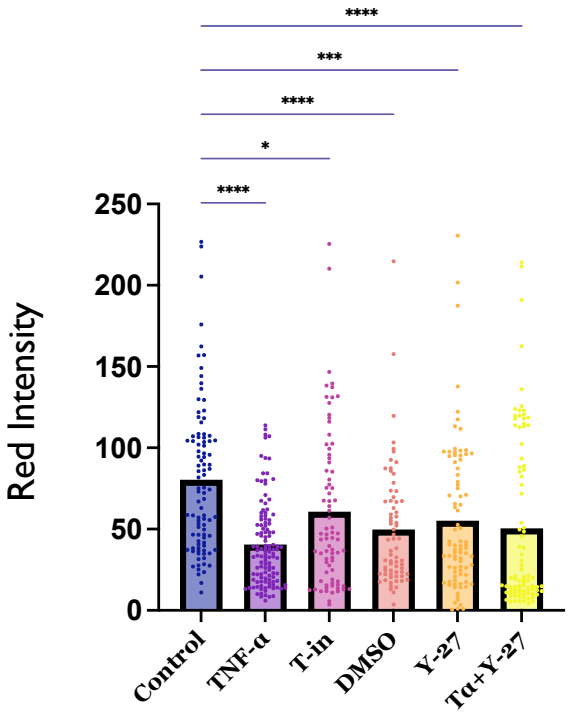


**Figure 2.17. Alizarin red assay.** Data are mean ± SEM, *p<0.05, **p<0.01, ***p<0.001, ****p<0.0001 by repeated measures one-way ANOVA with Tukey's multiple comparisons. TNF-in – TNF-α inhibitor, Y-27 – ROCK inhibitor Y-27632, Tα +Y-27 - TNF-α inhibitor + ROCK inhibitor Y-27632.

## 2.4 DISCUSSION

Periodontal function and health are greatly dependent on the structural integrity of its three component layers of cementum, ligament and alveolar bone. Hence, the ability to direct region-specific cell differentiation that produces targeted regeneration of a specific periodontal layer has been direly sought but continues to elude researchers. This application has profound utility for clinical scenarios involving periodontal disease treatment, periodontal regeneration and

orthodontic tooth movement. My research in this chapter hence intended to address this problem by investigating if the cytoskeletal element in the periodontal cells is linked in determining cellular function including differentiation - in short, to detect the link between form and function at a single cell level so that it can be potentially harnessed as a therapeutic target for directed cell differentiation. In particular, this study investigated if biochemical mediators like TNF-$\alpha$ influence cell cytoskeleton and mechanical properties via the Rho/ ROCK pathway, to regulate osteogenic differentiation. Using the novel reference-free TFM technique called black dots pioneered in the Sniadecki lab, I quantified F-actin stress fiber properties and contractile forces of 1,617 single cells obtained from healthy periodontium of extracted human premolars (Table 2.1). Contractile forces generated by PDL cells ranged from 0.4 to 1.3 $\mu$N. This is the first time that periodontal cell contractile forces have been quantified. Cellular contractile forces are crucial for cellular functions like cell division, differentiation, migration and survival (Chen et al. 1997, Polachek and Chen 2011). Quantifying these contractile forces in PDL cells is hence essential to assess how cellular functions can be modified and controlled by targeting the contractile structural elements.

This study also demonstrates how high-yielding the black dots technique can be, facilitating biomechanical and structural analysis of thousands of cells. Evaluation of cell morphology using the BD technique showed the formation of dendrite-like processes in the group treated with ROCK inhibitor Y-27632. This finding is consistent with a previous study by Lakshman et al. 2007 where ROCK inhibition caused cells to become elongated. Importantly, we were also able to detect the myofibroblast phenotype in our cell population based on their F-actin structure and high contractile force production. Myofibroblasts in the PDL cell population untreated with any reagents (control group), had significantly higher contractile force averaging 1.3 $\mu$N compared to 0.4 $\mu$N contractile force produced by aSMA negative non-myofibroblastic cells (Figure 2.13). Interestingly, although TNF-$\alpha$ caused a significantly higher number of cells to undergo myofibroblastic transformation

(Table 2.2, Figure 2.12), TNF- $\alpha$ induced myofibroblasts had a lower contractile force averaging 0.7 $\mu$N compared to 1.3 $\mu$N of the untreated control myofibroblasts (Figure 2.15). ASMA expressing cells are known osteoprogenitors (Meng et al. 2010, San Miguel et al. 2010, Roguljic et al. 2016, Matthews et al. 2020) whose numbers TNF-$\alpha$ increases, but whose contractile force is reduced by TNF-$\alpha$ treatment. These findings raise the question if cell phenotype is determined by modifying the magnitude of contractile force generated by the cytoskeleton, all other factors remaining the same. TNF-$\alpha$ is a central regulator of periodontal health and disease. Its periodontal levels are elevated during orthodontic treatment, autoimmune disorders, periodontitis, several systemic diseases and lately COVID. My study identifies one of the structural elements through which TNF-$\alpha$ may regulate periodontal cell differentiation - aSMA stress fibers. With further research, targeting aSMA stress fibers as an intervention should be explored to modulate TNF-$\alpha$ activity and direct periodontal stem / progenitor cell differentiation per clinical needs of patients. Developing such therapeutic interventions will be a step towards precision dentistry and can potentially benefit millions of patients seeking treatments like orthodontics, periodontal repair and regeneration.

Limitations of the current study are that the observations are based on only one donor cell population. Additional experiments with more donor cell populations should be able to give a clearer picture. The osteogenic experiments were too variable to make any conclusive inferences. Collecting more data from different donors should be able to clarify this issue as well, since the sample size and number of independent experiments will increase.

## 2.5 CONCLUSION AND FUTURE DIRECTIONS

Using the novel reference-free traction-free microscopy technique, black dots, we have quantified contractile forces of periodontal cells for the first time. This study also demonstrates how this technique can be utilized to perform a high-yield analysis of single cell morphology, F-actin stress fibers and contractile forces. We were also able to detect the presence of myofibroblasts and quantify their contractile forces which per our knowledge, has not been done before on periodontal cells. Stress fiber features and myofibroblast differentiation supported our hypothesis that TNF-$\alpha$ upregulates cellular F-actin and increases contractile forces. The BD technique can be used for drug development, testing biological agents and elucidating molecular mechanisms at a single cell level. Current observations provide basis to plan and conduct future studies that investigate directed differentiation of PDL stem / progenitor cells by targeting aSMA stress fibers in periodontal cells.

## 2.6 REFERENCES

Algate K, Haynes DR, Bartold PM, Crotti TN, Cantley MD. The effects of tumour necrosis factor-α on bone cells involved in periodontal alveolar bone loss; osteoclasts, osteoblasts and osteocytes. J Periodontal Res. 2016;51(5):549-66.

Basaran G, Ozer T, Kaya FA, Kaplan A, Hamamci O. Interleukine-1beta and tumor necrosis factor-alpha levels in the human gingival sulcus during orthodontic treatment. Angle Orthod. 2006;76:830–836.

Blair D, Dufresne E. The matlab particle tracking code repository. Particle-tracking code available at http://physics. georgetown. edu/matlab. 2008.

Beussman KM, Mollica MY, Leonard A, Miles J, Hocter J, Song Z, Stolla M, Han SJ, Emery A, Thomas WE, Sniadecki NJ. Black dots: High-yield traction force microscopy reveals structural factors contributing to platelet forces. Acta biomaterialia. 2023;163:302-11.

Campos SB, Ashworth SL, Wean S, et al. Cytokine-induced F-actin reorganization in endothelial cells involves RhoA activation. Am J Physiol Renal Physiol. 2009;296(3):F487–F495.

Chen CS, Mrksich M, Huang S, Whitesides GM, Ingber DE. Geometric control of cell life and death. Science. 1997;276(5317):1425-8.

Eltzner B, Hauke L, Huckemann S, Rehfeldt F, Wollnik C. A Statistical and Biophysical Toolbox to Elucidate Structure and Formation of Stress Fibers. Nanoscale Photonic Imaging. 2020:263-82.

Feghhi S, Munday AD, Tooley WW, Rajsekar S, Fura AM, Kulman JD, López JA, Sniadecki NJ. Glycoprotein Ib-IX-V complex transmits cytoskeletal forces that enhance platelet adhesion. Biophys J. 2016;111(3):601-8.

Grant M, Wilson J, Rock P, Chapple I. Induction of cytokines, MMP9, TIMPs, RANKL and OPG during orthodontic tooth movement. Eur J Orthod. 2013;35(5):644-51. doi: 10.1093/ejo/cjs057. Epub 2012 Sep 17. PMID: 22987319.

Goldberg MT, Han YP, Yan C, Shaw MC, Garner WL. TNF-α suppresses α-smooth muscle actin expression in human dermal fibroblasts: an implication for abnormal wound healing. J Invest Dermatol. 2007;127(11):2645-55.

Jäger A, Zhang D, Kawarizadeh A, Tolba R, Braumann B, Lossdörfer S, Götz W. Soluble cytokine receptor treatment in experimental orthodontic tooth movement in the rat. Eur J Orthod. 2005;27(1):1-1.

Kim HG, Kim JY, Gim MG, Lee JM, Chung DK. Mechanical stress induces tumor necrosis factor-α production through Ca2+ release-dependent TLR2 signaling. Am J Physiol Cell Physiol. 2008;295(2):C432-9.

Lakshman N, Kim A, Bayless KJ, Davis GE, Petroll WM. Rho plays a central role in regulating local cell-matrix mechanical interactions in 3D culture. Cell Motil Cytoske. 2007;64(6):434-45.

Lee SY, Zaske AM, Novellino T, Danila D, Ferrari M, Conyers J, Decuzzi P. Probing the mechanical properties of TNF-α stimulated endothelial cell with atomic force microscopy. Int J Nanomedicine. 2011:179-95.

Leong KG, Karsan A. Invited Reviews-Signaling pathways mediated by tumor necrosis factor a. Histol Histopathol. 2000;15(4):1303.

Liu X, Tan GR, Yu M, Cai X, Zhou Y, Ding H, Xie H, Qu F, Zhang R, Lam CU, Cui P. The effect of tumour necrosis factor-α on periodontal ligament stem cell differentiation and the related signaling pathways. Curr Stem Cell Res Ther. 2016;11(7):593-602.

MacEwan DJ. TNF ligands and receptors--a matter of life and death. Br J Pharmacol. 2002;135(4):855-75. doi: 10.1038/sj.bjp.0704549. PMID: 11861313; PMCID: PMC1573213.

MacNearney D, Mak B, Ongo G, Kennedy TE, Juncker D. Nanocontact printing of proteins on physiologically soft substrates to study cell haptotaxis. Langmuir. 2016;32(50):13525-33.

Martino F, Perestrelo AR, Vinarský V, Pagliari S, Forte G. Cellular mechanotransduction: from tension to function. Front Physiol. 2018;9:824.

Matthews BG, Wee NK, Widjaja VN, Price JS, Kalajzic I, Windahl SH. αSMA osteoprogenitor cells contribute to the increase in osteoblast numbers in response to mechanical loading. Calcif Tissue Int. 2020;106(2):208-17.

McBeath R, Pirone DM, Nelson CM, Bhadriraju K, Chen CS. Cell shape, cytoskeletal tension, and RhoA regulate stem cell lineage commitment. Dev Cell. 2004;6(4):483-95.

Meikle MC. The tissue, cellular, and molecular regulation of orthodontic tooth movement: 100 years after Carl Sandstedt. Eur J Orthod. 2005;28:221–40. doi:10.1093/ejo/cjl001.

Meng Y, Han X, Huang L, Bai D, Yu H, He Y, Jing Y. Orthodontic mechanical tension effects on the myofibroblast expression of alpha-smooth muscle actin. The Angle Orthodontist. 2010;80(5):912-8.

Nanes MS. Tumor necrosis factor-α: molecular and cellular mechanisms in skeletal pathology. Gene. 2003 4;321:1-5.

Obenaus AM, Mollica MY, Sniadecki NJ. (De) form and function: measuring cellular forces with deformable materials and deformable structures. Adv Healthc Mater. 2020;9(8):1901454.

Osta B, Benedetti G, Miossec P. Classical and paradoxical effects of TNF-α on bone homeostasis. Front. immunol. 2014;5:80339.

Palchesko RN, Zhang L, Sun Y, Feinberg AW. Development of polydimethylsiloxane substrates with tunable elastic modulus to study cell mechanobiology in muscle and nerve. PloS one. 2012;7(12):e51499.

Papadopoulou A, Cantele A, Koletsi D, Eliades T, Kletsas D. Short-and long-term treatment with TNF-α inhibits the induction of osteoblastic differentiation in cyclic tensile-stretched periodontal ligament fibroblasts. Eur J Orthod. 2020;42(4):396-406.

Polacheck WJ, Chen CS. Measuring cell-generated forces: a guide to the available tools. Nat Methods. 2016;13(5):415-23.

Putra VD, Kilian KA, Knothe Tate ML. Biomechanical, biophysical and biochemical modulators of cytoskeletal remodelling and emergent stem cell lineage commitment. Commun Biol. 2023;6(1):75.

Ren Y, Hazemeijer H, de Haan B, Qu N, de Vos P. Cytokine profiles in crevicular fluid during orthodontic tooth movement of short and long durations. J Periodontol. 2007;78(3):453-8. doi: 10.1902/jop.2007.060261. PMID: 17335368.

Rodriguez ML, Beussman KM, Chun KS, Walzer MS, Yang X, Murry CE, Sniadecki NJ. Substrate stiffness, cell anisotropy, and cell–cell contact contribute to enhanced structural and calcium handling properties of human embryonic stem cell-derived cardiomyocytes. ACS Biomater Sci Eng. 2019;5(8):3876-88.

Roguljic H, Matthews BG, Yang W, Cvija H, Mina M, Kalajzic I. In vivo identification of periodontal progenitor cells. J Dent Res. 2013;92(8):709-15.

San Miguel SM, Fatahi MR, Li H, Igwe JC, Aguila HL, Kalajzic I. Defining a visual marker of osteoprogenitor cells within the periodontium. J Periodontol Res. 2010;45(1):60-70.

Takemura AI, Nakagawa S, Kawai H, Inaba T, Kato S, Hamada, Amano A. Inhibitory effects of tumor necrosis factor-alpha on migration of human periodontal ligament cells. J Periodontol. 2006;77(5): 883-890.

Urbano RL, Furia C, Basehore S, Clyne AM. Stiff substrates increase inflammation-induced endothelial monolayer tension and permeability. Biophys J. 2017;113(3):645-55.

Wang L, Sun B, Ziemer KS, Barabino GA, Carrier RL. Chemical and physical modifications to poly (dimethylsiloxane) surfaces affect adhesion of Caco-2 cells. J Biomed Mater Res A. 2010;93(4):1260-71.

Yamamoto T, Ugawa Y, Kawamura M, Yamashiro K, Kochi S, Ideguchi H, Takashiba S. Modulation of microenvironment for controlling the fate of periodontal ligament cells: the role of Rho/ROCK signaling and cytoskeletal dynamics. Cell Commun Signal. 2018;12(1):369-78

Yoshimatsu M, Shibata Y, Kitaura H, Chang X, Moriishi T, Hashimoto F, Yoshida N, Yamaguchi A. Experimental model of tooth movement by orthodontic force in mice and its application to tumor necrosis factor receptor-deficient mice. J Bone Miner Metab. 2006;24(1):20-7. doi: 10.1007/s00774-005-0641-4. PMID: 16369894.

Yu H, Xiong S, Tay CY, Leong WS, Tan LP. A novel and simple microcontact printing technique for tacky, soft substrates and/or complex surfaces in soft tissue engineering. Acta biomaterialia. 2012 Mar 1;8(3):1267-72.

Yucel-lindberg T, Båge T. Inflammatory mediators in the pathogenesis of periodontitis. Expert Rev Mol Med 2013; 15: 1-22.

# CHAPTER 3. ENGINEERED 3D PERIODONTAL LIGAMENT MODEL WITH MAGNETIC TENSILE LOADING

## 3.1 ABSTRACT

*In vitro* models are invaluable tools for deconstructing the biological complexity of the periodontal ligament (PDL). Model systems that closely reproduce the three-dimensional (3D) configuration of cell-cell and cell-matrix interactions in native tissue can deliver physiologically relevant insights. However, 3D models of the PDL that incorporate mechanical loading are currently lacking. Hence, we developed a model where periodontal tissue constructs (PTCs) are made by casting PDL cells in a collagen gel suspended between a pair of slender, silicone posts for magnetic tensile loading. Specifically, one of the posts was rigid and the other was flexible with a magnet embedded in its tip so that PTCs could be subjected to tensile loading with an external magnet. Additionally, the deflection of the flexible post could be used to measure the contractile force of PDL cells in the PTCs. Prior to tensile loading, second harmonics generation analysis of collagen fibers in PTCs revealed that incorporation of PDL cells resulted in collagen remodeling. Biomechanical testing of PTCs by tensile loading revealed an elastic response at four hours, permanent deformation by one day, and creep elongation by one week. Subsequently, contractile forces of PDL cells were substantially lower for PTCs under tensile loading. Immunofluorescence analysis revealed that tensile loading caused PDL cells to increase in number, express higher levels of F-actin and alpha smooth muscle actin and become aligned to the tensile axis. Second harmonics generation analysis indicated that collagen fibers in PTCs progressively remodeled over time with tensile loading. Gene expression analysis also confirmed tension-mediated activation of the Rho/ROCK pathway and osteogenic genes. Our model is novel in demonstrating the mechanobiological behavior that results in cell-mediated remodeling of the PDL tissue in a 3D context. Hence, it can

be a valuable tool to develop therapeutics for periodontitis, periodontal regeneration, and orthodontics.

## 3.2 INTRODUCTION

The periodontal ligament (PDL) processes mechanical loads by modulating its biomechanical properties and cellular functions to ensure homeostasis during health, and repair and remodeling during disease or injury. Obtaining mechanistic insights into these mechanoresponses is necessary to develop newer therapeutic interventions for periodontitis, periodontal regeneration and orthodontic tooth movement. However, the architectural arrangement of an extremely narrow (150 to 380 microns) band of soft PDL tissue bonded to bone and cementum on either side renders *in vivo* PDL difficult to study (Beertsen et al. 1997). Consequently, periodontal research has depended heavily on *in vivo* animal, *in vitro* and *in silico* models of the PDL. *In vitro* models have the distinct advantages of simplifying biological complexity, facilitating reductionist hypothesis testing and experimentation at multiple scales – cellular, molecular and tissue-level. In particular, mechanical *in vitro* models are indispensable to investigate signaling pathways and molecular mechanisms that drive tissue behavior and cellular activity in response to mechanical loads.

Two-dimensional (2D) *in vitro* mechanical models that deform cell monolayers on substrates have been the most widely used (Yang et al. 2015). However, observations in 2D models significantly differ from that in three-dimensional (3D) models. This is due to their lack of multi-dimensional cell-cell and cell-extracellular matrix (ECM) networks necessary for effective mechanotransduction provided by the 3D environment (Kang et al. 2013). 3D architecture is also vital for recreating the concentration gradient of signaling molecules inherent in *in vivo* tissues to observe the gradient-dependent cell responses to applied stresses. Considering their

advantages, innovations in the fields of tissue engineering and biomaterials like microfluidics and 3D bioprinting have been recently harnessed to develop 3D PDL models (Huang et al. 2023).

3D *in vitro* PDL models are mainly categorized as either for inducing periodontal regeneration or for testing mechanical loading (Aveic et al. 2021). PDL regeneration 3D models meant for *in vivo* implantation seed PDL cells in either a scaffold-free matrix or scaffold of biomimetic polymers, ceramics, hydrogels or self-assembling peptides. In mechanical testing 3D models, PDL cells have been seeded in various receptacles of matrix materials like hyaluronan, gelatin, or type I collagen (Yang et al. 2015). An important advantage of 3D *in vitro* mechanical models is that they facilitate interrogation of mechanical stress-mediated alteration of PDL biomechanical parameters such as stiffness, viscoelasticity and strain at the tissue level. Tissue biomechanical properties are established critical drivers of cell structure which in turn determines cell lineage specification and function (McBeath et al. 2004, Yamamoto et al. 2018). Hence, 3D in vitro models that facilitate research into the PDL biomechanical properties-structure-function link can be invaluable to identify therapeutic targets to control PDL cell differentiation and tissue remodeling.

Successful clinical translation using *in vitro* models can be enhanced if investigative findings from models approximate physiological conditions *in vivo*. For that, the 3D *in vitro* models need to match the spatial arrangement and structure of *in vivo* tissue as closely as possible, which is lacking in existing models. Additionally, the difficulty of applying tensile stresses to current 3D models has been a significant hindrance for periodontal mechanobiology investigations (Yang et al. 2015). To address these problems, the present research was conducted with two main objectives, to – 1) engineer a 3D *in vitro* PDL model that recapitulates key elements of native periodontal architecture and 2) design and test a magnet-based tensile stretching system on the model. This chapter will provide the proof-of-principle for this model through fabrication of 3D PDL tissue masses, consisting of human PDL cells embedded in a collagen matrix hydrogel, called

periodontal tissue constructs (PTCs). An in-depth investigation of tensile stretching effects on PTCs was then conducted. Tensile stretch, as during orthodontic force application, has been associated with cell proliferation, collagen remodeling, elevated cellular F-actin and alpha-smooth muscle actin (aSMA) levels and osteogenic gene expression changes (Mabuchi et al. 2002; Martino et al. 2004; Kook et al. 2011; Huang et al. 2016; Yamamoto et al. 2018; Sun et al. 2021; Janjić 2023). This chapter presents data on these parameters and demonstrates the feasibility of the PTC platform as a model of the PDL in future studies.

## 3.3 MATERIALS AND METHODS

### *3.3.1 Isolating primary PDL cells*

PDL cells were harvested using pre-established protocols (Somerman et al. 1988) from the roots of healthy premolars, which had been extracted for orthodontic purposes in a 13 year-old male patient. Briefly, PDL tissue was gently dissected from the middle third of the tooth root surface in a culture dish containing wash buffer [Hanks' balanced salt solution (HBSS; Gibco) supplemented with 5% (v/v) fetal bovine serum (FBS; HyClone) and 50 U/mL penicillin and 50 µg/mL streptomycin]. The suspension was centrifuged at 400×g for 10 min at 4°C. After aspirating the supernatant, PDL tissue was digested in collagenase I (3 mg/mL, Sigma- Aldrich) and dispase II (4 mg/mL; Sigma-Aldrich) for 1 hour at 37°C. After digestion, the suspension was passed through a 70 µm strainer to obtain a single-cell suspension. The cell population was expanded by seeding the single-cell suspension in 24-well plates. Cells were grown in standard PDL cell culture medium of Dulbecco's Modified Eagle Medium (DMEM; Gibco) supplemented with 10% FBS (HyClone) and 1% penicillin/ streptomycin (Gibco) at 37°C with 5% $CO_2$. On reaching confluence, cells were washed with PBS, trypsinized with 0.25% trypsin-EDTA (Gibco) and passaged progressively into T-75 and T-175 flasks. Cells at passage numbers 1 to 3 were stored in freezing media

Cryostor (1 mL per 10 million cells) in a liquid nitrogen freezer then thawed, plated, and expanded as needed in T-75 and T-175 flasks. PDL cells between passage numbers 3 and 6 were used for the experiments.

### *3.3.2 Fabricating post arrays and PDMS wells*

To fabricate the post array, a four-part acrylic mold (designed in-house) was assembled (Figure 3.1). Capillary tubes with 1 mm outer diameter were cut into six 14 mm long sections. One section was placed in each of the six vertical post channels on one side of the assembled mold to prepare rigid posts. One neodymium magnet cube (1 $mm^3$, SuperMagnetMan) was inserted into each of the six contralateral vertical posts that would eventually become flexible posts. Two full-length 1.1 mm outer diameter capillary tubes were placed on either side of the mold base (for a total of 4) to

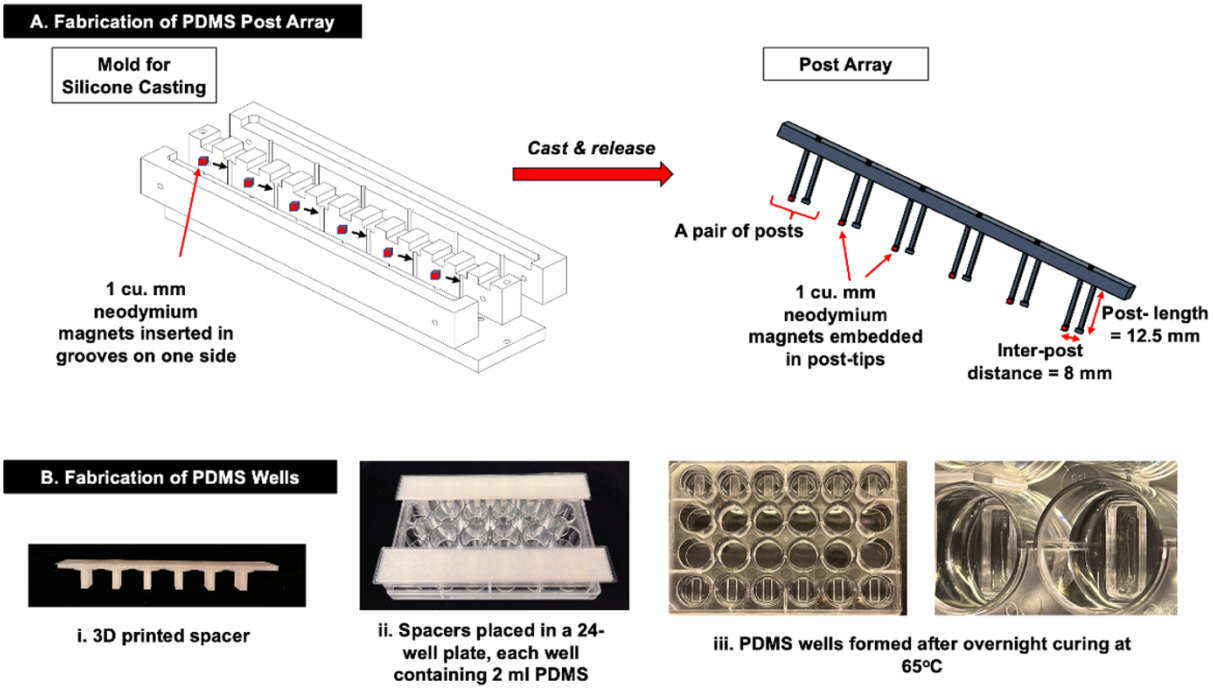


**Figure 3.1. Fabrication of PTC casting components**. (A) A 6-part acrylic mold is assembled. 1 cu mm magnets are inserted in mold grooves, PDMS is poured and cured overnight at 65ºC to fabricate silicone posts. (B) PDMS wells are fabricated in a 24-well plate by placing a 3D printed spacer in 2 mL PDMS per well and curing overnight at 65ºC.

provide structural support to the base. A 10:1 mixture of Sylgard 184 polydimethylsiloxane (PDMS; Krayden) was prepared by mixing 10 parts of base component with one part of curing agent for five minutes. After degassing the PDMS under vacuum to remove bubbles, it was poured into the mold and cured for 18 hours at 65°C. On cooling, the post array was then carefully cut from the mold using a razor blade. For preparing the PDMS wells, a polylactic acid (PLA) spacers measuring 12 mm in length, 4 mm in width, and 13 mm in height in an array were 3D printed in-house. A 24-well plate was plasma-treated for 60 seconds to enhance attachment of PDMS to wells. Two mL of degassed 10:1 PDMS mixture was dispensed in each well of the top row of the 24-well plate. The spacer array was then placed in the PDMS mixture in the 24-well plate and the assembly was cured overnight at 65°C. After removal from oven and cooling to room temperature, the spacer array was detached from the formed wells.

### *3.3.3 Casting tissues*

PTCs were cast between each post pair by modifying the protocol from two published techniques for engineered heart tissues (Bremner et al. 2022, Bhandari 2018) (Figure 3.2). Prior to casting, PDMS post arrays and 24-well plates with PDMS wells were submerged in 70% ethanol for 10 min, rinsed with sterile deionized water for 10 min, then UV sterilized for 10 min. Arrays were then transferred to the tissue-culture hood. PDMS wells were treated with 1 mL/well of 5% pluronic F-127 (Sigma-Aldrich) solution for 1 hour, then washed twice with 1 mL/well of DPBS and set aside to dry. Posts were then dipped sequentially in a 24-well plate containing 2.5 mL/well of 0.1% polyethylenimine (PEI) for 10 min, sterile deionized water for 5 min, 0.01% glutaraldehyde for 30 min, then rinsed twice in sterile DI water for 5 min and set aside to dry. Each PTC was cast from a 100 μL cell-collagen mixture composed of 1:4 ratio of PDL cell solution (20 μL culture media containing 300,000 PDL cells) and collagen mixture [80 μL of 9 parts of collagen (4 mg/mL; Advanced Biomatrix) mixed with 1 part of neutralization solution (Advanced Biomatrix)]. The

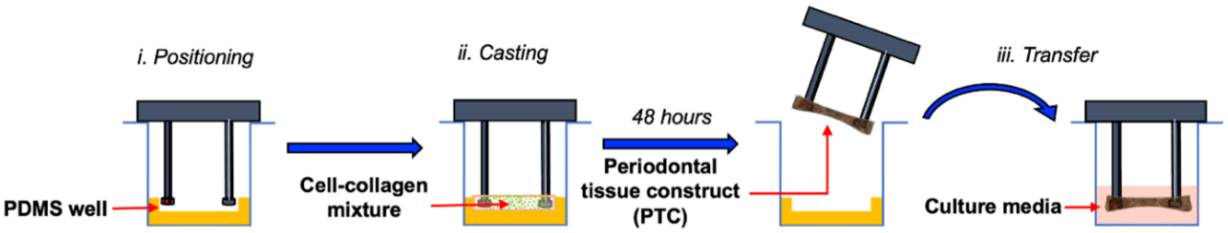


**Figure 3.2. Periodontal tissue constructs casting procedure.**

total volume of cell-collagen mixture for casting the required number of post arrays was calculated using these values as baseline. PDL cells were lifted using 0.25% Trypsin-EDTA (Gibco) and counted. The cell suspension containing the required number of total cells was separated, centrifuged at 1500 rpm for 5 min. The supernatant was aspirated, and cells were resuspended in the appropriate volume of culture medium based on the calculations. The collagen and neutralization solutions were placed on ice and mixed in 9:1 ratio. To this, the cell solution was added and gently mixed by triturating with the pipette to avoid air bubbles and then placed on ice. One hundred μL of this mixture was dispensed in each of the six PDMS wells in a 24-well plate. The post arrays were then inverted into this mixture gently, making sure they were aligned in the center of the well. The assembly transferred to the incubator at 37°C with 5% $CO_2$. After 90 min, 1 mL of culture media was gently added to the wells containing the cast PTCs and then incubated again at 37°C. After 48 hours, PTCs were transferred to a fresh 24-well plate with 2.5 mL/well of culture media, which was changed every 2 to 3 days. The same procedure was followed to cast a set of collagen only constructs (COC), consisting of only a 9:1 ratio of collagen and neutralization solution without any cell seeding.

### *3.3.4 Viability assessment*

PTCs were disassembled from posts and digested in collagenase I (3 mg/mL, Sigma- Aldrich) and dispase II (4 mg/mL; Sigma-Aldrich) solution for 45 min at 37$^{o}$C with occasional agitation using a P1000 pipette tip. After centrifugation at 1500 rpm for 5 min, supernatant was discarded. Sedimented tissue bits were re-suspended in 0.25% trypsin-EDTA (Gibco) while agitating consistently with a P1000 for 5 minutes to break down the cells. The suspension was passed through a 70 μM strainer to obtain a single-cell suspension. Cell viability was assessed by drawing 200 μL of the single cell solution in a Via-2 cassette and placing it in a Nucleocounter-NC 200 machine (ChemoMetec).

### *3.3.5 Calculation of PTC contractile force*

Based on a modulus of elasticity of 2.5 MPa for PDMS, the bending stiffness ($K_{post}$) of the flexible posts was calculated to be 0.95 μN/μm, as done previously (Bielawski et al. 2016). Contractile force was calculated by multiplying the bending stiffness by the deflection of the post ($\Delta_{post}$) (Figure 3.3).

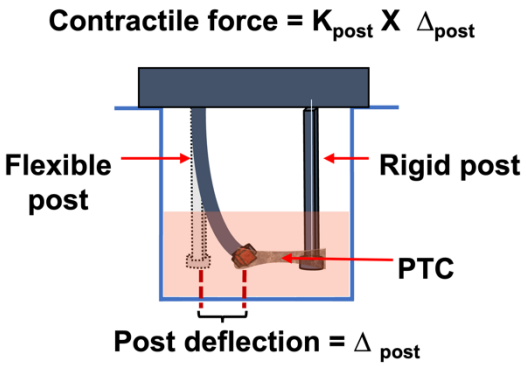


**Figure 3.3. Contractile force calculation for PTCs**

### 3.3.6 *Tensile loading of PTCs*

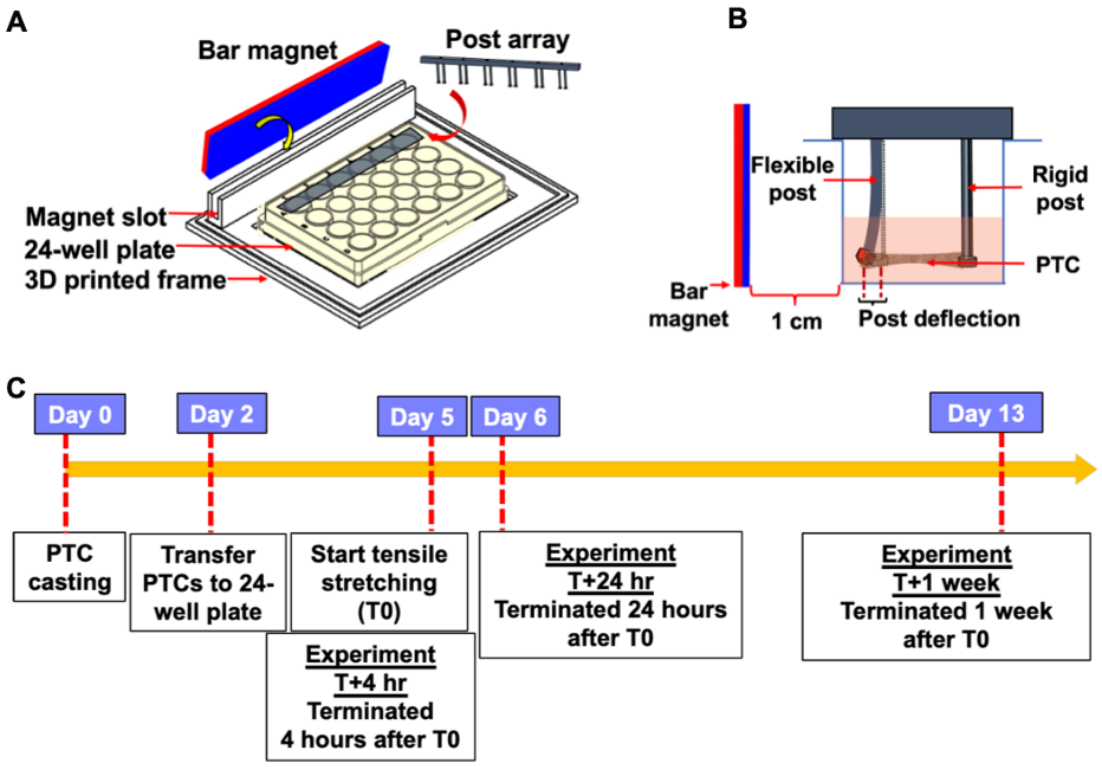


**Figure 3.4. Tensile stretching of PTCs.** (**A**) Schematic of tensile stretching apparatus and setup. (**B**) Schematic of tensile stretching of PTCs as viewed from side. (**C**) Experiment timeline.

A 14 × 17 mm tension apparatus to exert tensile stretch on PTCs was designed and printed in house using resin 3D printing material. The design included a slot to hold a 15 × 1 × 0.3 mm bar magnet (SuperMagnetMan) and another slot to seat a 24-well plate (Figure 3.4, A). For tensile loading, an array of PTCs was placed with flexible posts facing towards the bar magnet (Figure 3.4, B). At a separation of 1 cm, the attractive force between the bar magnet and embedded cube magnets in the flexible posts caused them to deflect. Prior to casting, post arrays were placed in the apparatus and the deflection of the posts was measured to be 430 ± 21 μm, which equates to

408.5 μN of force according to the bending stiffness. PTCs were loaded in the tensile apparatus five days after casting and subjected to tensile stretching for 4 hours, 24 hours, or one week (Figure 3.4, C). Images of the stretched PTCs and unstretched controls were taken with brightfield microscopy (Nikon Ti-E) using a 2X objective and then processed using FIJI image analysis software to calculate PTC length. Based on PTC length, contractile force produced after tensile loading was calculated as mentioned in the section above.

### *3.3.7 Immunofluorescence imaging*

PTCs on posts were fixed in 4% paraformaldehyde (PFA; VWR) at room temperature for 1 hour. PTCs were then dismounted from the posts for the immunofluorescence staining process. In short, PTCs were permeabilized with 0.2% Triton-X for 10 min followed by blocking with 10% normal goat serum (Invitrogen) for 10 min at room temperature. Samples were then incubated for 1 hour with mouse primary antibodies for alpha-smooth muscle actin (aSMA, Santa Cruz Biotechnology, 1:100), followed by 3X, 10 min PBS rinses on a room temperature shaker. PTCs were then treated with goat anti-mouse Alexa Fluor 488 (Invitrogen A28175, 1:200), Alexa Fluor 647 phalloidin (Invitrogen A22287, 1:400), and Hoechst 33342 (ThermoFisher, 1:1000). After 1 hour, PTCs were again rinsed thrice in PBS for 10 min each on a room temperature shaker. Whole PTCs were then coversliped in VECTASHIELD mounting medium and allowed to dry overnight. A Leica SP8 confocal microscope was used for imaging. Three to four images per PTC were obtained under 10X objective at 2X zoom and 1024 X 1024 resolution. Since three independent experiments were carried out and each experiment was conducted in triplicate, we ensured a minimum of 30 images per condition for analysis. Laser strength and gain were kept constant between all samples and fields of view. F-actin and aSMA fluorescence intensities were quantified using Fiji image analysis software. Cell alignment was calculated using the Directionality plugin in Fiji.

### *3.3.8 Collagen structural analysis*

PTCs while still on posts were fixed in 4% paraformaldehyde (PFA; VWR) for an hour at room temperature. They were then dismounted from the posts, rinsed in PBS and whole mounted on a slide using Fluoromount (ThermoFisher) mounting medium. Collagen structure in PTCs was assessed using multiphoton imaging to record the second harmonics generation (SHG) by collagen fibers. The whole mounted tissues were imaged on an Olympus FV1000MP microscope at 25X magnification, using 860 nm excitation from a Mai-Tai HP laser (Spectra Physics, 59% power) and a Violet/Green emission filter cube. Five zones in each whole mounted PTC were imaged. Each image was a Z-stack made up of 5 images with a 1.5-micron step, which were then condensed into maximum intensity projections using FIJI image analysis software. The SHG channel (violet) was quantified for fiber length, width, count and alignment using CurveAlign 5.0 beta in CT-FIRE fiber mode (Liu et al. 2020).

### *3.3.9 Gene expression analysis*

Following force assessment, PTCs stretched for 4 and 24 hours, and age-matched unstretched controls were flash frozen using liquid nitrogen and stored at −80°C. These samples were sent to BGI genomics for RNA extraction and 100 base pair paired-end transcriptome sequencing on the DNBseq platform with 50 million reads per sample. Expression quantification was done firstly by using Bowtie2 (Langmead et al. 2012) to map the clean reads to the reference gene sequence (transcriptome), and secondly using RSEM (Li and Dewey 2011) to calculate the gene expression level of each sample. Differential expression analysis was performed using DEGseq (Wang et al. 2010). In order to improve the accuracy of DEGs, genes with fold change >2 and Q-value ≤ 0.001, were classified as significant differentially expressed genes. According to the results of differential gene detection, the R package pheatmap was used to perform hierarchical clustering analysis on the union set of differential genes.

### 3.3.10 Statistical analysis

Data were collected from three independent experiments. All values are expressed as mean ± standard error of mean. Results were compared using an unpaired two-tail t-test or repeated measures ANOVA or one-way ANOVA with post-hoc comparisons using GraphPad Prism. Differences with p-values <0.05 were considered statistically significant.

## 3.4 RESULTS

### 3.4.1 PTCs exhibit cell-mediated contractility and ECM remodeling

A novel 3D *in vitro* PDL model was successfully fabricated by casting patient derived PDL cells in a collagen matrix between two silicone posts. Within 48 hours, the cell-collagen mixture had condensed into a polymerized mass of PDL tissue between the two posts (Figure 3.5). Each PTC measured approximately 7.5 mm (length) X 2 mm (width) X 0.5 mm (thickness).

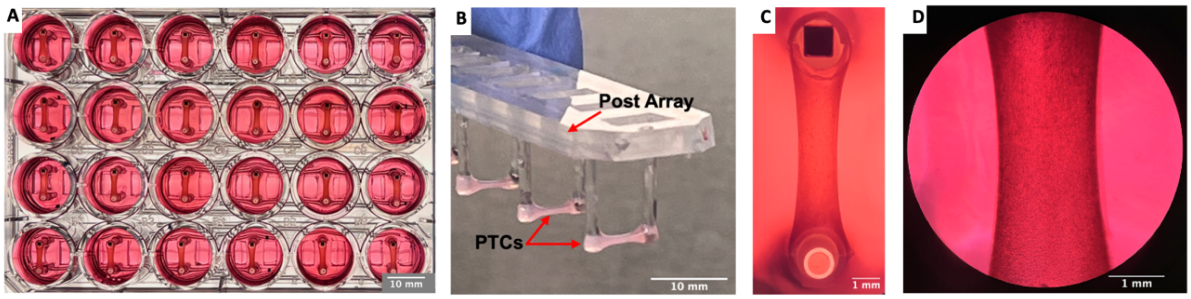


**Figure 3.5. Periodontal tissue constructs.** (**A**) PTCs in culture media in a 24-well plate. (**B**) PTCs on posts. (**C**) PTC observed under 1X brightfield microscope. Visible in the top post is the square cross-section of an embedded magnet for tensile loading and in the bottom post is the round cross-section of a glass capillary for rigid reinforcement. (**D**) PTC observed under 4X brightfield microscope.

Cells in the PTCs caused the 3D tissues to contract, pulling the flexible post towards the center, which was quantified as change in length and deflection of posts (Figure 3.6, A, B). Three days after casting, PTCs reduced in length to 7223 ± 37 μm, while collagen constructs without cells

were 8000 μm long (Figure 3.6, C). Based on the deflection of the posts, PTCs generated a contractile force of 739 ± 37 μN, while constructs without cells produced no force (Figure 3.6, D, Table 3.3).

**Table 3.3. Change in length of tissue constructs with and without cells**

| | COC (n = 12) | PTC (n = 12) |
|---|---|---|
| **Length (μm)** | 8000 | 7222.5 ± 37.4 |
| **Contractile force (μN)** | 0 | 738.63 ± 35.6 |

Data are mean ± SEM.

Average viability of PTCs ranged from 93.5 to 97.2% when measured 3-, 7- and 14-days after casting (Figure 3.6, E). To identify ECM structural changes underlying PTC behavior, an SHG analysis of the collagen component was performed. Collagen fibers in PTCs were significantly thicker (1.37 ± 0.01 μm), shorter (13.9 ± 0.06 μm), and less aligned (0.14 ± 0.001 μm) compared to COCs (14.5 ± 0.27 μm, 1.29 ± 0.01 μm, 0.31 ±0.05 μm respectively) (Figure 3.6, F-M, Table 3.4).

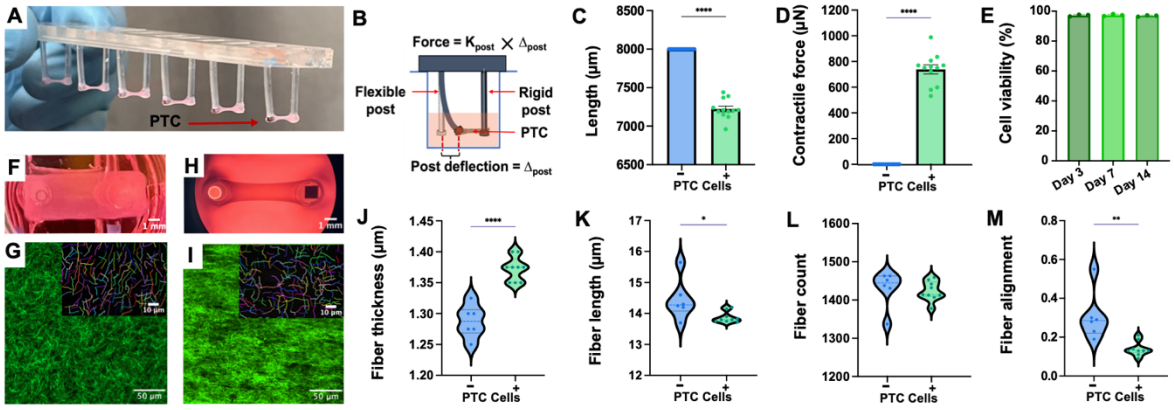


**Figure 3.6. Cell-mediated contraction and ECM remodeling of PTCs.** (**A**) Contraction of PTCs is observed at 3 days after casting. (**B**) Calculation of contractile force. (**C**) Length, (**D**) force, and (**E**) viability of PTCs for (**F**) collagen constructs without cells (- PTC cells) and (**H**) PTC (+ PTC cells). Representative two-photon images of PTC showing fibrillar collagen (green) in (**G**) constructs without cells and (**I**) PTCs. Insets show representative images of collagen fibers detected by Curve Align 5.0 beta in CT–FIRE fiber mode. Analysis of (**J**) fiber thickness, (**K**) length, (**L**) count, and (**M**) alignment in constructs without cells (n = 6) and PTCs (n = 9). For alignment, unity indicates all fibers are aligned in one direction while zero indicates a lack of alignment. Bar graphs and error bars depicted mean ± SEM. Statistical significance using two-tailed unpaired t-test in panels C, D, and J-M or using ANOVA in panel E indicated by *p<0.05, **p<0.01, ***p<0.001, ****p<0.0001.

**Table 3.4. Collagen SHG structural analysis in tissue constructs with and without cells**

| | COC (n = 6) | PTC (n = 9) | P-value |
|---|---|---|---|
| **Fiber Width (μm)** | 1.29 ± 0.01 | 1.37 ± 0.01 | <0.0001**** |
| **Fiber Length (μm)** | 14.5 ± 0.27 | 13.9 ± 0.06 | 0.0253* |
| **Fiber alignment** | 0.307 ± 0.05 | 0.14 ± 0.01 | 0.0023** |
| **Fiber count** | 1431 ± 19.5 | 1423 ± 8.5 | 0.7073 |

Data are mean ± SEM. *p<0.05, **p<0.01, ***p<0.001,****p<0.0001 by unpaired t-test.

### *3.4.2 Tensile loading causes biomechanical creep response*

To assess tissue behavior in response to mechanical stretching, tensile strain on PTCs using a magnetic apparatus was applied (Figure 3.4, A, B). PTCs were magnetically stretched to generate an initial strain of 4-7% by around 408.5 μN of force and held in a stretched position for 4 hours, 24 hours, or 1 week (Figure 3.4, C, Table 3.5). Releasing PTCs from their stretched length (7745 ± 38.5 μm) after 4 hours resulted in partial elastic recovery and mild permanent deformation (7453.33 ± 26.9 μm) as compared to their pre-stretched length (7330 ± 25.2 μm) (Figure 3.7, A). Stretching for 24 hours caused significant permanent deformation (7555 ± 43.7 μm) and little elastic recovery as indicated by the similarity in length of PTCs to their stretched value (7536.67 ± 55.8 μm) (Figure 3.7, B). Similarly, stretching for one week caused

**Table 3.5. PTC length changes before, during and after tensile loading**

| | $L_0$ (μm) | $L_S$ (μm) | $L_T$ (μm) | p-value | | |
|---|---|---|---|---|---|---|
| | | | | **$L_0$ vs. $L_S$** | **$L_0$ vs. $L_T$** | **$L_S$ vs. $L_T$** |
| **T+ 4 hr** | 7330 ± 25.2 | 7745 ± 38.5 | 7453.33 ± 26.9 | <0.0001**** | 0.0003*** | <0.0001**** |
| **T+ 24 hr** | 7133.33 ± 62.9 | 7536.67 ± 55.8 | 7555 ± 43.7 | 0.0001*** | 0.0054** | 0.9080 |
| **T + 1 week** | 6786.67 ± 125 | 7246.67 ± 152 | 7590 ± 113 | 0.0004*** | 0.0196* | 0.2703 |

For each time-point, n=6; from 3 independent experiments. $L_0$ – PTC length before tensile stretching; $L_S$- Stretched PTC length immediately after magnet application ; $L_T$ - Length after unloading PTCs at the end of force application duration. T+4 hr – tensile loading for 4 hours; T+24 hr – tensile loading for 24 hours; T+1 week – tensile loading for 1 week. Data are mean ± SEM. *p<0.05, **p<0.01, ***p<0.001,****p<0.0001 by repeated measure ANOVA with Tukey's multiple comparisons test.

significant permanent

deformation of PTCs (7590 ± 113 μm) such that their length exceeded their initial stretched length (7246.67 ± 152 μm), indicating a creep response in the tissue (Figure 3.7, C). Prior

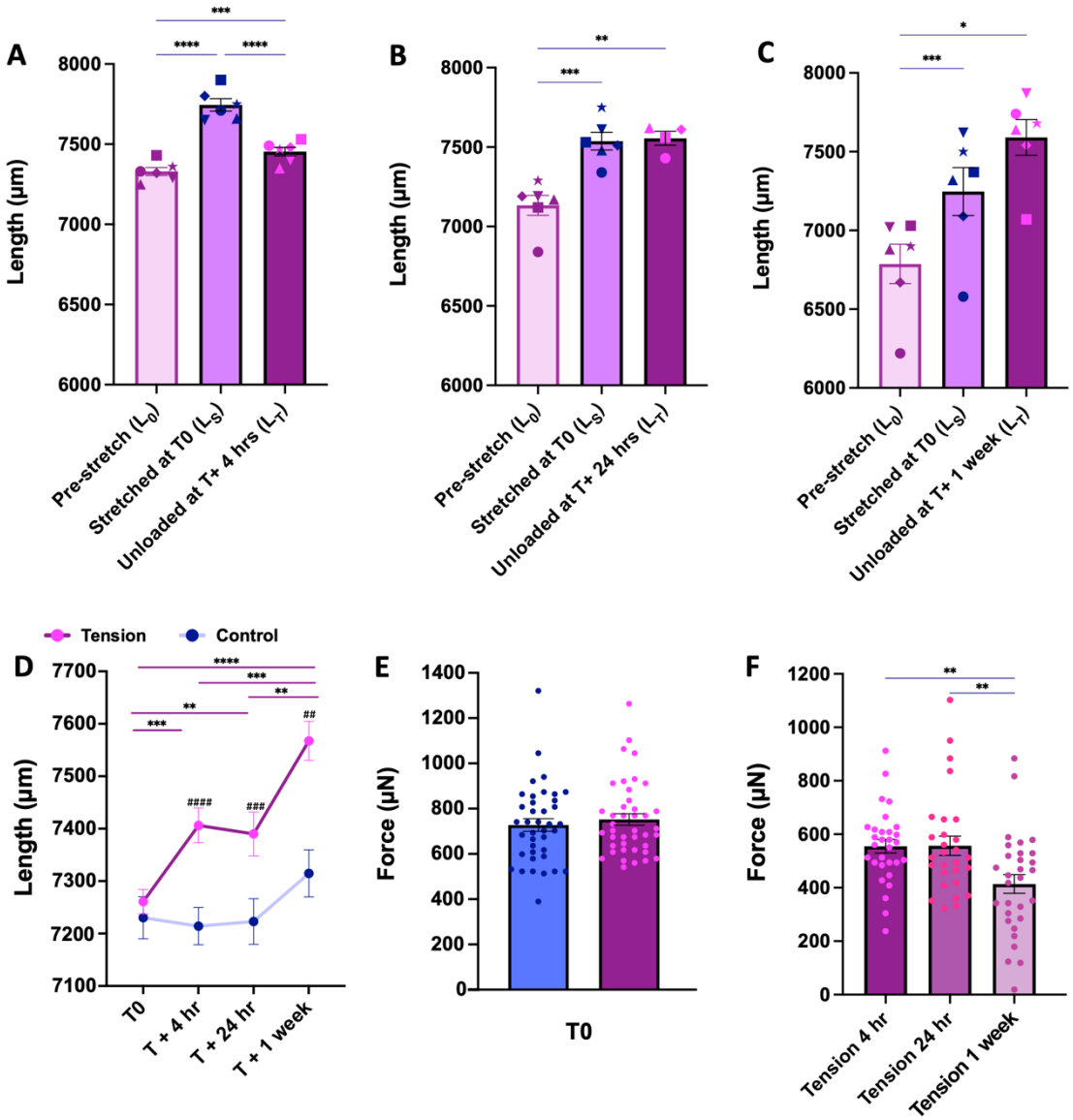


**Figure 3.7. Length changes of PTCs before, during, and after applying tensile stretch** at (**A**) 4 hours (n = 5), (**B**) 24 hours (n = 6) and (**C**) 1 week (n = 6). (**D**) Longitudinal change in PTC length with tensile stretching (For each time-point: control n = 27, tension n = 24). (**E**) PTC contractile force in experimental (n = 41) and control groups (n = 39) before application of tensile stretch. (**F**) PTC contractile force after tensile stretching for 4 hours (n = 30), 24 hours (n = 28), and 1 week (n = 30). Data are mean ± SEM, *p<0.05, ##, **p<0.01, ###, ***p<0.001, ####, ****p<0.0001 by repeated measure 1-way ANOVA (**A-D**) or ordinary 1-way ANOVA (**F**) with Tukey's multiple comparisons or two-tailed unpaired t-test (**D, E**). (**D**) Purple bars with asterisks depict inter-group differences among PTCs subjected to tension; # denotes intra-group difference between stretched and control PTCs at the same time-point.

to tensile stretching, there were no statistically significant differences in PTC length (Figure 3.8, A, Table 3.6) or contractile force (Figure 3.7, E, Table 3.7), between control and experimental

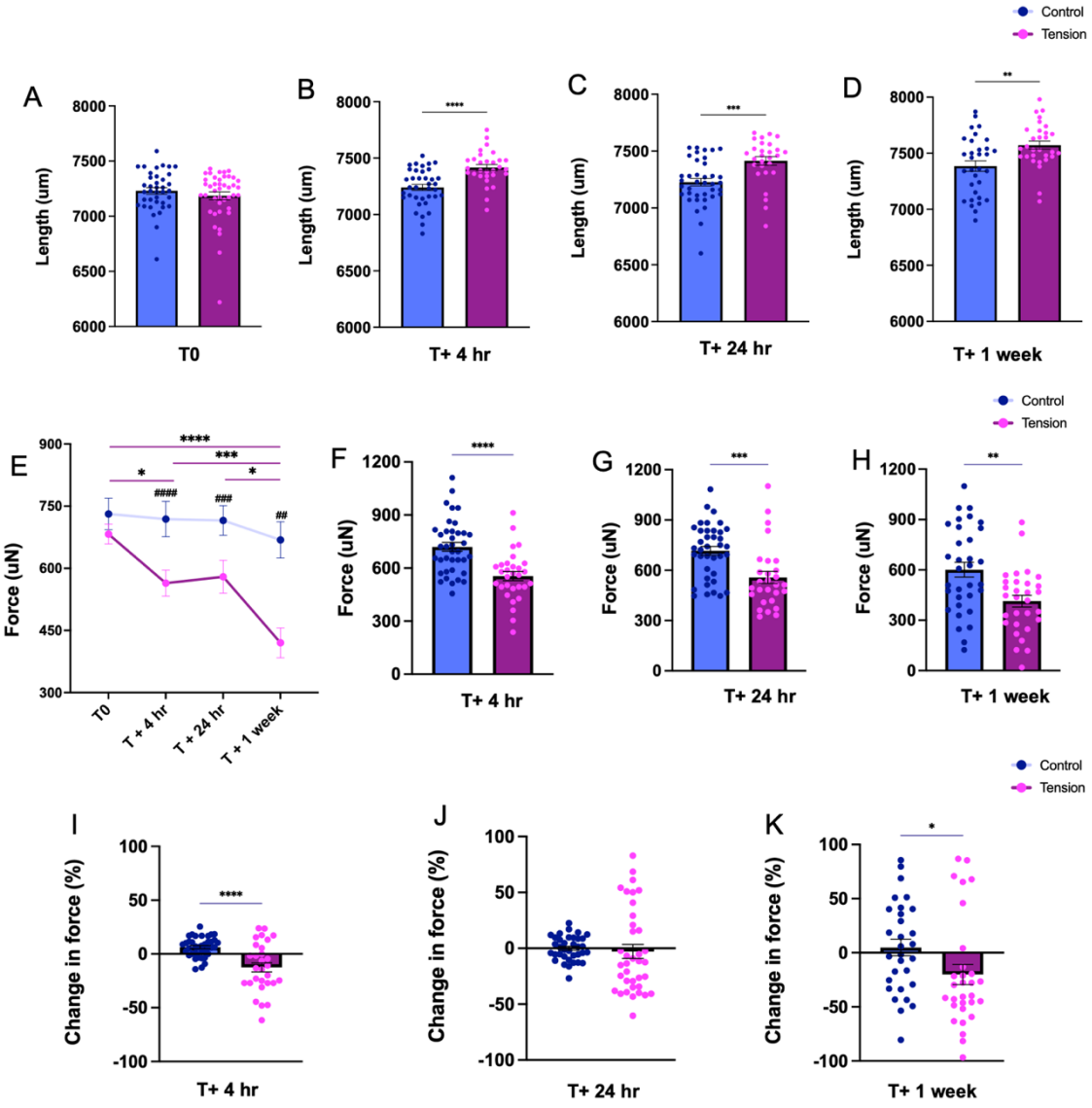


**Figure 3.8. Change in PTC length and force with tensile stretch.** PTC length (**A**) before application of tensile stretch (control $n_c$ = 38; tension $n_t$ = 42), after application of tensile stretch for (**B**) 4 hours ($n_c$ = 37; $n_t$ = 30), (**C**) 24 hours ($n_c$ = 38; $n_t$ = 28), and (**D**) 1 week ($n_c$ = 32; $n_t$ = 30). (**E**) Longitudinal change in PTC contractile force with tensile stretching (for each time-point: $n_c$ = 27, $n_t$ = 24). PTC contractile force after tensile stretching for (**F**) 4 hours ($n_c$ = 38; $n_t$ = 30), (**G**) 24 hours ($n_c$ = 38; $n_t$ = 28), and (**H**) 1 week ($n_c$ = 33; $n_t$ = 30). Percent change in contractile force of PTCs on tensile stretching at (**I**) 4 hours ($n_c$ = 38; $n_t$ = 29), (**J**) 24 hours ($n_c$ = 36; $n_t$ = 37), and (**K**) 1 week ($n_c$ = 30; $n_t$ = 30). Data are mean ± SEM, *p<0.05, ##,**p<0.01, ###,***p<0.001, ####, ****p<0.0001 by repeated measure ANOVA (**E**) with Tukey's multiple comparisons or two-tailed unpaired t-test (**A-K**). (**E**) Purple bars with asterisks depict inter-group differences among PTCs subjected to tension; # denote intra-group difference between stretched and control PTCs at the same time-point.

group PTCs. However, application of tensile stretch significantly increased PTC length (Figure 3.8, B-D, Table 3.6) and reduced contractile force generation compared to controls at all 3 time-points (Figure 3.8, E-K, Table 3.7).

**Table 3.6. PTC length changes on tensile loading at 3 time-points[#]**

| | | n | PTC length (μm) | p-value C vs. T | Length change (%) | p-value C vs. T |
|---|---|---|---|---|---|---|
| **T0** | C | 39 | 7230.53 ± 29.8 | 0.3299 | - | - |
| | T | 41 | 7184.76 ± 35.3 | | - | - |
| **T+4 hr** | C | 38 | 7240.81 ± 26.9 | <0.0001**** | 0.63 ± 0.15 | <0.0001**** |
| | T | 30 | 7415.67 ± 26.9 | | -1.27 ± 0.41 | |
| **T+24 hr** | C | 38 | 7226.58 ± 32.5 | 0.0004*** | 0.08 ± 0.19 | 0.3288 |
| | T | 28 | 7413.57 ± 37.8 | | -0.57 ± 0.72 | |
| **T + 1 week** | C | 33 | 7384.69 ± 46.7 | 0.0026** | -0.04 ± 0.74 | 0.5463 |
| | T | 30 | 7572 ± 36.4 | | -0.97 ± 1.41 | |

[#] Two measurements were made on each PTC - one before tensile loading and one after tensile loading either for 4 hours, 24 hours or 1 week. n – number of PTCs over 3 independent experiments; C – Control; T- Tensile loading; T+4 hr – tensile loading for 4 hours; T+24 hr – tensile loading for 24 hours; T+1 week – tensile loading for 1 week. Data are mean ± SEM. *p<0.05, **p<0.01, ***p<0.001,****p<0.0001 by unpaired t-test.

**Table 3.7. PTC contractile force changes on tensile loading at 3 time-points[#]**

| | | n | Contractile force (μN) | p-value C vs. T | Force change (%) | p-value C vs. T |
|---|---|---|---|---|---|---|
| **T0** | C | 39 | 727.60 ± 27.8 | 0.5175 | - | - |
| | T | 41 | 752.12 ± 25.6 | | - | - |
| **T+4hr** | C | 38 | 719.75 ± 24.9 | <0.0001**** | 6.36 ± 1.48 | <0.0001**** |
| | T | 30 | 555.12 ± 25.6 | | -12.4 ± 4.25 | |
| **T+24hr** | C | 38 | 715.75± 26.5 | 0.0006*** | -0.05 ± 1.82 | 0.6682 |
| | T | 28 | 557.11 ± 35.9 | | 2.88 ± 6.23 | |
| **T + 1 week** | C | 33 | 600.77 ± 44.4 | 0.0018** | 4.8 ± 7.65 | 0.0425* |
| | T | 30 | 413.94 ± 35 | | -20.1 ± 9.27 | |

[#] Two measurements were made on each PTC - one before tensile loading and one after tensile loading either for 4 hours, 24 hours or 1 week. n – number of PTCs over 3 independent experiments; C – Control; T- Tensile loading; T+4 hr – tensile loading for 4 hours; T+24 hr – tensile loading for 24 hours; T+1 week – tensile loading for 1 week. Data are mean ± SEM. *p<0.05, **p<0.01, ***p<0.001,****p<0.0001 by unpaired t-test.

Overall, the creep response in PTCs results in significant elongation at one week with tensile loading as compared to 4 and 24 hours (Figure 3.7, D, Table 3.8, **Error! Reference source not found.**). Consequently, the same PTCs stretched for one week generated weaker contractile forces (420.05 ± 35.99 μN) as compared to being stretched for 4 (564.06 ± 31.30 μN ) or 24 hours (579.50 ± 39.74 μN) (Figure 3.8, E, Table 3.9Table 3.8). These results indicate that tensile loading of PTCs results in a time dependent increase in length and reduction of contractile forces

**Table 3.9. Longitudinal PTC length and contractile force measurements on tensile loading at 3 time-points***

| | | n | PTC length (μm) | Contractile force (μN) |
|---|---|---|---|---|
| **T0** | C | 27 | 7230.37 ± 40.15 | 731.15 ± 38.15 |
| | T | 24 | 7260.83 ± 23.40 | 682.46 ± 23.89 |
| **T+4 hr** | C | 27 | 7214.23 ± 35.41 | 718.83 ± 42.57 |
| | T | 24 | 7406.25 ± 32.95 | 564.06 ± 31.30 |
| **T+24 hr** | C | 26 | 7222.96 ± 43.49 | 715.42 ± 35.84 |
| | T | 24 | 7390.00 ± 41.83 | 579.50 ± 39.74 |
| **T + 1 week** | C | 27 | 7314.81 ± 44.86 | 668.47 ± 43.69 |
| | T | 24 | 7567.50 ± 37.19 | 420.05 ± 35.99 |

* Four measurements were made on each PTC - one before tensile loading and three after tensile loading for measuring lengths in a longitudinal manner at 4 hours, 24 hours and 1 week. n – number of PTCs over 3 independent experiments; C – Control; T- Tensile loading; T+4 hr – tensile loading for 4 hours; T+24 hr – tensile loading for 24 hours; T+1 week – tensile loading for 1 week. Data are mean ± SEM.

**Table 3.8. P-values for longitudinal PTC length and contractile force measurements on tensile loading at 3 time-points***

as compared to controls.

* Four measurements were made on each PTC - one before tensile loading and three after tensile loading for measuring lengths in a longitudinal manner at 4 hours, 24 hours and 1 week. n – number of PTCs over 3 independent experiments; T- Tensile loading; T+4 hr – tensile loading for 4 hours; T+24 hr – tensile loading for 24 hours; T+1 week – tensile loading for 1 week. P-values are for comparison of PTC length and contractile forces values shown in Table 3.6 using repeated measures ANOVA and Tukey's multiple comparisons test. *p<0.05, **p<0.01, ***p<0.001,****p<0.0001.

### *3.4.3 Tensile loading triggers changes in cell structure and number*

To assess the effects of tensile stretching on the biological response of PDL cells, immunofluorescent staining was performed (Figure 3.9). Confocal images of around 9-12 PTCs per group from 3 independent experiments were obtained. Each of the confocal microscope images was used to quantify cell number, F-actin levels, aSMA levels, and directionality. F-actin and aSMA levels were normalized using either cell count or area. No significant differences were noted for PTCs stretched for 4 or 24 hrs in any of the parameters except directionality which was higher in PTCs tensile stretched for 4 hours compared to controls. However, cell count (Figure 3.9, D, Table 3.10 and Table **3.11**), F-actin levels (Figure 3.9, E), and aSMA expression (Figure 3.9, F) were all higher for PDL cells in PTCs after one week of tensile loading as compared to unloaded controls (Figure 3.10, Table 3.12). PTCs stretched for 1 week had 117.95 ± 3.36 AU of

| | | T + 4 hr (C) | T + 4 hr (T) | p-Value |
|---|---|---|---|---|
| **n** | | 31 | 29 | |
| **Cell count per image** | | 437.32 ± 35.5 | 457.76 ± 34.4 | 0.6814 |
| **F-actin** | **per nucleus (AU)** | 26.4 ± 0.88 | 26 ± 0.93 | 0.7448 |
| | **per unit area (AU)** | 115.23 ± 10.3 | 114.14 ± 8.37 | 0.9349 |
| **aSMA** | **per nucleus (AU)** | 19.4 ± 0.99 | 20.9 ± 0.97 | 0.2651 |
| | **per unit area (AU)** | 113.32 ± 6.41 | 124.88 ± 8.09 | 0.2687 |
| **Directionality** | | 0.0285 ± 0.000472 | 0.0302 ± 0.000551 | 0.0273* |

| | Adjusted p -Values | |
|---|---|---|
| | **PTC Length** | **Contractile force** |
| **T0 (T) vs. T + 4 hr (T)** | 0.0001*** | 0.0153* |
| **T0 (T) vs. T + 24 hr (T)** | 0.0092** | 0.1238 |
| **T0 (T) vs. T + 1 week (T)** | <0.0001**** | <0.0001**** |
| **T + 4 hr (T) vs. T + 24 hr (T)** | 0.9478 | 0.9478 |
| **T + 4 hr (T) vs. T + 1 week (T)** | 0.0004*** | 0.0007*** |
| **T + 24 hr (T) vs. T + 1 week (T)** | 0.0081** | 0.0107* |

**Table 3.10. Immnofluorescence analysis of PTCs tensile loaded for 4 hours**

F-actin and 127.69 ± 4.95 AU of SMA whereas F-actin in controls was 96.03 ± 4.79 AU and aSMA

Data are mean ± SEM. n – number of confocal microscope images obtained from 9-12 PTCs per group from 3 independent experiments. *p<0.05 by unpaired t-test.

was 107.17 ± 4.42 AU. However, F-actin and aSMA production was similar on a per-cell basis for PTCs tensile loaded for 1 week compared to controls (Figure 3.11, Table 3.12). These results indicate that elevated F-actin and aSMA levels observed at one week of tensile loading is mainly due to an increase in cell count, presumably due to proliferation induced by mechanical loading.

**Table 3.12. Immnofluorescence analysis of PTCs tensile loaded for 24 hours**

Inter-group comparisons showed a statistically significant trend of cell count reducing with time in unloaded control PTCs. Control PTCs at 4 hours had significantly higher cell numbers than in the 24 hours and 1 week groups (Figure 3.9, D). In the 24 hours group, F-actin levels per cell / nucleus

Data are mean ± SEM. n – number of confocal microscope images obtained from 9-12 PTCs per group from 3 independent experiments.

**Table 3.11. Immnofluorescence analysis of PTCs tensile loaded for 1 week**

| | | T + 24 hr (C) | T + 24 hr (T) | p-Value |
|---|---|---|---|---|
| **n** | | 31 | 33 | |
| **Cell count per image** | | 351.97 ± 18.3 | 373.27 ± 27.1 | 0.5216 |
| **F-actin** | **per nucleus (AU)** | 21.4 ± 0.91 | 20.9 ± 0.88 | 0.7193 |
| | **per unit area (AU)** | 74.56 ± 4.78 | 78.28 ± 7.12 | 0.6699 |
| **aSMA** | **per nucleus (AU)** | 23 ± 1.28 | 23.3 ± 1.19 | 0.8648 |
| | **per unit area (AU)** | 130.46 ± 7.89 | 138.31 ± 6.45 | 0.4415 |
| **Directionality** | | 0.0301 ± 0.000564 | 0.0304 ± 0.000515 | 0.5049 |
| | | **T + 1 week (C)** | **T + 1 week (T)** | **p-Value** |
| **n** | | 31 | 36 | |
| **Cell count per image** | | 351.74 ± 11.1 | 447.02 ± 13.8 | <0.0001**** |
| **F-actin** | **per nucleus (AU)** | 27.3 ± 0.94 | 26.6 ± 0.42 | 0.4712 |
| | **per unit area (AU)** | 96.03 ± 4.79 | 117.95 ± 3.36 | 0.0003*** |
| **aSMA** | **per nucleus (AU)** | 19.8 ± 0.76 | 18.3 ± 0.51 | 0.1009 |
| | **per unit area (AU)** | 107.17 ± 4.42 | 127.69 ± 4.95 | 0.0034** |
| **Directionality** | | 0.0361 ± 0.000941 | 0.0394 ± 0.00102 | 0.0204* |

Data are mean ± SEM. n – number of confocal microscope images obtained from 9-12 PTCs per group from 3 independent experiments. *p < 0.05, **p<0.01, ***p<0.001,****p<0.0001 by unpaired t-test.

were significantly lower in both control and tensile loaded PTCs than those respective PTCs in 4 hour and 1 week groups (Figure 3.11, B). On the contrary, aSMA levels per cell / nucleus in the 24 hour tensile stretched PTCs were significantly higher compared to the one week tensile stretched group (Figure 3.11, C). Cells in the PTCs became progressively more aligned with time, as seen by the directionality measure (Figure 3.9, G and Figure **3.12**). Unloaded control PTCs at 1 week had a significantly greater directionality score, indicating greater alignment, compared to unloaded controls at both 4 and 24 hours. Similarly, PTCs tensile loaded for 1 week were significantly more aligned compared to those tensile loaded for both 4 and 24 hours. To summarize, tensile loading effects were observable in cell count and directionality parameters for the shorter 4 hour and 24 hour time-points, whereas after 1 week of tensile loading, all four

parameters were significantly elevated. Together, these results indicate there is a mechanobiological response in PDL cells due to tensile mechanical loading.

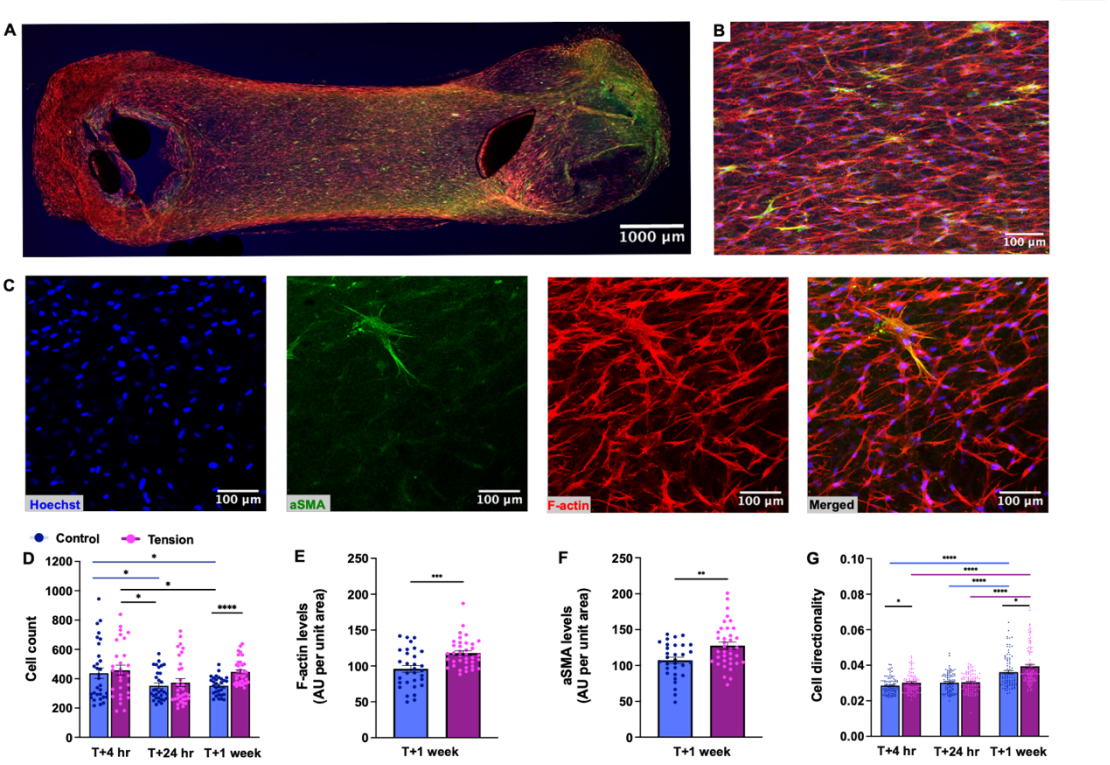


**Figure 3.9. PTC structural analysis and tensile loading effects.** (**A-C**) Representative images of immunofluorescent stained PTCs three days after casting for nuclei (blue), aSMA (green) and F-actin (red). (**A**) Whole mounted representative composite image of a PTC. Networked appearance of stellate and spindle shaped PDL cells interspersed with aSMA positive green myofibroblast cells (**B, C**). Quantification of immunofluorescent data on tensile stretching for 4 hours, 24 hours and 1 week for (**D**) cell count and (**G**) cell directionality. Quantification of F-actin (**E**) and aSMA (**F**) levels normalized by area after tensile stretching for one week. Data are mean ± SEM, *p<0.05, **p<0.01, ***p<0.001, ****p<0.0001 by 1-way ANOVA with Tukey's multiple comparisons (**D, G**) or two-tailed unpaired t-test (**D-G**). (n = 9-12 PTCs per group from 3 independent experiments. 30-50 images per group were taken for analysis).

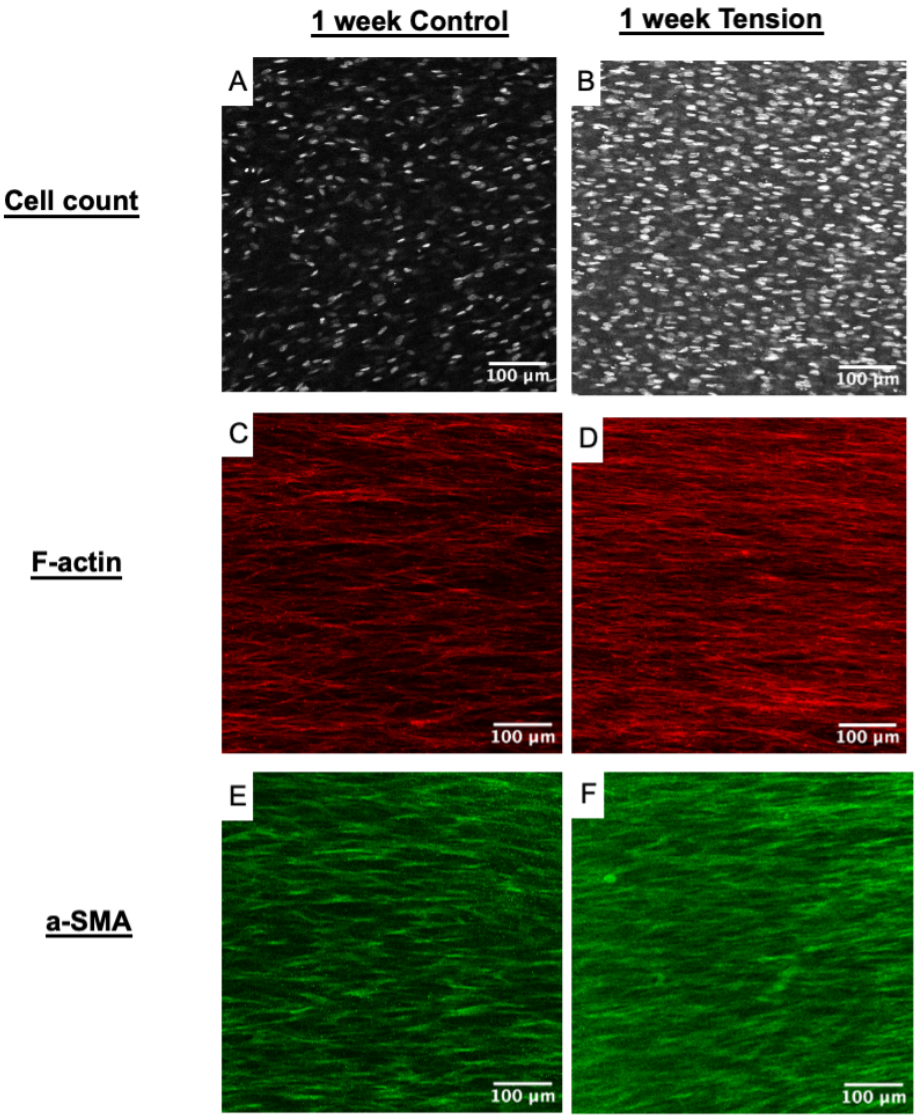


**Figure 3.10.** Differences in cell count, F-actin and aSMA with tension. Representative immunofluorescent images depicting (**A**) decrease in nuclei count in one week control, and (**B**) increase in nuclei count with application of tension in the one week PTC compared to its control. Similarly, representative images of (**C, D**) F-actin and (**E, F**) aSMA staining of PTCs show greater intensity of both stains in the one week tensile loaded group (**D, F**) as compared to the controls (**C, E**).

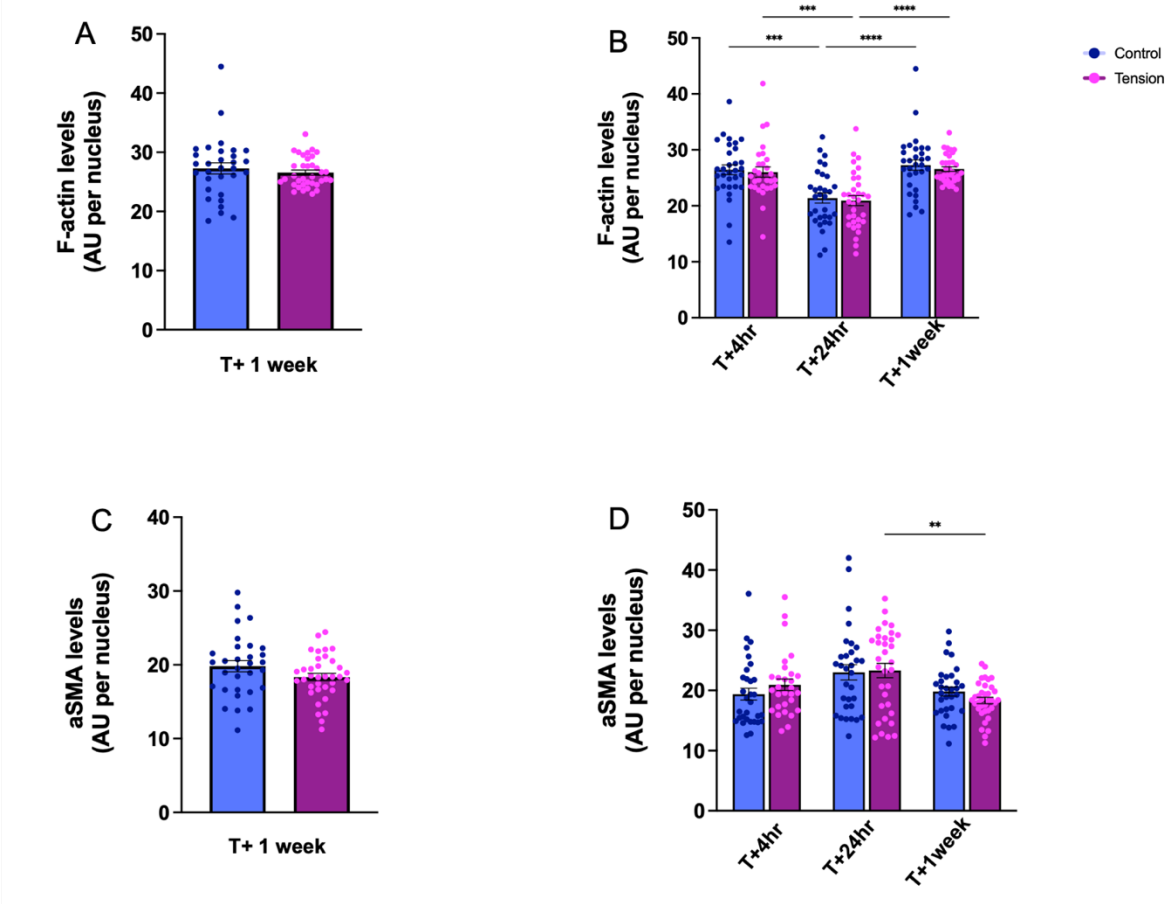


**Figure 3.11. Quantification of immunofluorescent data of (A, B) F-actin and (C, D) aSMA levels normalized by number of cells after tensile stretching for 4 hours, 24 hours, or 1 week.** Data are mean ± SEM, *p<0.05, **p<0.01, ***p<0.001, ****p<0.0001 by two-tailed unpaired t-test (**A, C**) or one-way ANOVA with Tukey's multiple comparisons (**B, D**). (n = 9-12 PTCs per group from 3 independent experiments. 30-50 images per group were taken for analysis).

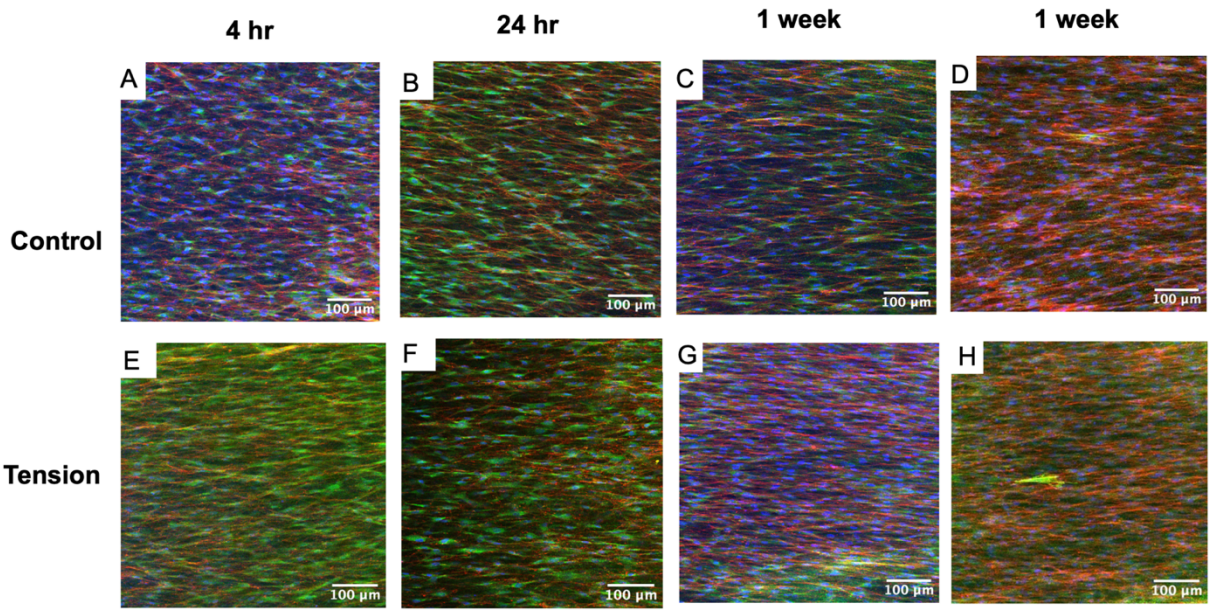


**Figure 3.12. Tissue alignment with time and tension.** Representative images of immunofluorescent stained PTCs for nuclei (blue), aSMA (green) and F-actin (red). All images are depicted with the tensile axis oriented along the left to right direction. Tissue alignment was calculated using the Directionality plugin in FIJI image analysis software. Representative immunofluorescent images depicting increased alignment of cellular elements progressively from 4 hours (**A, E**) to 24 hours (**B, F**) to one week (**C, D, G, H**). At each time-point, tensile-stretched PTCs (**E-H**) appear more aligned compared to unstretched controls (**A-D**). Large myofibroblasts (aSMA-positive) are observed in PTCs at one week, for both control and tensile stretched groups (**D, H**).

### *3.4.4 PDL cells remodel collagen upon tensile loading*

To identify ECM structural changes underlying PTC behavior on tensile loading, an SHG analysis of collagen fibers was carried out. By one week, tensile stretching significantly decreased fiber thickness, increased fiber length, reduced fiber count, and increased fiber alignment as compared to stretching for either 4 or 24 hours (Figure 3.13Figure 3.14). Tensile loading for 4 hours significantly increased fiber thickness (1.4 ± 0.01 μm) and reduced fiber length (14.3 ± 0.10 μm) compared to controls (1.38 ± 0.01 μm and 14.8 ± 0.13 μm respectively) (Figure 3.13, A, B, Table 3.13). On the other hand, loading for 24 hours significantly increased fiber thickness (1.39 ± 0.01

μm) alone compared to unloaded controls (1.37 ± 0.01 μm) (Figure 3.13, A, Table 3.14). After loading for one week, PTCs had significantly longer fibers (15.5 ± 0.10 μm), lower fiber count (1325 ± 9.88) and higher fiber alignment (0.5 ± 0.01) compared to the controls and stretching for either 4 or 24 hrs (Figure 3.13, Table 3.15).

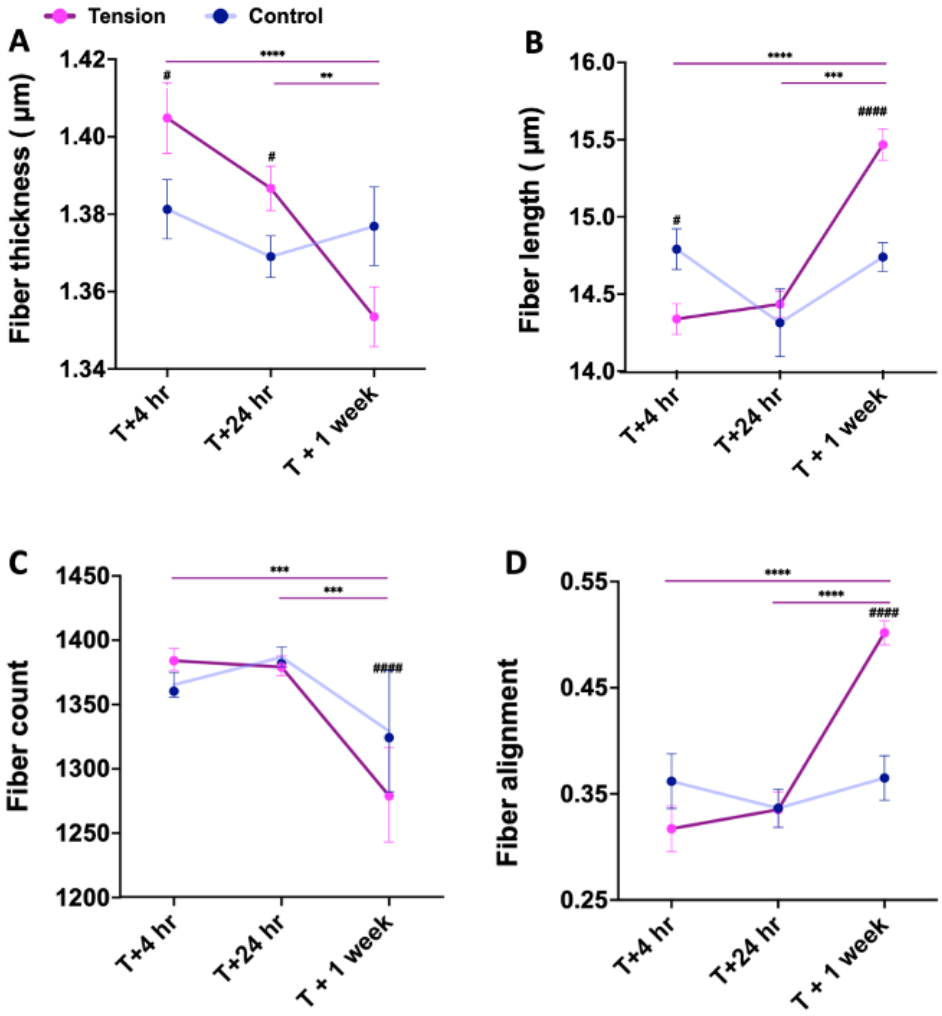


**Figure 3.13. Quantification of collagen fiber thickness** (**A**), length (**B**), count (**C**) and alignment (**D**) on tensile stretching PTCs for 4 hours, 24 hours and 1 week, using Curve Align 5.0 beta in CT–FIRE fiber mode. Data are mean ± SEM, #, *p<0.05, **p<0.01, ***p<0.001, ####, ****p<0.0001 by 1-way ANOVA with Tukey's multiple comparisons (**A-D**) or two-tailed unpaired t-test (**A-D**). (**A-D**) Purple bars with asterisks depict inter-group differences among PTCs subjected to tension, # denotes intra-group difference between stretched and control PTCs at the same time-point. (n = 9-12 PTCs per group from 3 independent experiments. 30-50 images per group were taken for analysis).

**Table 3.13. Structural analysis of collagen in PTCs tensile loaded for 4 hrs**

| | T + 4 hr (C) | T + 4 hr (T) | p-Value |
|---|---|---|---|
| **n** | 48 | 40 | |
| **Fiber thickness (μm)** | 1.38 ± 0.01 | 1.4 ± 0.01 | 0.0496* |
| **Fiber length (μm)** | 14.8 ± 0.13 | 14.3 ± 0.10 | 0.0102* |
| **Fiber alignment** | 0.36 ± 0.03 | 0.32 ± 0.02 | 0.1927 |
| **Fiber count** | 1360 ± 9.63 | 1379 ± 8.62 | 0.1553 |

Data are mean ± SEM. n – number of 2-photon microscope images obtained from 9-12 PTCs per group from 3 independent experiments. *p < 0.05 by unpaired t-test.

**Table 3.14. Structural analysis of collagen in PTCs tensile loaded for 24 hrs**

| | T + 24 hr (C) | T + 24 hr (T) | p-Value |
|---|---|---|---|
| **n** | 67 | 68 | |
| **Fiber thickness (μm)** | 1.37 ± 0.01 | 1.39 ± 0.01 | 0.0269* |
| **Fiber length (μm)** | 14.3 ± 0.22 | 14.4 ± 0.08 | 0.6046 |
| **Fiber alignment** | 0.34 ± 0.02 | 0.34 ± 0.02 | 0.9596 |
| **Fiber count** | 1382 ± 7.77 | 1374 ± 7.72 | 0.4853 |

Data are mean ± SEM. n – number of 2-photon microscope images obtained from 9-12 PTCs per group from 3 independent experiments. *p < 0.05 by unpaired t-test.

**Table 3.15. Structural analysis of collagen in PTCs tensile loaded for 1 week**

| | T + 1 week (C) | T + 1 week (T) | p-Value |
|---|---|---|---|
| **n** | 40 | 50 | |
| **Fiber thickness (μm)** | 1.38 ± 0.01 | 1.35 ± 0.01 | 0.0664 |
| **Fiber length (μm)** | 14.7 ± 0.09 | 15.5 ± 0.10 | <0.0001**** |
| **Fiber alignment** | 0.37 ± 0.02 | 0.50 ± 0.01 | <0.0001**** |
| **Fiber count** | 1390 ± 10.1 | 1325 ± 9.88 | <0.0001**** |

Data are mean ± SEM. n – number of 2-photon microscope images obtained from 9-12 PTCs per group from 3 independent experiments. *p < 0.05, **p<0.01, ***p<0.001,****p<0.0001 by unpaired t-test.

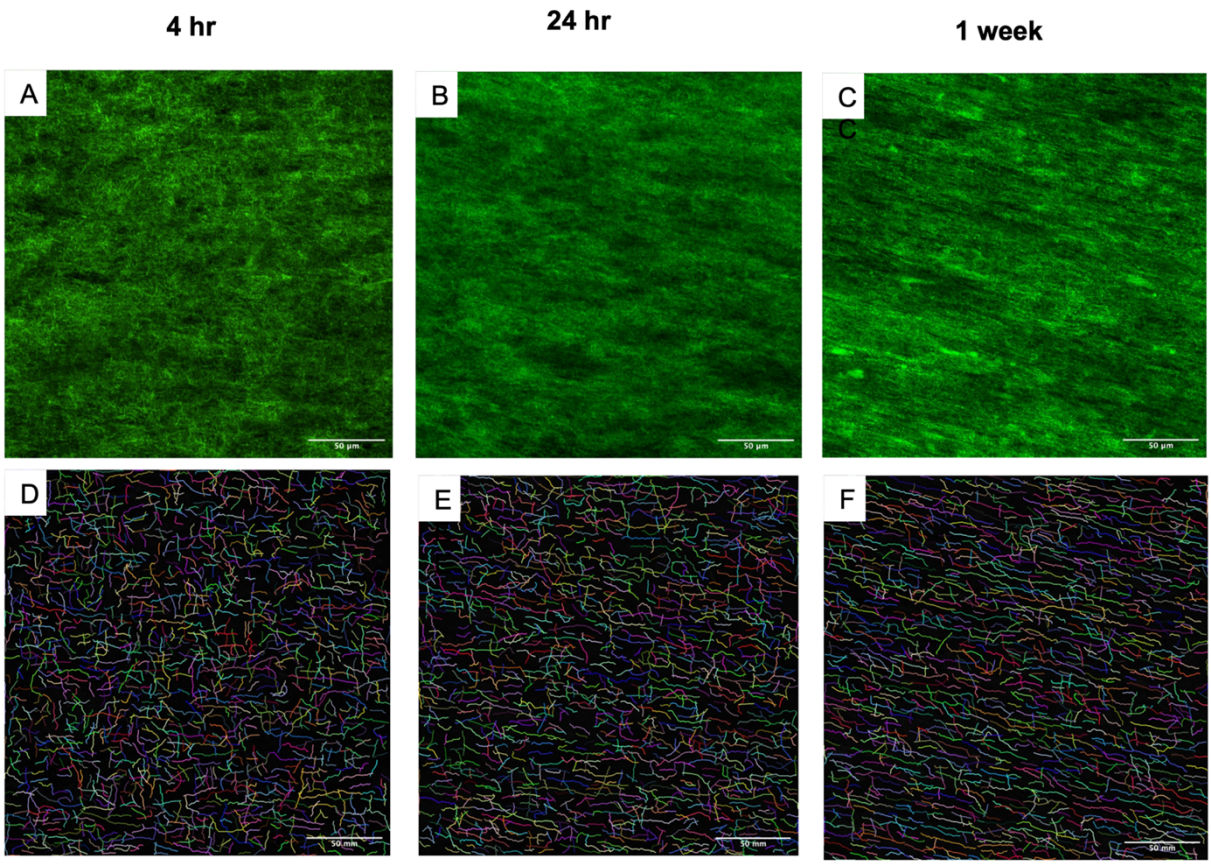


**Figure 3.14. Collagen fiber alignment with tensile loading over time.** All images are depicted with the tensile axis oriented along the left to right direction. Representative images of second harmonics generation analysis of collagen fibers (green) imaged using two-photon microscopy of PTCs subjected to tensile loading (**A-C**). Output images generated by CurveAlign CT-Fire mode with collagen fibers detected by the software (**D-E**) for images A-C respectively.

### *3.4.5 Tensile stretch regulates gene pathways for tissue remodeling*

To identify early transcriptional changes from tensile loading, we performed bulk RNA-sequencing of PTCs stretched for 4 and 24 hours. Tensile loading resulted in a higher number of differentially expressed genes (DEGs) over time (Figure 3.15, A). A total of 89 genes were differentially expressed 4 hours after tension application of which 77 were upregulated and 12 downregulated. The 24 hour tension group had 146 downregulated and 334 upregulated genes compared to the 4 hour tension group. KEGG pathway analysis indicated that signal transduction pathways had the most DEGs after 4 and 24 hours of tensile loading (Figure 3.15, B). At 24 hours, DEGs for cell

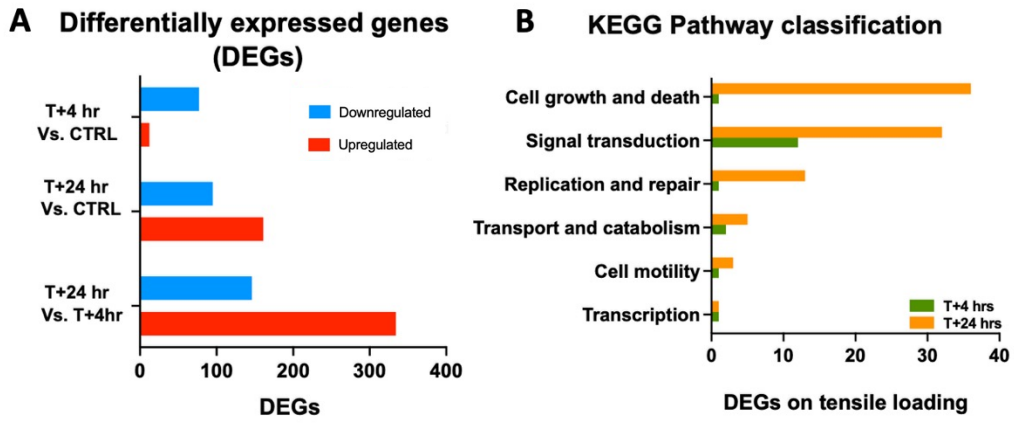


**Figure 3.15. Gene expression analysis at 4 hours and 24 hours after tensile stretching (For each time-point, n = 1).** (**A**) Bar chart demonstrates split-up of upregulated and downregulated genes among genes differentially expressed at 4 hours and 24 hours, compared to control and to each other. (**B**) KEGG pathway analysis depicting biological pathways DEGs belong to, at 4 hours and 24 hours compared to controls. T+4hr, T+24 hr - tensile loading for 4 hours and 24 hours respectively; CTRL – Control.

growth and death, and replication and repair pathways were among the highest. Downregulation at 4 hours and upregulation at 24 hours was observed for genes related to cytoskeletal organization and the Rho/ROCK pathway (ACTN1, FLNA, RHOA, ARPC3, LIMK1) (Figure 3.16, A), and aSMA production and TGF-β pathway (ACTA2, BMP8A, SMAD7, TGFB1) (Figure 3.16, B).

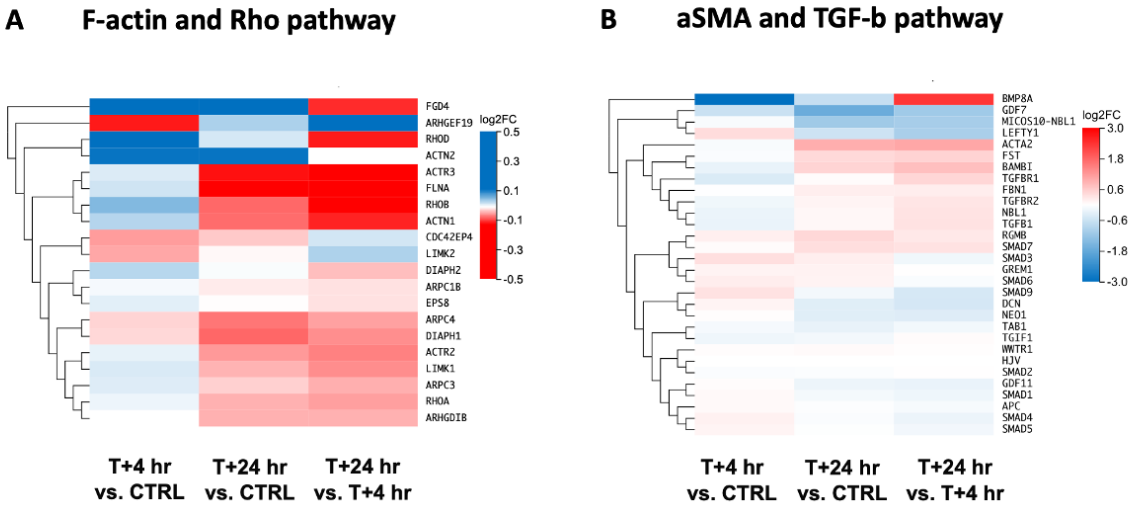


**Figure 3.16. Gene expression analysis at 4 hours and 24 hours after tensile stretching (For each time-point, n = 1).** Heat maps showing log2 fold change in subsets of DEGs related to (**A**) F-actin and Rho pathway, and (**B**) aSMA and TGF-b pathway. T+4hr, T+24 hr - tensile loading for 4 hours and 24 hours respectively; CTRL – Control.

Similarly, genes related to cell cycle and cell death (CDK1, CDCA2, CCNB1, CENPF) (Figure 3.17, A), collagen fibrillogenesis and ECM organization (COL1A1, PLOD1, PLOD2, COMP), collagen breakdown and tissue turnover (ADAMTS3, MMP1, MMP3, MMP8, TIMP3) (Figure 3.17, B), and osteoblast differentiation and mineralized matrix production (BMP8B, IBSP, SPP1, DMP1) (Figure 3.17, C) were downregulated at 4 hours and upregulated at 24 hours.

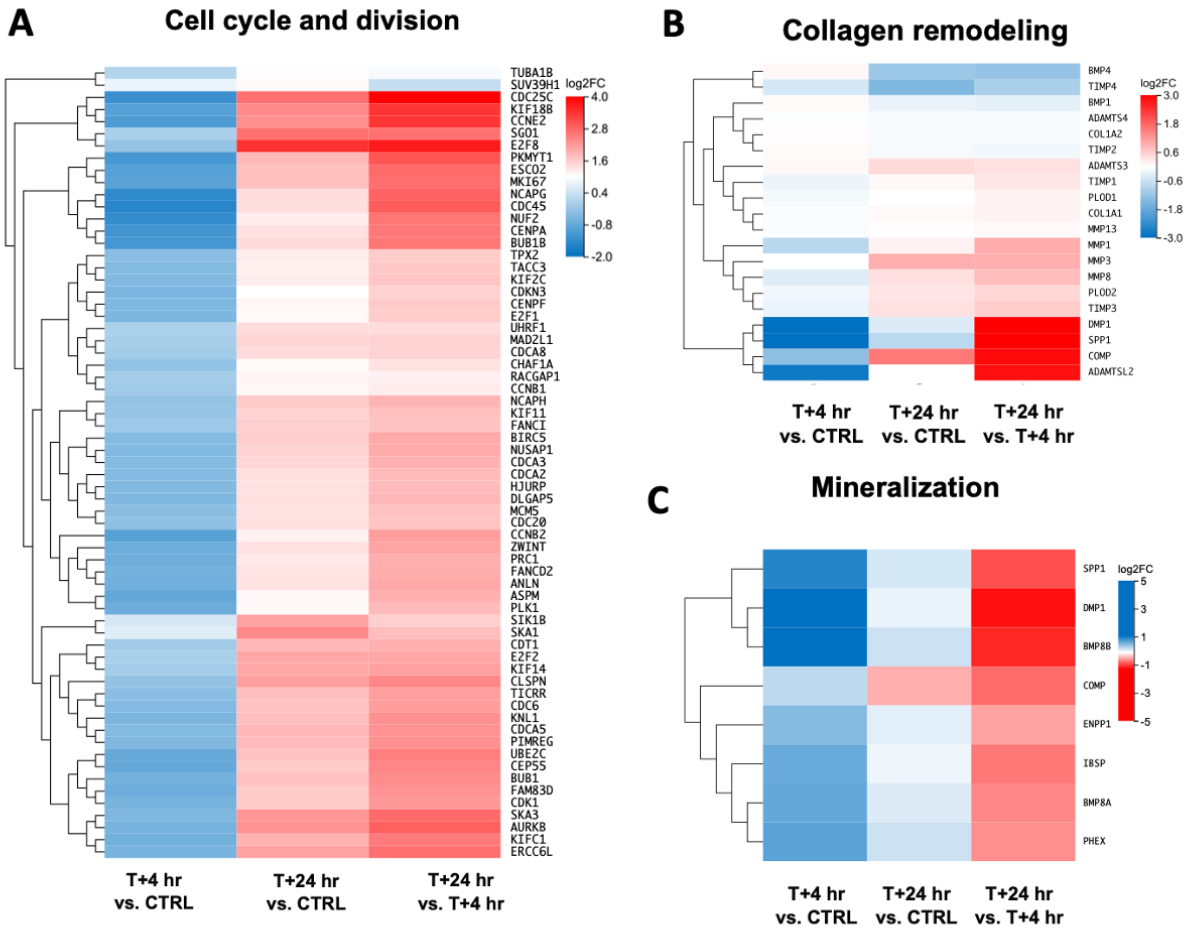


**Figure 3.17. Gene expression analysis at 4 hours and 24 hours after tensile stretching (For each time-point, n = 1).** (Heat maps showing log2 fold change in subsets of DEGs related to (**A**) cell cycle and division, (**B**) collagen remodeling, and (**H**) mineralization. T+4hr, T+24 hr - tensile loading for 4 hours and 24 hours respectively; CTRL – Control.

Gene ontology (GO) analysis showed a significant upregulation of genes related to actin filament bundle organization and negative regulators of bone mineralization after stretching for 4 hours (Figure 3.18, A). Genes related to ossification, cytokine production, ECM organization and mineralization were downregulated at 4 hours (Figure 3.19, A).

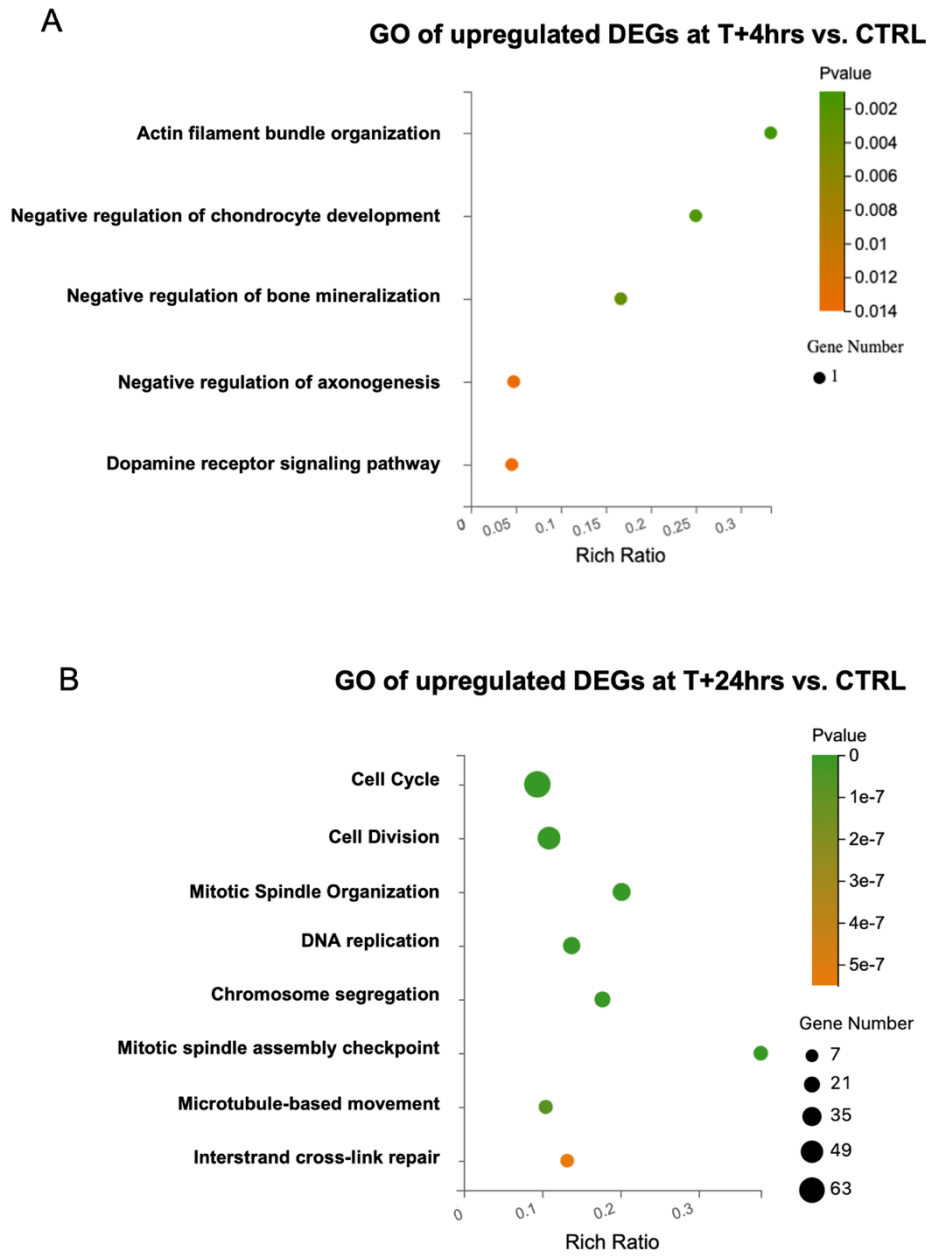


**Figure 3.18.** Significant gene ontology biological processes (GO:BP) enriched in upregulated DEGs at (**A**) 4 hours of tensile stretching compared to control and (**B**) 24 hours of tensile stretching compared to control

In PTCs stretched for 24 hours, GO analysis showed upregulation of genes mainly belonging to the cell cycle, cell division, and DNA replication pathways (Figure 3.18, B) and downregulation of cell differentiation, cytokine mediated, PI3 kinase pathways and negative regulators of apoptosis (Figure 3.19, B).

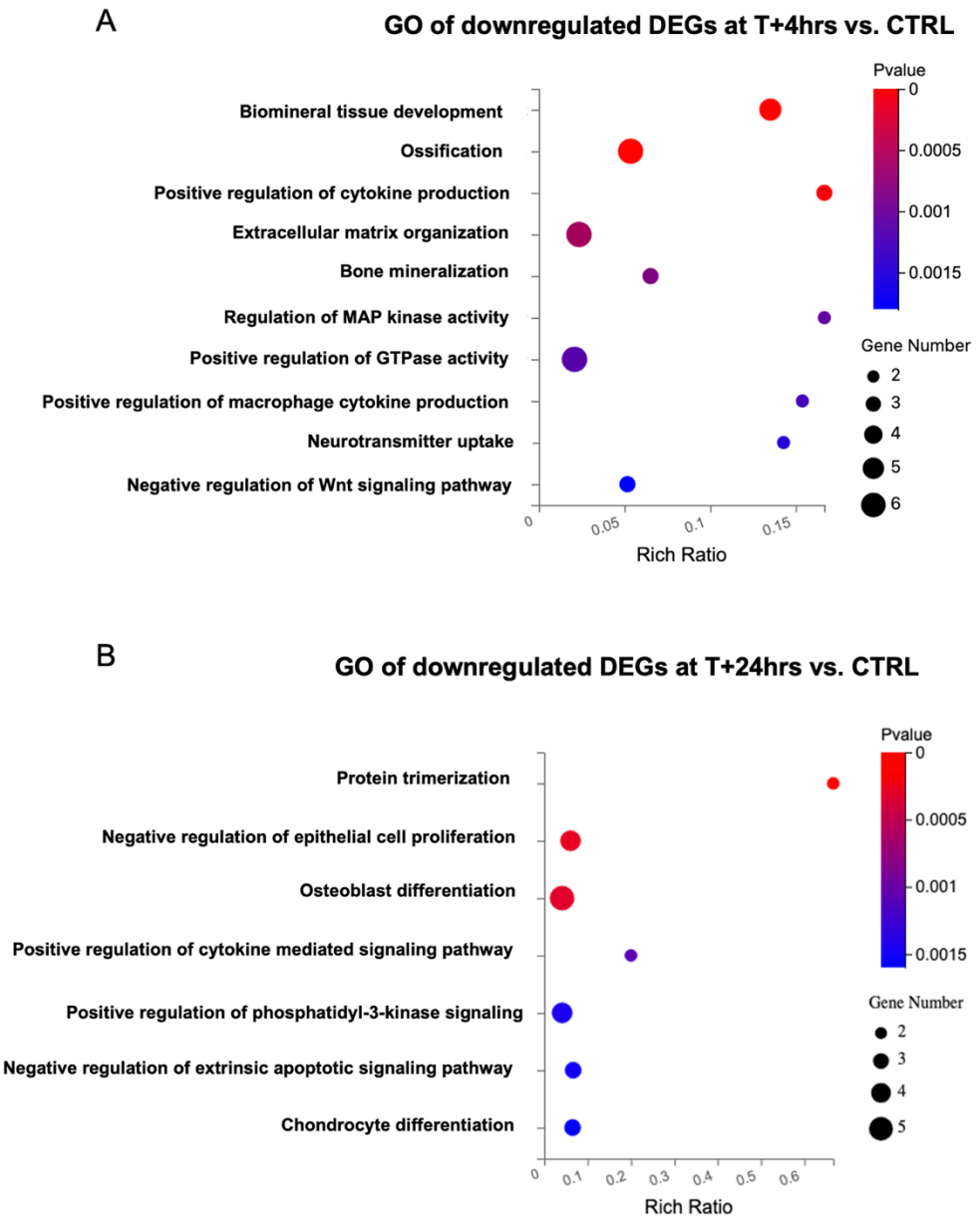


**Figure 3.19.** Significant gene ontology biological processes (GO:BP) enriched in downregulated DEGs at (**A**) 4 hours of tensile stretching compared to control and (**B**) 24 hours of tensile stretching compared to control

## 3.5 DISCUSSION

This chapter provides the proof-of-principle for fabricating a novel *in vitro* 3D PDL model which has several advantages over existing 3D PDL models of which there are few. Using in-house mechanical fabrication and 3D printing tissue-engineering tools, I fabricated the PTC model based on the engineered heart tissue platform pioneered in our lab (Bielawski et al. 2016, Bremner et al. 2022). Scaffold based *in vitro* models have a problematic non-uniform distribution of nutrients which affects cell distribution and proliferation. Scaffold-free models cast as thick collagen gels, also have cells diffusing towards the surface from the core due to lack of nutrition (Yang et al. 2015). In contrast, our PTCs are less than 500 microns thick, hence cells stay sufficiently perfused and uniformly distributed even over a 4-week period. Our model design of attaching PTCs at both ends to posts, leaving the bulk of tissue open and accessible, is highly conducive for live imaging and longitudinal measurements. Importantly, it also facilitates spatial and temporal monitoring of cellular responses which may be involved in the region-specific periodontal cell differentiation necessary to preserve the complex periodontal anatomy. This is a significant difficulty in scaffold based designs where cells are inaccessible and obliterated from view within scaffold matrices (Liao et al. 2016).

3D *in vitro* models that recapitulate the spatial context for cell-cell and cell-matrix interactions as *in vivo* are better suited to investigate cellular and molecular mechanisms that determine tissue-level PDL properties and behavior. Our bioengineered PTCs emulate certain key *in vivo* architecture, structure and function features as follows -

Architecture: PDL cells in our model self-assembled into PTCs within the collagenous ECM while being suspended between the two silicone posts (Figure 3.5). This recreates the *in vivo* design feature of principal collagen fiber bundles, enmeshed with PDL cells, spanning alveolar bone and cemental surfaces within the PDL. We have also demonstrated how spindle shaped and stellate

cells along with collagen fibers are organized parallel to each other and aligned along the tensile axis in our model (Figure 3.9, A, and Figure **3.12**). This bears a striking resemblance to observations in *in vivo* PDL in studies by Beertsen et al. 1997 and Hirashima et al. 2016. On a cellular scale, our model embodies the physiologic cell-cell and cell-ECM interactions which are the primary conduits for crosstalk (Figure 3.9, B, C). Embedding cells in type I collagen to fabricate PTCs renders our model physiologically relevant as type I collagen is the predominant component of *in vivo* PDL ECM. This feature is further bolstered as collagen fiber diameters in our PTCs ranging from 1.35 to 1.4 μm fall within the 1 - 4 μm diameter range of *in vivo* PDL collagen fiber bundles (Berkovitz 1990; Pini et al. 2004). Thus, our model mimics both the content and 3D spatial orientation of PDL components. These features make our model well-suited to investigate in 3D the PDL cells-type I collagen structural arrangement which is critical for the core collagen remodeling function of the PDL (McCulloch et al. 2000).

Function: PTCs withstand constant mechanical stresses as occurs in the native PDL. A passive tensile strain is generated in PTCs owing to cell contractility and cell-collagen interactions (Figure 3.6, A, C, D, H). PTCs function for up to 4 weeks in the presence of this mild mechanical strain (Figure 3.6, E) and withstand actively applied tensile loads for up to a week, thus proving to be a robust mechanical model.

In this chapter, I have also demonstrated the use of the PTC model to study the biological effects of tensile loading. My research study has demonstrated a straightforward technique for applying a tensile load directly to PTCs with the simple placement of a bar magnet in the tensile stretching apparatus. Effects of tensile force application were studied with this model system at tissue, cellular and molecular scales. By incorporating an *in situ* tensile loading system, the PTC model fills a critical gap in periodontal mechanobiology investigations left by existing models. We chose to develop the tensile loading platform over a compressive one, firstly because far fewer models are available for tensile loading. This is primarily due to the difficulty in designing tensile load

application apparatus compared to the ease of a compressive one (Yang et al. 2015). Secondly, tensile loads are more predominant than compressive ones in the PDL under both physiologic and orthodontic tooth movement yet remain understudied in a 3D *in vitro* model (Beertsen et al. 1997; Cattaneo et al. 2005). Loading mechanisms in existing 3D *in vitro* mechanical models range from overly simplistic - ex. Flexcell plates, plastic coverslips with metal rings- to overly complicated - ex. actuators with complex motorized mechanisms, Velcro coated polycarbonate blocks moved with pins (Oortgiesen et al. 2012; Yang et al. 2015). Additionally, these models also lacked sufficient cell density or the native tissue-mimicking, organized cell-ECM structure and alignment observed in our PTCs. Importantly, our PTC model enables assessment of biological effects of tensile loading on multiple scales. On a tissue-level viscoelastic PTC behavior was characterized at three time-points. Cell numbers and ECM remodeling effects were assessed on a cellular scale. At the molecular level, gene expression changes and modifications in collagen, F-actin and aSMA structural elements in response to tension were characterized. This demonstrates the utility of the PTC model to conduct a detailed study on PDL behavior under mechanical loading far beyond that facilitated by existing 3D models.

The PTC model demonstrates how the ECM remodeling function of cells is reflected in observed biomechanical tissue properties such as PTC length and contractility. Due to the inherent design of the vertical, parallel posts, collagen fibers and cells in PTCs are suspended between the two posts and generate contractile forces in the process. This is reflected in reduction of PTC length to $7223 \pm 37$ μm and generation of contractile force ($738.63 \pm 35.6$ μN) by PTCs on day 3 after casting (Table 3.3). Comparatively, COCs which are control PTCs with no cells, had a length that remained unchanged from the inter-post distance of 8000 μm as no contractile force was generated. Corresponding structural changes in PTC collagen (Table 3.4) such as increase in fiber thickness, reduced length and alignment are indicative of ECM turnover by PDL cells

(Beertsen et al. 1997). Thus, our model facilitated tracking of tissue level change in contractile force with corresponding change in collagen structure through cellular remodeling.

*In vivo* PDL is likened to a complex, fiber-reinforced substance that responds to force in a viscoelastic, non-linear, and time-dependent manner (Wise and King 2006). This section describes similar time-dependent, viscoelastic responses observed on magnetically stretching the PTCs in the present study. These observations further validate our model's value as an investigative platform due to its proximity to *in vivo* PDL behaviour. PTC length significantly reduces on unloading from tensile stretching after 4 hours, compared to its stretched length (Figure 3.7, A). This is indicative of partial elastic recovery of PTC elements after being subjected to tensile deformation for 4 hours. Ability of the PDL to respond to applied force application through elastic recovery is considered critical to reduce PDL injury in case of excessive force or prolonged static deformation (Komatsu et al. 2004). Hence, the PTC model can be used to design studies investigating this critical PDL property. Additionally, PTCs after 4 hours of tensile stretch display some permanent deformation as they exhibit significant elongation compared to their pre-stretched length (Figure 3.7, A). PTCs stretched for 24 hours exhibit complete permanent elongation of PTCs with no elastic recovery, referred to as viscoplastic behavior (Figure 3.7, B). One week after stretching, tissue creep sets in, and PTCs elongate beyond the length at which they were stretched at the onset of force application (Figure 3.7, C). These observations are based on collagen fiber changes (Figure 3.13) seen after tensile stretching described in the section below.

Collagen is the predominant ECM component in the PDL and collagen structure is a major determinant of periodontal response to mechanical loads (Nanci 2012). PDL cells produce and organize collagen fibers in a hierarchical manner with triple helical twisted collagen molecules at the lowest level of hierarchy. Collagen molecules are then aggregated in both lateral and longitudinal directions to form fibrils, thus building up the diameter and length of fibrils. Multiple

fibrils are cross-linked with macromolecules like proteoglycans, fibronectin and small leucine-rich proteoglycans (SLRPs) like decorin, biglycan, fibromodulin and lumican form thicker and longer collagen fibers (Gautieri et al. 2011; Matheson et al. 2005). In a steady-state, collagen fibers of the PDL are entangled (Gauthier et al. 2021). Axial stretching is attributed to unraveling collagen sub-structures in a graded manner. Smaller strains straighten disordered and helically twisted collagen molecules, whereas prolonged or larger strains will cause uncoiling, stretching and straightening at the fibril level (Gauthier et al. 2021). Furthermore, fibrillar collagen molecules are held together by non-covalent bonds like electrostatic and hydrophobic bonds. So, an additional mechanism for viscoelastic behavior of collagen is the unbinding of these weak interactions allowing for fiber slippage. Slippage and re-coiling of collagen molecules could be the reason behind the behavior of PTCs stretched for 4 hours. Thus, the partial elastic recovery and partial permanent deformation seen in the 4 hr tensile loaded group could be due to re-coiling of the uncoiled collagen molecules and reformation of non-covalent bonds after tensile stretch cessation.

PTCs exhibited partial elastic recovery and mild permanent deformation on undergoing tensile stretch for 4 hours, possibly due to tensile force induced physical alterations in collagen structure and some early collagen remodeling by cells. The increase in fiber diameter after 4 hours of tensile stretching (Figure 3.13, A) could be taken to indicate new collagen fibrillogenesis. This could perhaps also be a contributor to the partial permanent deformation observed in this group, as new collagen fibers fill in gaps in the stretched tissues thus at least partially preventing the PTCs from reverting to their baseline length before magnetic stretch was applied (Figure 3.7, A). PDL cells synthesize and turnover collagen at the fastest rate compared to other tissues, rendering it plausible that fibrillogenesis and fiber thickening can occur after 4 hours of stretching (Hudson 2017). Rapid collagen fiber turnover could also account for the increase in fiber count and decrease in fiber alignment in the same group, although not statistically significant (Figure 3.13,

C, D). Alternatively, the reduction in fiber length and alignment, and increase in fiber count could be due to stretch-induced breakage of covalent bonds causing collagen fibers to rupture, leading to permanent deformation at the tissue level in the 4 hour tensile stretched PTCs. However, findings from *in vivo* experimental tooth movement that mechanical load instigates collagen production by cells indicate that collagen synthesis is a more likely explanation for the observed changes (Huang et al. 2016). Further molecular level studies are needed to pinpoint the exact changes in collagen ultrastructure corresponding to observed PTC behavior.

Tensile stretching PTCs for 24 hours caused significant permanent deformation and very little elastic recovery, driven presumably by tensile force induced physical alterations in collagen structure and cellular remodeling of collagen. In PTCs stretched for 24 hours, there is a statistically significant increase in collagen fiber thickness compared to its control and PTCs stretched for 1 week. There is a non-statistically significant trend of reduced fiber thickness, increased fiber length, decreased fiber count and increased fiber alignment observed in 24 hour tension group compared to 4 hour tension group (Figure 3.13). This could be taken to mean that newly formed shorter and thicker collagen fibers at 4 hours have had time over 24 hours to polymerize into longer and more aligned fibers. This structural alteration of collagen fibers through remodeling can be taken as the underlying cause of the complete permanent elongation of PTCs with no elastic recovery (Figure 3.7, B) after 24 hours of tension application. A component of the permanent tissue-level deformation could also be due to the collagen fiber rupture and covalent bond breakage. However, tensile stretching for 24 hours reduces contractile force only by 0.57% with no significant difference compared to 24 hour controls (Figure 3.8, J). This is considered as PTCs regaining their contractile force ability since the reduction in contractile force after 4 hours of stretching was 1.27% which was significantly lower than 4 hour controls (Figure 3.8, I). This regaining of contractile force in resistance to active tensile loading that occurs in PTCs, provides a stronger support for collagen polymerization and remodeling as the underlying cause of

viscoplastic behavior of PTCs at 24 hour stretch time-point, rather than breakage of collagen molecules. Prior studies have indeed corroborated the critical role of collagen fibers in providing tensile strength to the PDL by administering collagen polymerization inhibiting lathyrogens which caused tooth mobility in animal studies (Chiba et al. 1990).

Sustained tensile loading for a week resulted in permanent deformation and creep of the PTC longitudinal dimension accompanied by significant cellular remodeling of collagen and tensile force induced structural changes in the collagen molecules. Tensile stretching PTCs for 1 week led to a statistically significant increase in collagen fiber length and alignment and decrease in fiber thickness and count compared to the 1 week control, 4 hour tension and 24 hour tension groups (Figure 3.13). Biomechanical changes associated with collagen structural changes after 1 week of tensile loading were a significant reduction in PTC contractile force and creep induced increase in PTC length beyond its baseline length before tensile stretch was applied (Figure 3.7, C, Table 3.5). Van Driel et al. (2009) postulate that creep has two components - 1) material relaxation component due to changes in collagen fiber and 2) water flux component – made up of free, exchangeable water in interstitial fluid or non-exchangeable water which is bound by proteoglycan macromolecules in ECM. Significantly increased collagen fiber length and thinning of 1 week stretched PTCs due to collagen remodeling constitute the material relaxation component. Additionally, fiber thinning could also be due to exudation of the glycosaminoglycans and proteoglycans from the type 1 rat tail collagen used in the PTCs based on the *in vitro* study findings by Lam et al. (1993). The reduced fiber count seen with the 1 week tension group could be a combination of fusion of collagen fibrils to polymerize into longer fibers and digestion of collagen fibers by PDL fibroblasts with collagenase production or phagocytosis. This reduction in ECM content could be related to the increase in cell count observed in the 1 week tensile stretched group, which is discussed in the next section.

The co-occurrence of lower collagen fiber count and higher cell count observed in PTCs tensile stretched for a week could be attributable to the bilateral relationship between cell proliferation and ECM remodeling. Proliferating cells are known to create space by digesting ECM (Green et al. 1990). Enhanced creep, stress relaxation and higher loss of modulus of elasticity of collagen networks in turn promote spreading of adherent cells such as myofibroblasts, fibroblasts and mesenchymal stem cells (Chaudhuri et al. 2020). This observation was consistent with our study as the 1 week stretched PTCs that exhibited tissue creep had significantly higher cell numbers compared to the 1 week controls (Figure 3.9, D). Similarly, *in vivo* experimental tooth movement models have also demonstrated six-fold increase in cell proliferation in tension stimulated PDL along with upregulation of metalloproteinases to degrade collagen (Mabuchi et al. 2002; Kook et al. 2011). Furthermore the 1 week PTCs also displayed presence of differentiated myofibroblasts (Figure 3.12, D, H). These findings correspond with previous studies showing that biomechanical properties of microenvironment in tissues drive cell differentiation, fate and function (McBeath et al. 2004, Yamamoto et al. 2018). Thus, our platform can be used in future studies to control phenotypic conversion of stem cells for periodontal regeneration through changes in collagen fibrillogenesis and ECM biomechanical properties.

Tensile loading of PTCs led to increase in cellular alignment and enhanced F-actin levels as expected. Immunofluorescence analysis of PTC cells showed progressively more alignment along the tensile stretch axis over the 7-day period, more so when tension was applied (Figure 3.9, G, Figure 3.12). Other *in vitro* studies similarly show cells oriented parallel to principal orientation of deformation under static loading (Gauthier et al. 2021). This concordance in cell alignment with collagen alignment at a tissue level (Figure 3.12, Figure 3.14) along the tensile axis has also been demonstrated as a critical feature of *in vivo* PDL cells-collagen bundles arrangements (Pini et al. 2004, Gauthier et al. 2021). These inter-relationships are foundational for mechanical load dissipation and cell activity regulation in the PDL. Mechanical stretching is

known to activate the Rho/ROCK mechanotransduction pathway and upregulate F-actin formation (Martino et al. 2004), as was observed in our PTCs after tensile loading them for a week (Figure 3.9, E). Although increased F-actin production is supposed to increase cellular contractility, we observed a reduction in contractile force of PTCs at a tissue-level in the 1 week tension group (Figure 3.7, F, Figure 3.8, E). This discrepancy may be attributed to the creep response in PTC, which elongated under tension and thereby increased the distance between the silicone posts used to measure tissue-level force. It is unknown if the contractile forces of individual cells were affected by tensile loading in our study. However, F-actin levels on a per-cell basis were similar between tensile loaded and unloaded controls (Figure 3.11, A), so it is plausible that cellular forces were similar.

Tensile loading increased levels of aSMA indicating replacement of the usual beta-actin isomer in F-actin with alpha-smooth muscle actin isomer due to highly mechanically stimulating conditions. ASMA levels per unit area were higher in the 1 week tensile stretched PTCs compared to the controls. When assessed at per cell level, aSMA levels were higher for 24-hour tensile stretched group compared to the 1-week group (Figure 3.11, D). However, F-actin levels per cell dipped at the 24-hour time-point while increasing at the 4-hour and 1-week time-points (Figure 3.11, B). Thus, there appears to be an inverse relationship between F-actin and aSMA levels produced in our PTCs, which needs a closer look in future studies. In our study we also observed the appearance of characteristic aSMA stained myofibroblasts after tensile loading for a week (Figure 3.12, D, H ). Myofibroblasts were also seen in PTCs 3-days after casting (Figure 3.12, B-C). Perivascular cells and myofibroblasts in the PDL are aSMA positive cells, some of which may be progenitors of the osteoblast lineage. Detection of this highly specialized cell-type in our *in vitro* model was an unexpected and serendipitous novel finding. Future investigations into the nature, mechanisms of activation and functions of these myofibroblasts are definitely warranted to shed more light on this finding.

Our limited gene expression analysis corroborated the anabolic, matrix remodeling and osteogenic effects of tensile loads as previously known. We found tension to stimulate a higher number of DEGs at 24 hours (Figure 3.15, A) compared to 4 hours. The large number of cell cycle and cell death genes upregulated in the 24 hour tension group (Figure 3.15, B, Figure 3.17, A) corroborate the anabolic and cell proliferative effects of mechanical tension (Huang et al. 2016). DEGs highly expressed in the 24 hour tension group for collagen remodeling and mineralization overlapped with each other (Figure 3.17, B, C). Some of these genes were COMP (cartilage oligomeric matrix protein), SPP1 (secreted phosphoprotein 1), DMP1 (dentin matrix acidic phosphoprotein 1), BMP8B (bone morphogenetic protein 8b), IBSP (integrin binding sialoprotein), ADAMTSL2 (ADAMTS like 2), ADAMTS3 (ADAM metallopeptidase with thrombospondin type 1 motif 3), ADAMTS4 (ADAM metallopeptidase with thrombospondin type 1 motif 4), COL1A1 (collagen type 1 alpha 1 chain), COL1A2 (collagen type 1 alpha 2 chain), MMPs (matrix metalloproteinases ) and TIMPs (inhibitors of MMPs) (Figure 3.17, B, C). Genes like COMP, COL1A1 and COL1A2 are involved in collagen fibrillogenesis and ECM organization. The ADAMTSs and MMPs break down collagen and ECM protein assisting in tissue turnover. Thus, our observations of continued collagen fiber synthesis, polymerization and matrix turnover in PTCs stretched for 24 hours beyond that seen in PTCs stretched for 4 hours is supported by these transcriptomic findings. Osteogenic genes like BMP8B, IBSP, SPP1 and DMP1 that control osteoblast differentiation and mineralized matrix production were also upregulated more in the 24 hour tension group. This finding of upregulation of osteogenic genes due to tensile stretching is consistent with other studies showing that tension drives osteogenic changes (Meikle 2008; Sun et al. 2021; Janjić 2023).

Mechanical stretching is known to activate the Rho/ROCK mechanotransduction pathway and upregulate F-actin formation, along with TGF-b pathway activation and aSMA production (Martino et al. 2004; Meng et al. 2010). Consequently, genes related to F-actin cytoskeletal organization

like ACTN1( actinin alpha 1), FLNA (filamin A) along with genes for actin-regulating RhoGTPases like RhoA, Rac and CDC42 were also significantly upregulated in PTCs stretched for 24 hours compared to PTCs stretched for 4 hours (Figure 3.16, A). Combined with the previously stated observation of upregulated osteogenic genes, these findings provide a proof-of-principal for the mechanical stretch-mediated activation of osteogenic genes via the Rho-ROCK pathway in our model (Martino et al. 2004, Yamamoto et al. 2018). ASMA production is controlled TGF-beta pathway genes which seem split across both 4hour tension and 24 hour tension groups (Figure 3.16, B). However, the main gene for aSMA, which is ACTA2, is only upregulated in the 24 hour tension group, which may be a precursor for the elevated aSMA levels observed in the immunofluorescent analysis of 1 week tension tissues. Interestingly, despite seeing an upregulation of F-actin and aSMA genes in the 24 hour tension group, we see an upregulation of F-actin and aSMA at a protein level only in the one-week tension group, presumably because protein production trails mRNA synthesis.

To our knowledge, we have fabricated a first of its kind 3D PDL model that facilitates exploration of macro-scale tissue behavior and its links with underlying structural changes. Our model also facilitates convenient and direct measurement of tissue-generated contractile force. In the present study we have applied continuous, uniaxial tensile stretch. With further experimentation our model can be suitably modified to either apply cyclic tensile stresses or compressive force. Our PTCs provide an excellent platform for drug development, testing biological agents and elucidating molecular mechanisms. Multiple PTCs can be cast at a time, allowing experimentation on a large sample size for a fraction of a cost required for animal models. PTCs with varying ECM stiffnesses can be cast by modifying the collagen matrix concentration to explore ECM-stiffness and tissue contractile force based cell phenotype determination. Mapping stiffness or force values to their cell differentiation effects is a powerful tool to elicit clinical need-based directed cell differentiation

such as either osteogenic or osteoclastogenic response within the periodontium. This has profound translational implications for a host of clinical issues including for repair and regeneration of periodontitis-afflicted tissues, determination of optimum orthodontic force to effectuate tooth movement, retention after orthodontic treatment and implant osseointegration. A significant hurdle in periodontal regeneration has been repopulation of periodontal defects with cells producing biochemical factors to maintain the PDL in an unmineralized state while simultaneously promoting mineralization of adjacent bone and cementum layers. Transplanting *in vitro* fabricated PDL grafts such as ours, which has PDL cells and collagen in an organized, structured matrix, could provide a feasible alternative to drive the desired cellular functions necessary for periodontal regeneration. Unlike cell sheets used for transplantation in periodontal defects, our PTCs would not need heat for detachment as they can be easily dismounted within seconds while fully maintaining their intact anatomy. PTCs could also potentially offer a plausible alternative to bioprinting or injecting cells in an unorganized matrix approach for periodontal regeneration. PTCs can also be modified for use in conjunction with microfluidic devices or organ-on-a-chip model to elaborate fluid shear flow mechanisms or neurovascular interactions by co-culturing with endothelial and neural cells (Huang et al. 2023). These are the various applications which our PTC platform offers for future investigations.

Some of the limitations of our study are that the model size and scale of forces are not the same as *in vivo* PDL. Our model is relatively unconstrained compared to *in vivo* tissue which is enclosed circumferentially by alveolar bone and tooth root. The modulus of elasticity of our PTC model has not been measured so its resemblance to *in vivo* PDL in this feature is unknown. It is also difficult to match the in vitro model's modulus to that of in vivo PDL particularly due to the lack of consensus on its actual value, which range from 0.01 to 1750 MPa (Fill et al. 2011) The gene expression analysis we carried out was limited only to the early changes in this study, since we plan to conduct a more extensive analysis on osteogenesis and mineralization of PTCs in

response to tension on a longer time scale in the future. Through our paper, we have elaborated fabrication of a novel 3D *in vitro* PDL model which has multi-purpose research applications and translational potential. With the molecular level configurations embodying the physiologic cell-ECM architecture, we can expect that our model would recapitulate the cellular behavior patterns expected in native tissue with greater accuracy than existing models.

## 3.6 REFERENCES


Aveic S, Craveiro RB, Wolf M, Fischer H. Current trends in in vitro modeling to mimic cellular crosstalk in periodontal tissue. Advanced Healthc Mater. 2021;10(1):2001269.

Beertsen W, McCulloch CA, Sodek J. The periodontal ligament: a unique, multifunctional connective tissue. Periodontol 2000. 1997;13(1):20-40.

Berkovitz BK. The structure of the periodontal ligament: an update. Eur J Orthod. 1990;12(1):51-76.

Bhandari S. Engineering a novel device to implement afterload on human stem cell-derived cardiac tissues (Doctoral dissertation).

Bielawski KS, Leonard A, Bhandari S, et al. Real-time force and frequency analysis of engineered human heart tissue derived from induced pluripotent stem cells using magnetic sensing. Tissue Eng Part C 2016; 22: 932–940.

Bremner, S., Goldstein, A. J., Higashi, T., & Sniadecki, N. J. (2022). Engineered heart tissues for contractile, structural, and transcriptional assessment of human pluripotent stem cell-derived cardiomyocytes in a three-dimensional, auxotonic environment. In Cardiac Tissue Engineering: Methods and Protocols (pp. 87-97). New York, NY: Springer US.

Cattaneo PM, Dalstra M, Melsen B (2005). The finite element method: a tool to study orthodontic tooth movement. J Dent Res 84:428-433.

Chaudhuri O, Cooper-White J, Janmey PA, Mooney DJ, Shenoy VB. Effects of extracellular matrix viscoelasticity on cellular behaviour. Nature. 2020 Aug 27;584(7822):535-46.

Chiba M, Yamane A, Ohshima S, Komatsu K. In vitro measurement of regional differences in the mechanical properties of the periodontal ligament in the rat mandibular incisor. Arch Oral Biol. 1990;35(2):153-61.

Feng L, Yang R, Liu D, Wang X, Song Y, Cao H, He D, Gan Y, Kou X, Zhou Y. 2016. PDL progenitor–mediated PDL recovery contributes to orthodontic relapse. J Dent Res. 95(9):1049-56.

Fill TS, Carey JP, Toogood RW, Major PW. Experimentally determined mechanical properties of, and models for, the periodontal ligament: critical review of current literature. J Dent Biomech. 2011;2011:312980. doi: 10.4061/2011/312980. Epub 2011 Apr 5. PMID: 21772924; PMCID: PMC3134825.

Gauthier R, Jeannin C, Attik N, Trunfio-Sfarghiu AM, Gritsch K, Grosgogeat B. Tissue engineering for periodontal ligament regeneration: Biomechanical specifications. J Biomech Eng. 2021;143(3):030801.

Gautieri A, Vesentin S, Redaelli A, Buehler MJ. Hierarchical structure and nanomechanics of collagen microfibrils from the atomistic scale up. Nano lett. 2011;11(2):757-66.

Green DD, Hembry RM, Atkinson SJ, Reynolds JJ, Meikle MC. Immunolocalization of collagenase and tissue inhibitor of metalloproteinases (TIMP) in mechanically deformed fibrous joints. Am J Orthod Dentofacial Orthop. 1990;97(4):281-8

Hirashima S, Ohta K, Kanazawa T, Okayama S, Togo A, Uchimura N, Kusukawa J, Nakamura KI. Three-dimensional ultrastructural analysis of cells in the periodontal ligament using focused ion beam/scanning electron microscope tomography. Sci Rep. 2016;6(1):1-9.

Huang L, Liu B, Cha JY, Yuan G, Kelly M, Singh G, Hyman S, Brunski JB, Li J, Helms JA. Mechanoresponsive properties of the periodontal ligament. J Dent Res. 2016;95(4):467-75.

Huang D, Li Y, Ma Z, Lin H, Zhu X, Xiao Y, Zhang X. Collagen hydrogel viscoelasticity regulates MSC chondrogenesis in a ROCK-dependent manner. Sci Adv. 2023;9(6):eade9497.

Huang, C., Sanaei, F., Verdurmen, W. P. R., Yang, F., Ji, W., & Walboomers, X. F. (2023). The Application of Organs-on-a-Chip in Dental, Oral, and Craniofacial Research. J Dent Res. 102(4), 364-375.

Hudson DM, Garibov M, Dixon DR, Popowics T, Eyre DR. Distinct post-translational features of type I collagen are conserved in mouse and human periodontal ligament. J Periodontal Res. 2017;52(6):1042-9.

Janjić K, Nemec M, Maaser JL, Sagl B, Jonke E, Andrukhov O. 2023. Differential gene expression and protein-protein interaction networks of human periodontal ligament stromal cells under mechanical tension. Eur J Cell Biol. 102(2):151319.

Jónsdóttir SH, Giesen EB, Maltha JC. 2006. Biomechanical behaviour of the periodontal ligament of the beagle dog during the first 5 hours of orthodontic force application. Eur J Orthod. 28(6):547-52.

Kang KL, Lee SW, Ahn YS, Kim SH, Kang YG. Bioinformatic analysis of responsive genes in two-dimension and three- dimension cultured human periodontal ligament cells subjected to compressive stress. J Periodontal Res. 2013;48(1):87–97.

Kook SH, Jang YS, Lee JC. Involvement of JNK-AP-1 and ERK-NF-κB signaling in tension-stimulated expression of type I collagen and MMP-1 in human periodontal ligament fibroblasts. J Appl Physiol. 2011;111(6):1575-83.

Komatsu K, Kanazashi M, Shimada A, Shibata T, Viidik A, Chiba M. Effects of age on the stress–strain and stress–relaxation properties of the rat molar periodontal ligament. Arch Oral Biol. 2004;49(10):817-24.

Lam TC, Frank CB, Shrive NG. Changes in the cyclic and static relaxations of the rabbit medial collateral ligament complex during maturation. J biomech. 1993;26(1):9-17.

Langmead, B. et al. Fast gapped-read alignment with Bowtie 2. Nat. Methods. 2012;9:357-359.

Lanir Y, Salant EL, Foux A. Physico-chemical and microstructural changes in collagen fiber bundles following stretch in-vitro. Biorheology. 1988;25(4):591-603. doi: 10.3233/bir-1988-25401. PMID: 3252915.

Li B, Dewey CN. RSEM: accurate transcript quantification from RNA-Seq data with or without a reference genome. BMC Bioinformatics. 2011;12:323.

Liao W, Okada M, Inami K, Hashimoto Y, Matsumoto N. Cell survival and gene expression under compressive stress in a three-dimensional in vitro human periodontal ligament-like tissue model. Cytotechnology. 2016;68(2):249-60. doi: 10.1007/s10616-014-9775-3. Epub 2014 Aug 3. PMID: 25087076; PMCID: PMC4754250.

Liu Y, Keikhosravi A, Pehlke CA, Bredfeldt JS, Dutson M, Liu H, Mehta GS, Claus R, Patel AJ, Conklin MW, Inman DR, Provenzano PP, Sifakis E, Patel JM, Eliceiri KW. Fibrillar collagen quantification with curvelet transform based computational methods. Front Bioeng Biotechnol. 2020;8:198. doi: 10.3389/fbioe.2020.00198

Mabuchi R, Matsuzaka K, Shimono M. Cell proliferation and cell death in periodontal ligaments during orthodontic tooth movement. J Periodontal Res. 2002;37(2):118-24.

Martino F, Perestrelo AR, Vinarský V, Pagliari S, Forte G. Cellular mechanotransduction: from tension to function. Front Physiol. 2018;9:824.

McBeath R, Pirone DM, Nelson CM, Bhadriraju K, Chen CS. Cell shape, cytoskeletal tension, and RhoA regulate stem cell lineage commitment. Dev Cell. 2004;6(4):483-95.

McCulloch CA, Lekic P, Mckee MD. Role of physical forces in regulating the form and function of the periodontal ligament. Periodontol 2000. 2000;24(1):56-72.

Matheson S, Larjava H, Häkkinen L. Distinctive localization and function for lumican, fibromodulin and decorin to regulate collagen fibril organization in periodontal tissues. . J Periodontal Res. 2005;40(4):312-24.

Oortgiesen DA, Yu N, Bronckers AL, Yang F, Walboomers XF, Jansen JA. A three-dimensional cell culture model to study the mechano-biological behavior in periodontal ligament regeneration. Tissue Eng Part C Methods. 2012 Feb;18(2):81-9. doi: 10.1089/ten.TEC.2011.0367. Epub 2012 Jan 4. PMID: 21913838; PMCID: PMC3262976.

Meng Y, Han X, Huang L, Bai D, Yu H, He Y, Jing Y. 2010. Orthodontic mechanical tension effects on the myofibroblast expression of alpha-smooth muscle actin. Angle Orthod. 80(5):912-8.

Nanci A. Ten Cate's Oral Histology. 2012. Development, Structure, & Function. Mosby.

Meikle MC. 2005. The tissue, cellular, and molecular regulation of orthodontic tooth movement: 100 years after Carl Sandstedt. Eur J Orthod. 28:221–40

Pini M, Zysset PH, Botsis J, Contro R. Tensile and compressive behaviour of the bovine periodontal ligament. J Biomech. 2004;37(1):111-9.

Roguljic H, Matthews BG, Yang W, Cvija H, Mina M, Kalajzic I. 2013. In vivo identification of periodontal progenitor cells. J Dent Res. 92(8):709-15.

Ruiz SA, Chen CS. 2008. Emergence of patterned stem cell differentiation within multicellular structures. Stem cells. 26(11):2921-7.

Sun C, Janjic Rankovic M, Folwaczny M, Otto S, Wichelhaus A, Baumert U. Effect of tension on human periodontal ligament cells: systematic review and network analysis. Front Bioeng Biotechnol. 2021;9:695053.

Sniadecki NJ and Chen CS. Microfabricated silicone elastomeric post arrays for measuring traction forces of adherent cells. Methods Cell Biol. 2007; 83: 313–328.

Somerman MJ, Archer SY, Imm GR, Foster RA. (1988). A comparative study of human periodontal ligament cells and gingival fibroblasts in vitro. J Dent Res. 1988;67(1), 66-70.

Van Driel WD, van Leeuwen EJ, Von den Hoff JW, Maltha JC, Kuijpers-Jagtman AM. Time-dependent mechanical behaviour of the periodontal ligament. Proc Inst Mech Eng H. 2000;214(5):497-504. doi:10.1243/0954411001535525

Wang L, Feng Z, Wang X, et al. DEGseq: an R package for identifying differentially expressed genes from RNA-seq data[J]. Bioinform. 2010;26(1):136-138.

Wise GE, King GJ. Mechanisms of tooth eruption and orthodontic tooth movement. J Dent Res. 2008;87(5):414-34.

Yamamoto T, Ugawa Y, Kawamura M, Yamashiro K, Kochi S, Ideguchi H, Takashiba S. Modulation of microenvironment for controlling the fate of periodontal ligament cells: the role of Rho/ROCK signaling and cytoskeletal dynamics. Cell Commun Signal. 2018;12(1):369-78

Yang L, Yang Y, Wang S, Li Y, Zhao Z. In vitro mechanical loading models for periodontal ligament cells: From two-dimensional to three-dimensional models. Arch Oral Biol. 2015;60(3):416–424.doi:10.1016/j.archoralbio.2014.11.012.

# CHAPTER 4. BIOENGINEERING A NOVEL 3D BONE-PDL-BONE IN VITRO MODEL

## 4.1 ABSTRACT

PDL attachment to alveolar bone and cementum is a key structural element that determines PDL function and behavior. These points of attachments constitute a critical transition zone or enthesis for stress distribution and functional adaptation during oral functions. 3D *in vitro* models that reproduce the multi-layered architecture and entheses characteristic of the PDL are currently lacking. Hence, our objective was to bioengineer a 3D *in vitro* bone-PDL-bone tissue construct that would embody these characteristics and be potentially useful for mechanobiology research and periodontal regeneration applications.

We used the suspended tissue open microfluidic patterning (STOMP) system to create a spatially patterned tissue construct between two silicone posts. Two cell types were used – a) PDL cells obtained from extracted premolars of healthy patients, and b) osteoblastic cells obtained by treating PDL cells with osteogenic induction medium. PDL cells mixed with 4 mg/ml type I rat tail collagen were pipetted in the center of the STOMP microfluidic channel. Next, osteoblasts in collagen mixture were pipetted on either side of the PDL cell-collagen mixture to surround tips of the posts. After incubating patterned tissues for 48 hours at 37 °C, the microfluidic channel templates were removed. Thus, our technique produced a free-standing, osteoblast-PDL-osteoblast 3D *in vitro* tissue construct, suspended between two posts. Analysis with microscopy detected formation of a zigzag region resembling cellular enthesis between PDL and osteoblastic cells on either side. Immunofluorescent staining demonstrated aligned PDL cells similar to *in vivo* architecture. Based upon deflection of silicone posts, we noted the tissue constructs (n=6) generated a force of around 439 ± 65.7 uN.

We have developed a novel 3D *in vitro* multi-layered PDL model with two different cell types and a cellular enthesis constituted by PDL and osteoblastic cells. Our model provides a potentially valuable platform to investigate cell biomechanics, mechanotransduction and tissue behaviour at the junction of disparate cell types. It also has significant translational potential for periodontal therapeutic and regenerative applications. Additionally, this model can be further improved to create a cementum-PDL-bone model.

## 4.2 INTRODUCTION

PDL behavior is dependent as much on the architectural arrangement of its content as its composition. Region-specific cell differentiation to maintain the cementum, PDL and alveolar bone layers of the periodontium is especially important for structural and functional integrity. Reproducing this multi-layered configuration along with the entheses between the layers is critical to build a biomimetic 3D *in vitro* PDL model. Currently, lack of such a model results in under-investigated cellular and molecular mechanisms that occur at the entheses and underly periodontal health, disease and regeneration. Such a model, with region-specific pre-assembly and priming of cells in a 3D matrix, has also been long sought as a transplantation graft for *in vivo* periodontal regeneration. Especially, since current regenerative strategies range from using bone grafts, cell sheets and growth factors to bioprinting and scaffold-mediated cell delivery systems have limited clinical efficacy (Galli et al. 2021). Hence, the objective of the present study was to bioengineer an *in vitro* periodontal tissue construct (PTC) model that incorporates spatially patterned regions with different cell types and their cellular entheses for both clinical regeneration and research applications. The suspended tissue open microfluidic patterning (STOMP) system consists of an assembly of microfluidic devices and a post array. By incorporating the STOMP technique, we aim to create a spatially patterned 3D *in vitro* periodontal tissue.

## 4.3 MATERIALS AND METHODS

### *4.3.1 Primary PDL cell isolation*

PDL cells were harvested using pre-established protocols (Somerman et al. 1988) from the roots of healthy premolars, which had been extracted for orthodontic purposes in a 13 year-old male patient. Briefly, PDL tissue was gently dissected from the middle third of the tooth root surface in a culture dish containing wash buffer [Hanks' balanced salt solution (HBSS; Gibco) supplemented with 5% (v/v) fetal bovine serum (FBS; HyClone) and 50 U/mL penicillin and 50 µg/mL streptomycin]. The suspension was centrifuged at 400×g for 10 min at 4°C. After aspirating the supernatant, PDL tissue was digested in collagenase I (3 mg/mL, Sigma- Aldrich) and dispase II (4 mg/mL; Sigma-Aldrich) for 1 hour at 37°C. After digestion, the suspension was passed through a 70 µm strainer to obtain a single-cell suspension. The cell population was expanded by seeding the single-cell suspension in 24-well plates. Cells were grown in standard PDL cell culture medium of Dulbecco's Modified Eagle Medium (DMEM; Gibco) supplemented with 10% FBS (HyClone) and 1% penicillin/ streptomycin (Gibco) at 37°C with 5% $CO_2$. On reaching confluence, cells were washed with PBS, trypsinized with 0.25% trypsin-EDTA (Gibco) and passaged progressively into T-75 and T-175 flasks. Cells at passage numbers 1 to 3 were stored in freezing media Cryostor (1 mL per 10 million cells) in a liquid nitrogen freezer then thawed, plated, and expanded as needed in T-75 and T-175 flasks. PDL cells between passage numbers 3 and 8 were used for the experiments.

### *4.3.2 Osteoblast induction*

To induce osteoblast differentiation, a sub-population of PDL cells between passages 3 to 6, was transferred to a T-75 flask and cultured in the DMEM media with 10% FBS and 1% penicillin-streptomycin. The cells were left to grow up to 80-90% confluence with culture medium changes every 3 days before adding osteogenic induction medium (control medium supplemented with 50

μM ascorbic acid- 2-phosphate, 10 mM β-glycerophosphate, and 10 nM dexamethasone) for 10 days. On day 10, these cells were trypsinized and lifted to cast patterned tissues, as described in the next section.

### *4.3.3 Fabricating post arrays and open microfluidic patterning devices*

Engineering patterned periodontal tissue constructs required two components – a) a post array (Figure 4.1, A) and b) a suspended tissue open microfluidic patterning (STOMP) device (Figure 4.1, B). To fabricate the post array, a four-part acrylic mold (designed in-house) was assembled (Figure 3.1). Capillary tubes with 1 mm outer diameter were cut into six 14 mm long sections. One section was placed in each of the six vertical post channels on one side of the assembled mold to prepare rigid posts. One neodymium magnet cube (1 $mm^3$, SuperMagnetMan) was inserted into each of the six contralateral vertical posts that would eventually become flexible posts. Two full-length 1.1 mm outer diameter capillary tubes were placed on either side of the mold base (for a total of 4) to provide structural support to the base. A 10:1 mixture of Sylgard 184 polydimethylsiloxane (PDMS; Krayden) was prepared by mixing 10 parts of base component with one part of curing agent for five minutes. After degassing the PDMS under vacuum to remove bubbles, it was poured into the mold and cured for 18 hours at 65ºC. On cooling, the post array was then carefully cut from the mold using a razor blade.

The STOMP system consisting of open microfluidic patterning rail and clips were designed in Solidworks 2020 and 3D printed out of clear resin using a Form 3B+ 3D printer (Formlabs Inc.). Dimensions of the open channel were designed to fit around the PDMS posts. Clips were designed to hold the patterning rail in place during the tissue patterning process. The patterning devices (rail and clips) were cleaned in two separate FormWash units (Formlabs Inc.) with isopropyl alcohol (IPA) for 20 minutes and then another 10 minutes to remove excess uncured resin. The devices were dried with compressed air and cured under UV light at 60°C for 15 minutes in a FormCure (Formlabs Inc.).

### *4.3.4 Casting patterned tissues*

Prior to casting, PDMS post arrays and patterning devices were submerged in 70% ethanol for 10 min, rinsed with sterile deionized water for 10 min, then UV sterilized for 10 min. Arrays were then transferred to the tissue-culture hood. Posts were then dipped sequentially in a 24-well plate containing 2.5 mL/well of 0.1% PEI for 10 min, sterile deionized water for 5 min, 0.01% glutaraldehyde for 30 min, then rinsed twice in sterile DI water for 5 min and set aside to dry. The patterning rails that were to be used with a cell-laden hydrogel or ECM were incubated in a solution of 1% bovine serum albumin (BSA) for 1 hour. After incubation, the 1% BSA solution was

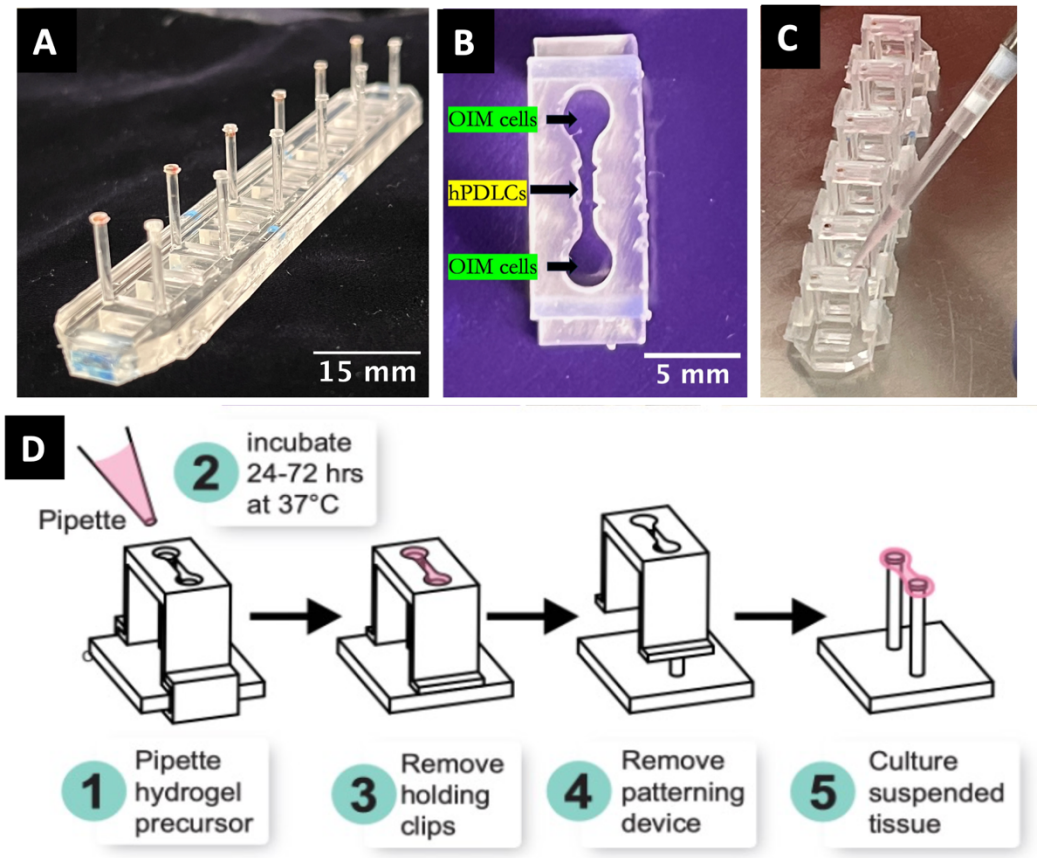


**Figure 4.1. Procedure for casting 3D tissues to create bone-PDL-bone enthesis.** (A) Polydimethylsiloxane (PDMS) post. (B) Regions of the STOMP rail. (C) Assembled STOMP on posts. (D) Schematic of patterning osteoblasts and PDL cells in collagen gel to generate 3D tissue constructs with bone-PDL- bone entheses. (Fig. 2D image courtesy Brown LG and Haack AJ from Theberge Lab at University of Washington, Department of Chemistry)

aspirated, and the patterning rails were allowed to fully dry prior to assembling the suspended tissue open microfluidic patterning devices. Then each open microfluidic patterning rail was placed such that it surrounded the ends of a pair of posts, and the clips were used to hold the patterning rail in place at the base of the PDMS post array (Figure 4.1, C, D).

To pattern tissues, two different cell-collagen mixtures were prepared by using the two cell types - the PDL cells and the osteoblastic cells obtained by treating PDL cells with osteogenic induction medium. To prepare the cell-collagen mixtures, each cell type was mixed with type I rat tail collagen such that a 100 µL cell-collagen mixture was composed of 1:4 ratio of cell solution (20 µL culture media containing 300,000 cells) and collagen mixture [80 µL of 9 parts of collagen (4 mg/mL; Advanced Biomatrix) mixed with 1 part of neutralization solution (Advanced Biomatrix)]. First, 13 µL of osteoblast collagen-mixture was pipetted on one end of the STOMP channel and then the other. Then, 3-4 µL of PDL cell-collagen mixture was pipetted in the center of the STOMP channel (Figure 4.1, C, D). The PDMS post array, with the patterned cell solutions cast along the patterning rail held to the post array by clips, was then placed upside down in a 24-well plate. The assembly transferred to the incubator at 37°C with 5% $CO_2$. After 90 min, 1 mL of culture media was gently added to the wells containing the cast PTCs and then incubated again at 37°C. After 48 hours, the clips and patterning rails were removed to reveal a suspended tissue between the PDMS posts. These patterned PTCs were then transferred to a fresh 24-well plate with 2.5 mL/well of culture medium, which was changed every 2 to 3 days. Similarly, patterned control tissues consisting of bone cells in all 3 regions (referred to as BBB) and periodontal cells in all 3 regions (referred to as PPP) were also cast.

### 4.3.5 Calculation of PTC contractile force

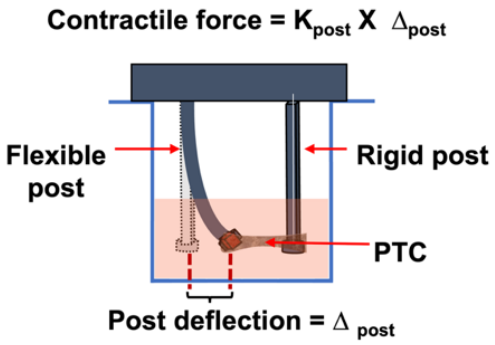


**Figure 4.2. Contractile force calculation for PTCs**

Contractile force generated by PTCs was calculated by quantifying the magnitude of deflection they caused in the post pairs they were cast on. Based on a modulus of elasticity of 2.5 MPa for PDMS, the bending stiffness ($K_{post}$) of the flexible posts was calculated to be 0.95 μN/μm, as done previously (Bielawski et al. 2016). Contractile force was calculated by multiplying the bending stiffness by the deflection of the post ($\Delta_{post}$) (Figure 4.2).

### 4.3.6 Immunofluorescence imaging

PTCs on posts were fixed in 4% paraformaldehyde (PFA; VWR) at room temperature for 1 hour. PTCs were then dismounted from the posts for the immunofluorescence staining process. In short, PTCs were permeabilized with 0.2% Triton-X for 10 min followed by blocking with 10% normal goat serum (Invitrogen) for 10 min at room temperature. Samples were then incubated for 1 hour with mouse primary antibodies for alpha-smooth muscle actin (aSMA, Santa Cruz Biotechnology, 1:100), followed by 3X, 10 min PBS rinses on a room temperature shaker. PTCs were then treated with goat anti-mouse Alexa Fluor 488 (Invitrogen A28175, 1:200), Alexa Fluor 647 phalloidin (Invitrogen A22287, 1:400), and Hoechst 33342 (ThermoFisher, 1:1000). After 1 hour, PTCs were again rinsed thrice in PBS for 10 min each on a room temperature shaker. Whole PTCs were then coversliped in VECTASHIELD mounting medium and allowed to dry overnight. A Leica SP8 confocal microscope was used for imaging. Three to four images per PTC were

obtained under 10X objective at 2X zoom and 1024 X 1024 resolution. Since three independent experiments were carried out and each experiment was conducted in triplicate, we ensured a minimum of 30 images per condition for analysis. Laser strength and gain were kept constant between all samples and fields of view. F-actin and aSMA fluorescence intensities were quantified using Fiji image analysis software. Cell alignment was calculated using Directionality plugin in Fiji.

### *4.3.7 Alkaline phosphatase staining*

PTCs on posts were fixed in 4% paraformaldehyde (PFA; VWR) at room temperature for 1 hour and then dismounted. Alkaline phosphatase (ALP) staining was carried out using Vector® Red ALP substrate (Vector Laboratories SK-5100). Working solution was prepared by adding a drop each of the Vector Red reagents 1, 2 and 3 to 5 ml of 100 mM - 200 mM Tris-HCl, pH 8.2 - 8.5 buffer. PTCs were incubated in 500 µL of the working solution for 30 min and then rinsed thrice in buffer for 5 mins each time. PTCs were then treated with Alexa Fluor 647 phalloidin (Invitrogen A22287, 1:400), and Hoechst 33342 (ThermoFisher, 1:1000). After 1 hour, PTCs were rinsed thrice in PBS for 10 min each on a room temperature shaker. Whole PTCs were then coversliped in VECTASHIELD mounting medium and allowed to dry overnight. Tissues were imaged using a Leica SP8 confocal microscope with a 10X or 20x air objective and a Nikon Ti-E widefield microscope with 40X oil objective. Laser strength and gain were kept constant between all samples and fields of view for the confocal imaging. Images were processed using the FIJI image analysis software.

### *4.3.8 Statistical analysis*

Data were collected from three independent experiments. All values are expressed as mean ± standard error of mean. Results were compared using one-way ANOVA with post-hoc comparisons using GraphPad Prism. Differences with p-values $<0.05$ were considered statistically significant.

## 4.4 RESULTS

### *4.4.1 STOMP patterned PTCs exhibit distinct cell layers and cellular enthesis*

The open microfluidic patterning system resulted in formation of patterned tissues suspended between two posts (Figure 4.3, A). The STOMP patterned tissues (on the left side in Figure 4.3, A) were slender compared to regular PTCs fabricated without using microfluidic devices (on the right side in (Figure 4.3, A) as described in Chapter 3. The arrangement of osteoblasts on either sides of the microfluidic channel and the PDL cells in the center of the PTCs (Bone-PDL-Bone;

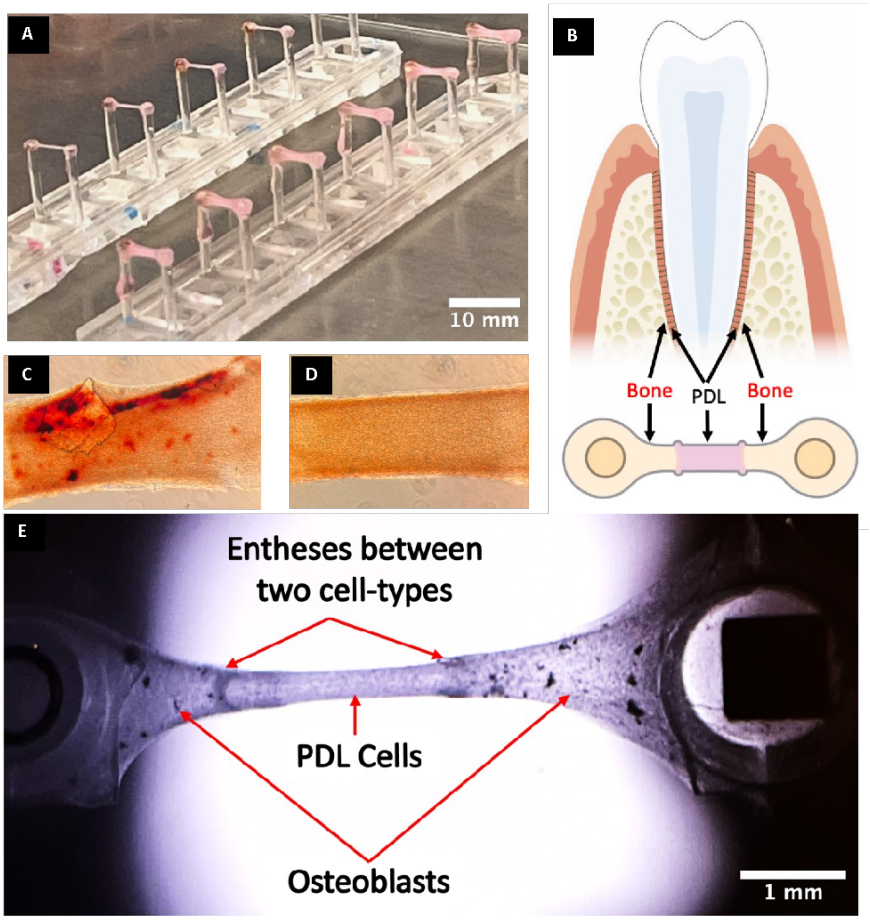


**Figure 4.3. 3D patterned PDL tissue constructs (PTC).** A. PTCs formed after removal of STOMP components. B. Schematic of patterned tissues corresponding with in vivo PDL structures. C. Alizarin red assay showing mineralized deposits of bone seen in control PTCs patterned with osteoblasts in all 3 zones of the microfluidic channel (BBB). D. No mineralized deposits were seen in PPP tissues patterned with PDL cells. E. Patterned PTC observed at 2X brightfield microscopy.

BPB) mimics the bone-PDL-bone arrangement found *in vivo*, as depicted in, B. Patterned PTCs made only from bone cells in all 3 regions - BBB – exhibited alizarin red stained mineralized nodules all over (Figure 4.3, C), whereas PPP controls did not exhibit such nodules (Figure 4.3, D). A clear demarcation between the osteoblasts and PDL cells in the center was found when the BPB PTCs were observed under brightfield microscopy, indicating formation of a cellular enthesis (Figure 4.3, E). Patterned PTCs were able to survive for at least two weeks without snapping or dissolving from the suspended posts, under normal culturing conditions.

### *4.4.2 STOMP patterned PTCs generated contractile forces*

Cells in the PTCs caused the 3D tissues to contract, pulling the flexible post towards the center, which was quantified as change in length and deflection of posts (Table 4.16). PPP PTCs generated the highest contractile force with a mean of 579.5 μN, followed by BPBs with a mean of 463.13 μN and least generated by BBB with a mean of 433.83 μN. However, differences were not statistically significant (Figure 4.4)

**Table 4.16. Contractile force analysis**

| | **Tissue length (μm)** | **Post Deflection (8000-tissue length) (μm)** | **Contractile Force (Deflection of post *0.95) (μN)** |
|---|---|---|---|
| **PPP (n = 4)** | 7440 | 560 | 532 |
| | 7430 | 570 | 541.5 |
| | 7410 | 590 | 560.5 |
| | 7280 | 720 | 684 |
| | | | **Mean ± SEM - 579.5 ± 35.33** |
| | | | |
| **BPB (n = 4)** | 7720 | 280 | 266 |
| | 7570 | 430 | 408.5 |
| | 7430 | 570 | 541.5 |
| | 7330 | 670 | 636.5 |
| | | | **Mean ± SEM - 463.13 ± 80.65** |
| | | | |
| **BBB (n = 6)** | 7410 | 590 | 560.5 |
| | 7450 | 550 | 522.5 |
| | 7560 | 440 | 418 |
| | 7470 | 530 | 503.5 |
| | 7680 | 320 | 304 |
| | 7690 | 310 | 294.5 |
| | | | **Mean ± SEM - 433.83 ± 46.65** |

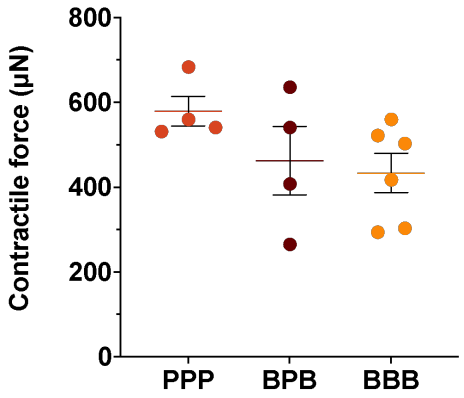


**Figure 4.4. Quantification of contractile force of PTCs.** One-way ANOVA found no significant differences between groups. PPP - Control PTCs with only PDL cells; BBB- Control PTCs with only osteoblasts; BPB – Osteoblast-PDL-Osteoblast PTCs.

### *4.4.3 STOMP generated PTCs display distinct morphological characteristics on immunofluorescent imaging*

BPB PTCs that were fabricated by patterning osteoblast-collagen gel at the ends and the PDL-collagen gel in the center of the microfluidic channel were found to maintain these two cell populations in their specific locations even after removal of the STOMP devices. PTCs were also found to have a distinct suture-like demarcation between osteoblasts and PDL cells on either sides (Figure 4.5). This structure seems like a cellular or soft-tissue analogue of the *in vivo* alveolar bone-PDL enthesis.

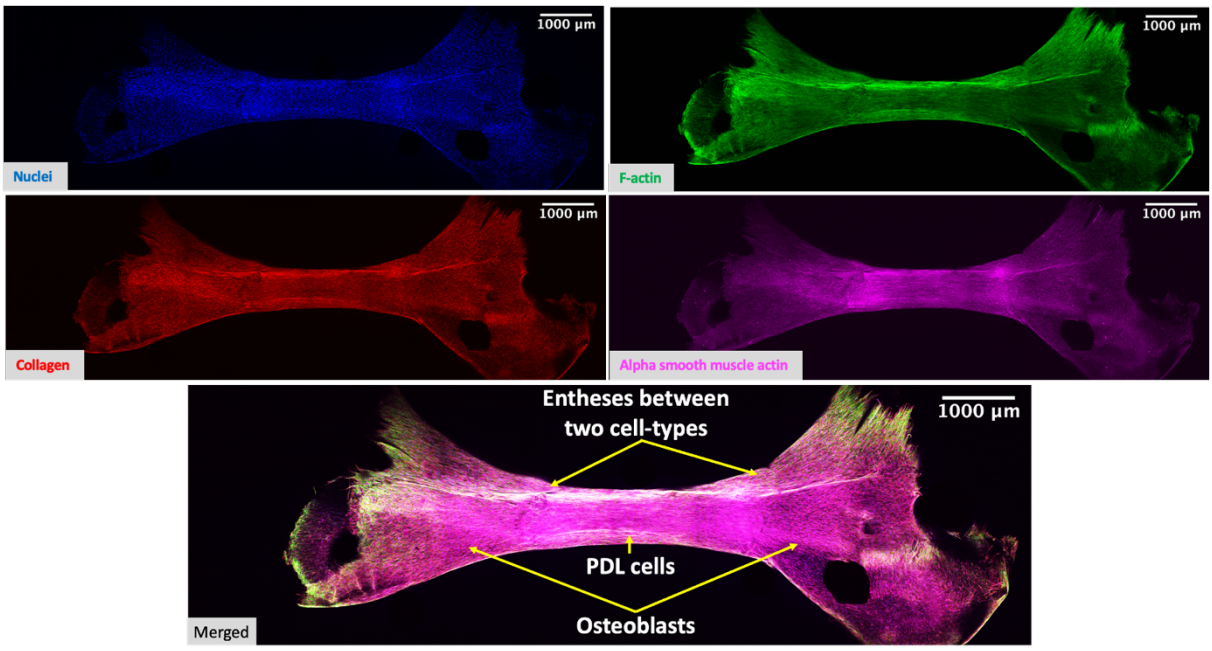


**Figure 4.5. Confocal images of BPB patterned PTC**

### 4.4.4 *Cells within the STOMP patterned PTCs displayed region-specific, structural characteristics distinctive of either the osteoblastic or periodontal phenotype*

Qualitative comparisons of the entheses in control PTCs - PPP or BBB – revealed distinct cellular morphology and alkaline phosphatase staining in each tissue type. PDL cells in the PPP enthesis

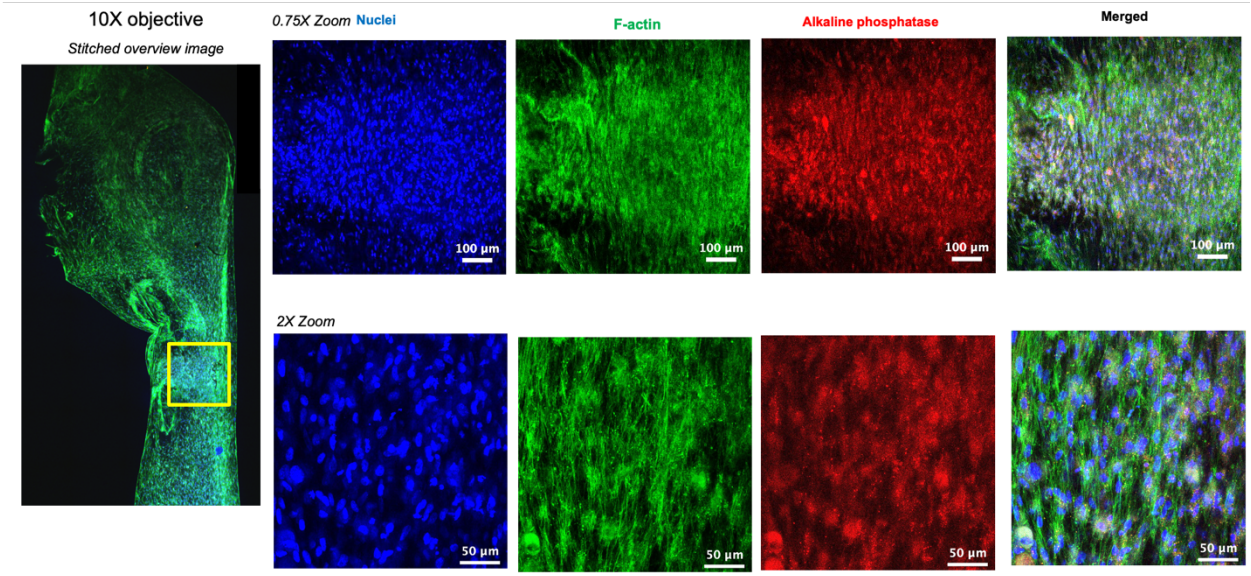


**Figure 4.6. Confocal images of PDL cells in PPP enthesis region**

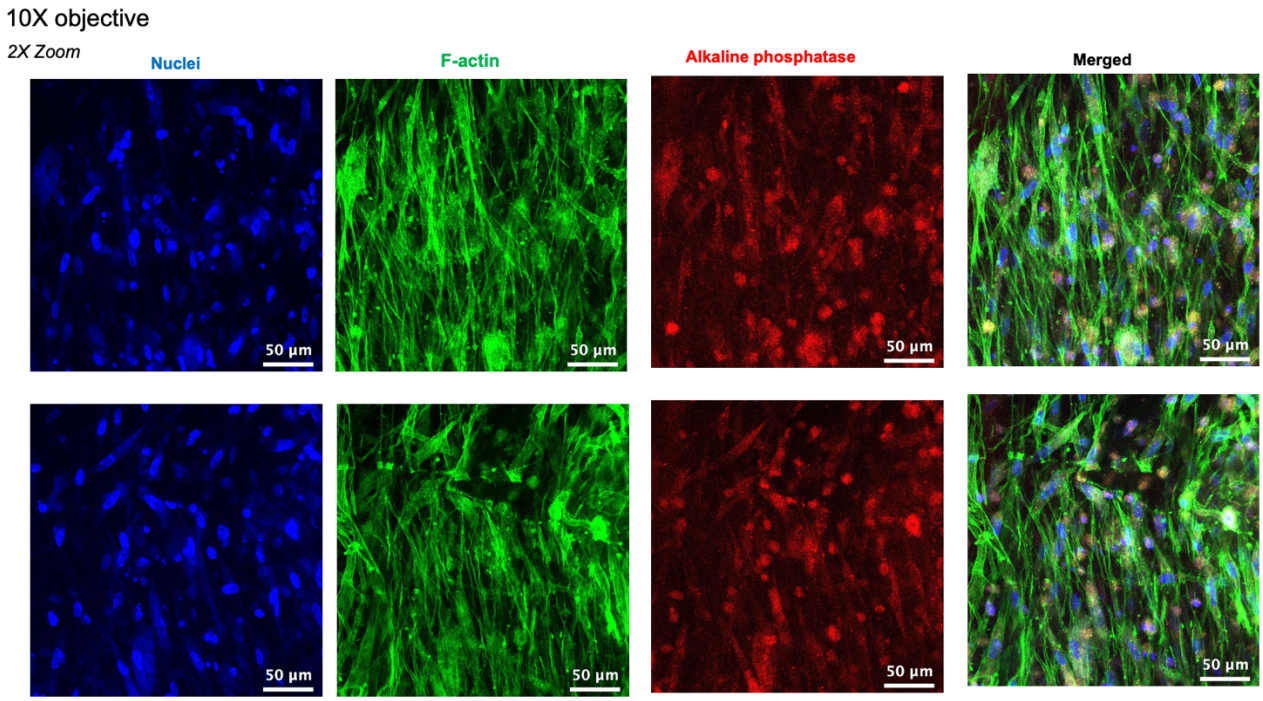


**Figure 4.7. Confocal images of osteoblasts in BBB enthesis region**

appeared more fibrous and enmeshed (Figure 4.6), whereas osteoblastic cells in the BBB enthesis appeared more defined with more prominent and distinctive F-actin stress fibers (Figure 4.7). Confocal imaging of ALP staining also showed more diffuse distribution of ALP in the PDL cell region whereas it appeared more localized to cell surfaces in osteoblasts (Figure 4.8).

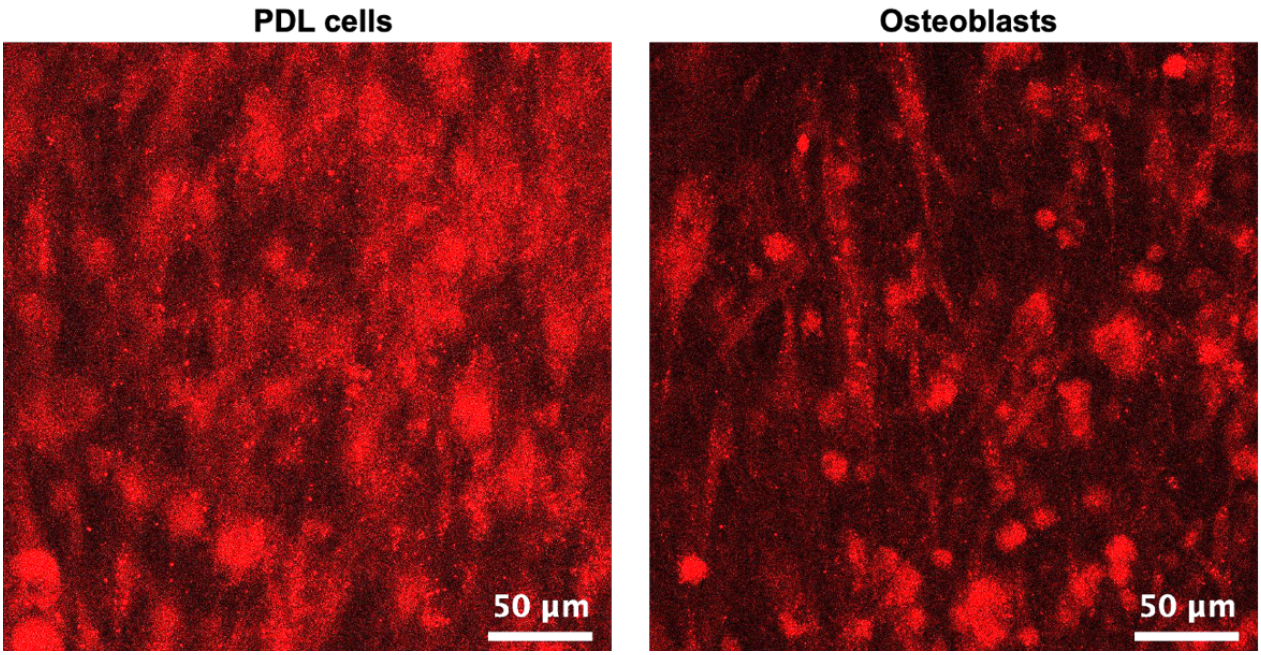


**Figure 4.8. Alkaline phosphatase (ALP) staining of PDL and bone cells.**

Similarly, widefield fluorescence images of PDL cells and osteoblasts in the PPP and BBB controls respectively showed ALP being localized to cell outlines around nuclei and in cytoplasm in osteoblasts (Figure 4.9, Figure 4.10, A), whereas being more diffuse and independent of cell outlines in PDL cells (Figure 4.10, B).

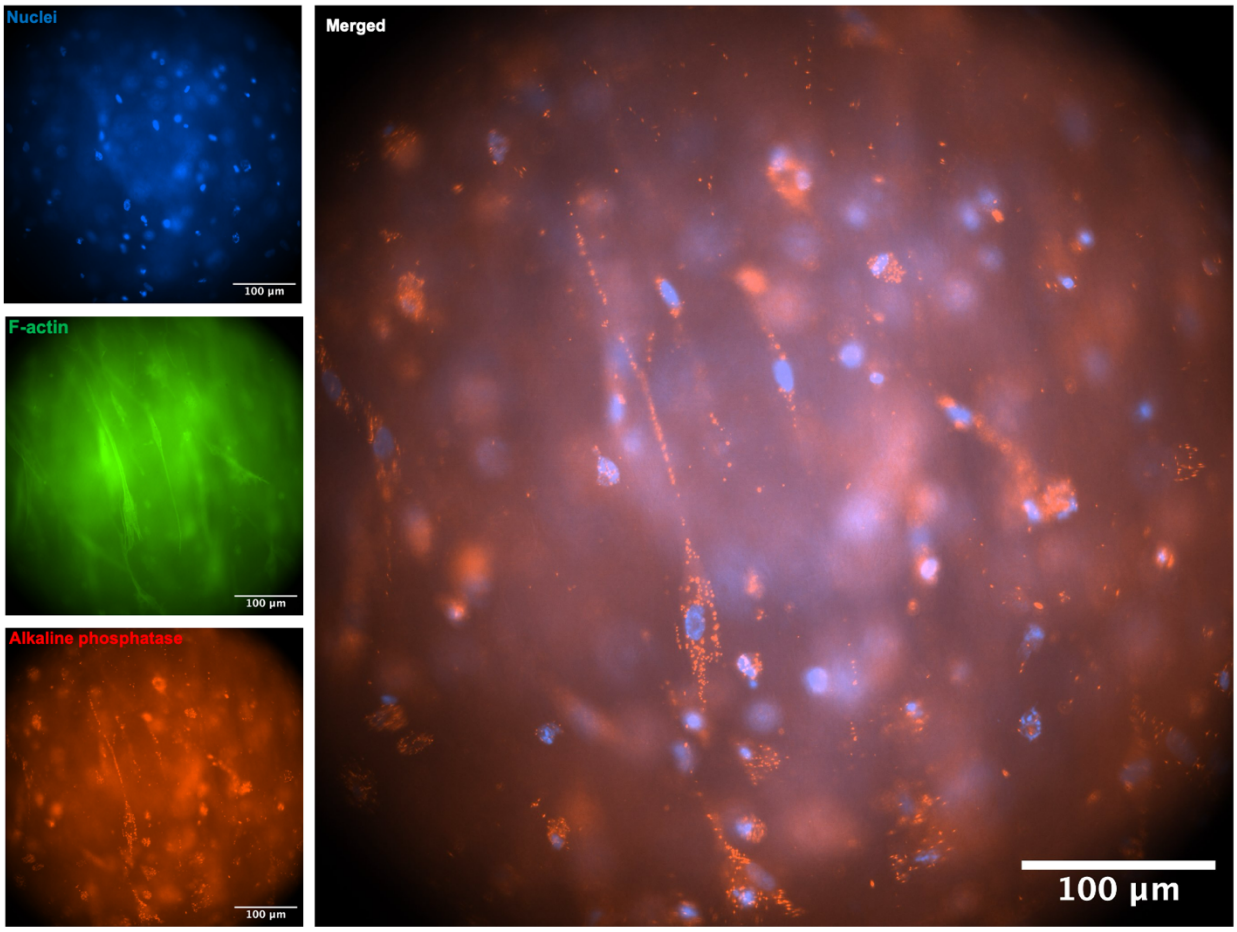


**Figure 4.9. Widefield imaging of osteoblasts in BBB PTCs.** Blue and red channels have been merged in the large image on the right to demonstrate ALP staining localized to cell outlines around nuclei.

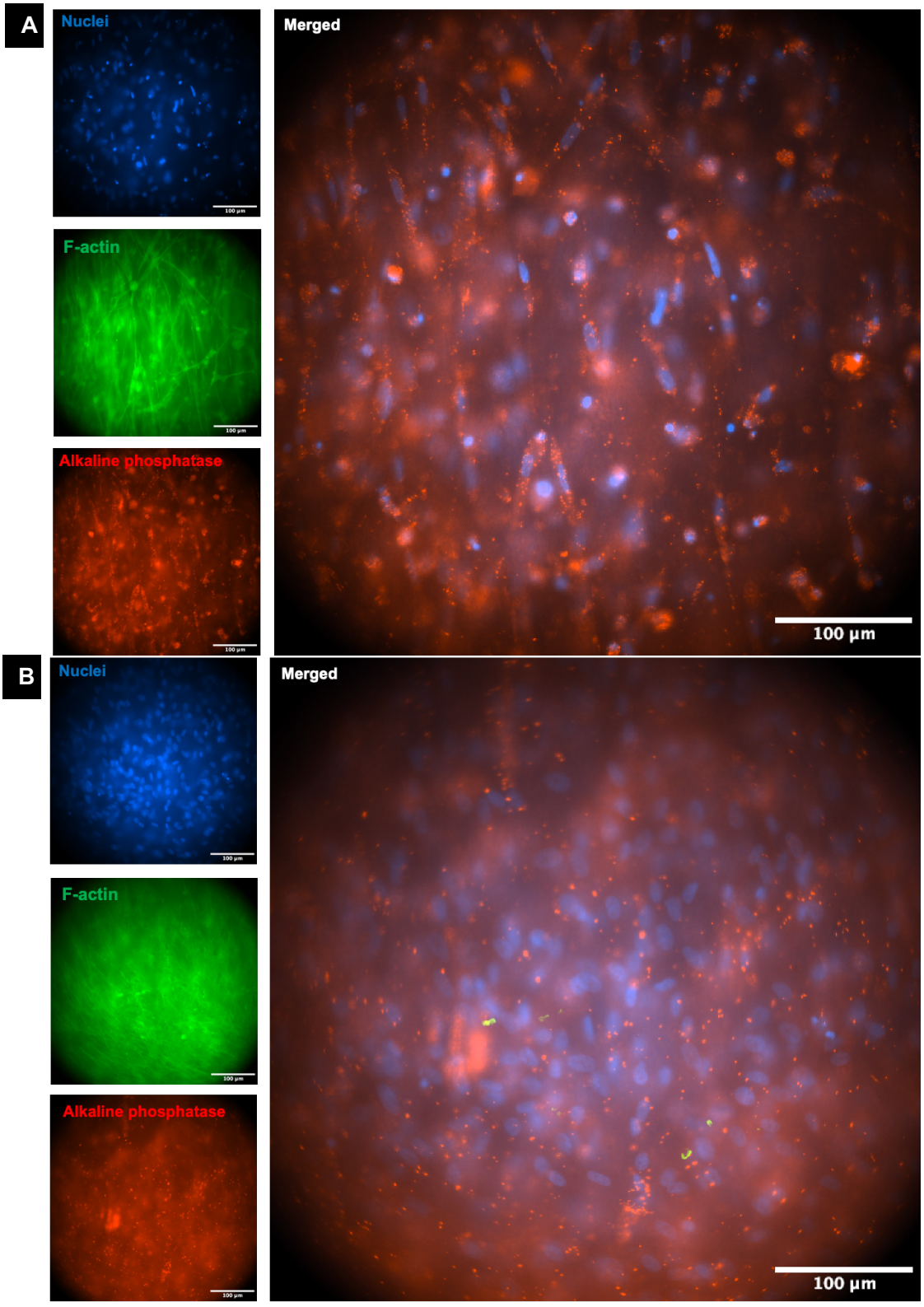


**Figure 4.10. Widefield imaging of osteoblasts in BBB and periodontal cells in PPP control PTCs' mid-region (non-enthesis) .** Blue and red channels have been merged in the larger images to demonstrate ALP staining relative to nuclei. (**A**)Osteoblasts in BBB PTCs. (**B**)Periodontal cells in PPP PTCs.

When the BPB PTCs with both cell types patterned in specific regions were imaged, we observed that both the upper (Figure 4.11) and lower (Figure 4.13) enthesis regions showed a network of cells that were aligned in a parallel fashion to each other along the longitudinal axis of the tissue construct. Imaging of areas limited to PDL cells (Figure 4.12, middle panel) showed aligned and enmeshed cells with finer F-actin fibers. Osteoblasts in the upper and lower regions of the BPB PTCs (Figure 4.12 top and bottom panel) appeared more defined in shape, less aligned and with prominent F-actin fibers, similar to that in BBB PTCs. This parallel arrangement of PDL cells and networked less-aligned arrangement of osteoblasts is also clear in the brightfield microscope images (Figure 4.14). Localization of ALP to cell surface and outlines in osteoblasts as opposed to its tissue-wide non-cell specific distribution in PDL cells is also observed in these images (Figure 4.14).

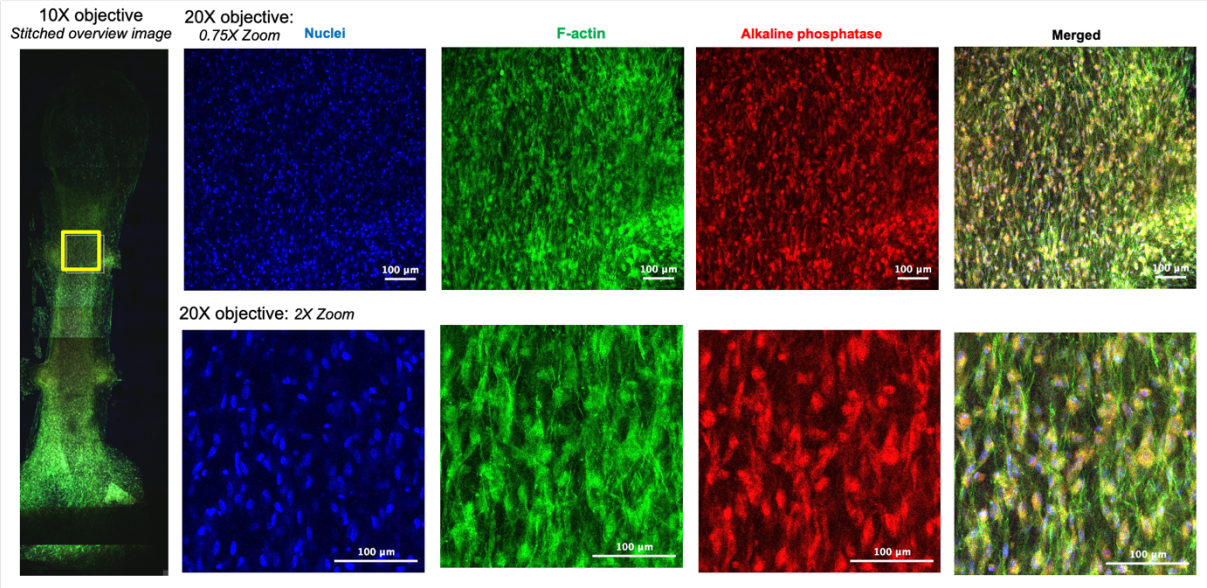


**Figure 4.11. Confocal images of BPB upper enthesis region.**

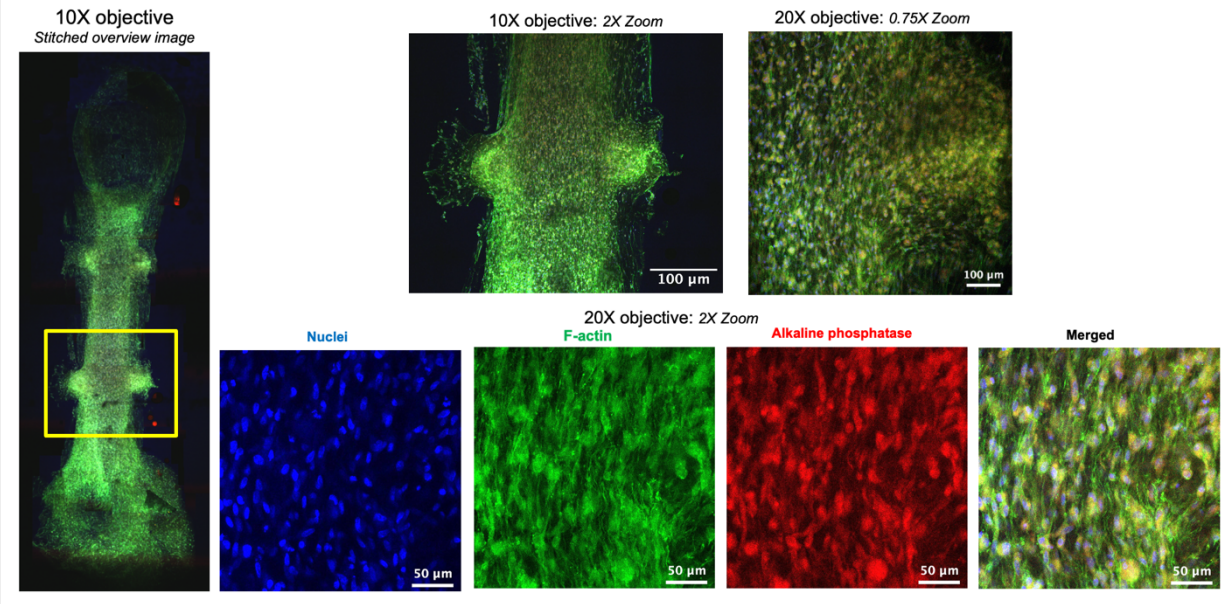


**Figure 4.13. Confocal images of BPB lower enthesis region**

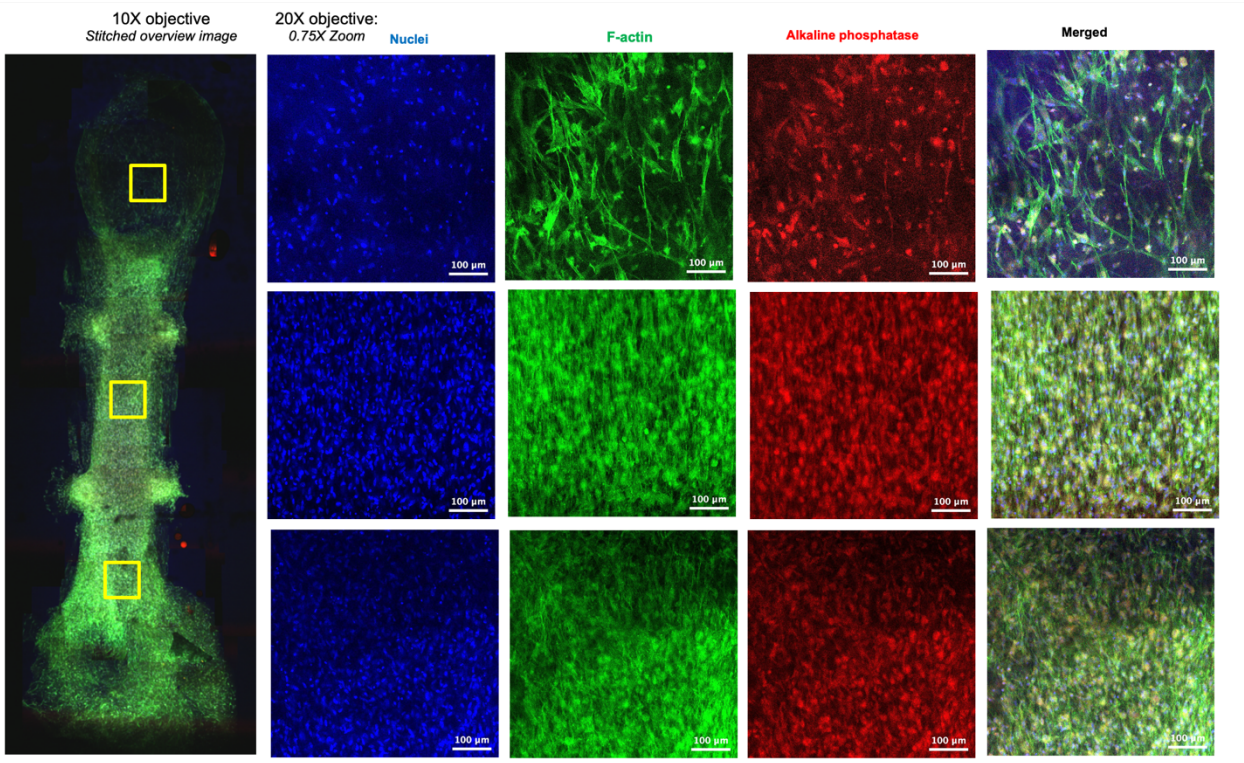


**Figure 4.12. Confocal images of BPB bone and PDL cell regions.** Top panel depicts osteoblasts towards the top end of the BPB PTC, middle panel depicts PDL cells in the mid region and bottom panel depicts osteoblasts in the lower end of the PTC. In the top panel osteoblasts were imaged in an area around the point of attachment of tissue around the silicone post. Hence, the morphology of these cells appear different, due to their sparsity and proximity to the post causing more tensile force generation in them

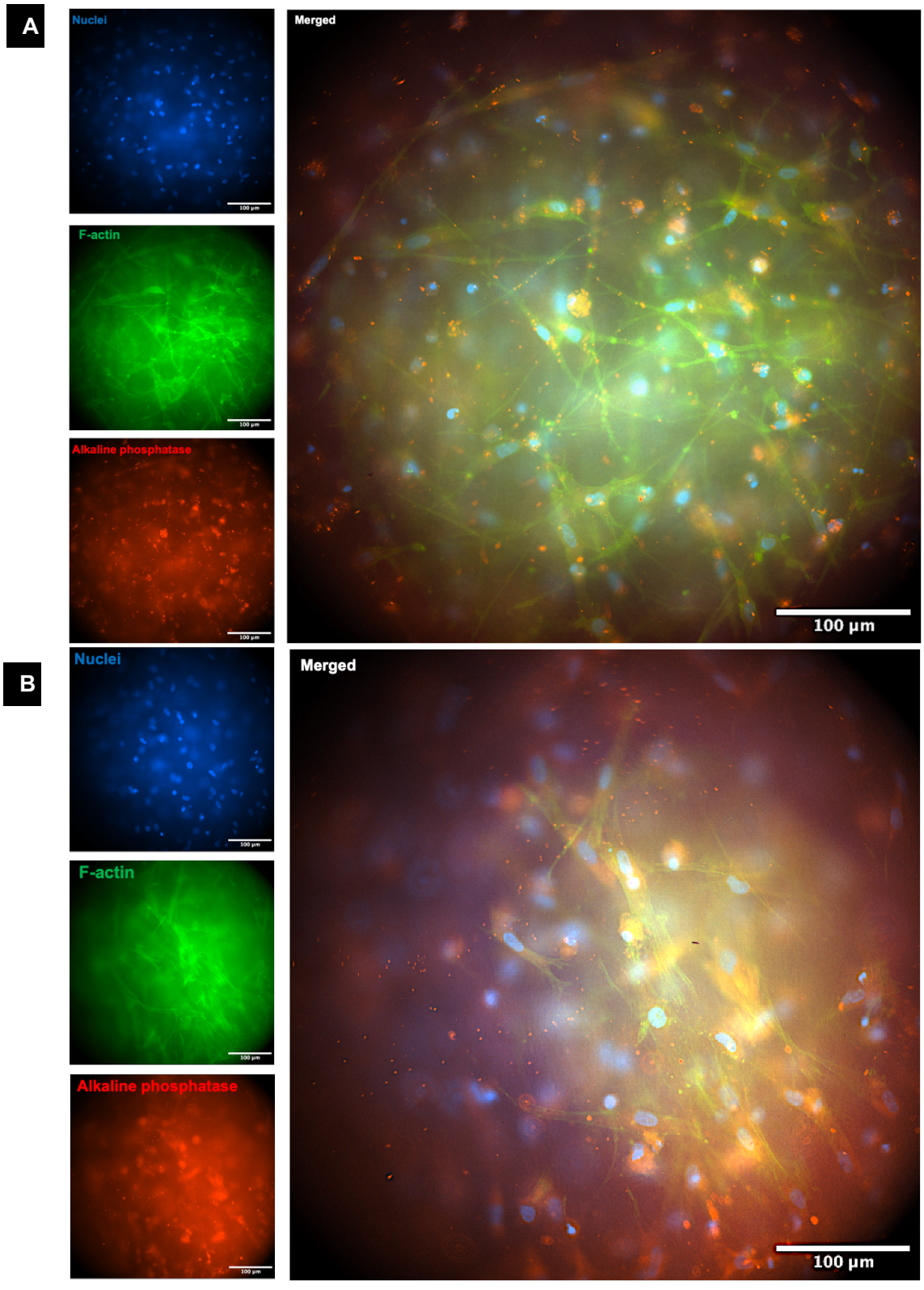


**Figure 4.14. Widefield imaging of osteoblast and periodontal cell regions in BPB PTCs.** Blue, red and green channels have been merged. (**A**) Osteoblasts in bone cell region at the top and bottom areas of BPB PTCs. (**B**) Periodontal cells in the middle PDL region of the PBP PTCs.

## 4.5 DISCUSSION

In this chapter, the development of a spatially patterned 3D *in vitro* tissue construct, using the suspended tissue open microfluidic patterning technique, was demonstrated. Similar to the non-patterned PTCs engineered in Chapter 3, the STOMP PTCs are also suspended between two posts thus also recreating the *in vivo* design feature of cells enmeshed with principal collagen fiber bundles spanning the PDL space. These STOMP PTCs have an added innovation of including disparate cell-types spatially patterned into discrete zones within the 3D tissue model. PDL cells cultured in regular media were patterned in the center of the tissue, whereas osteoblasts resulting from a 10-day treatment of PDL cells with osteogenic induction media were patterned towards both ends of the tissue construct. Comparatively, the PTC model engineered in Chapter 3 had the same PDL cell population distributed throughout the tissue without region-specific localization or patterning of disparate cell-types. The STOMP PTCs represent a step towards designing a biomimetic PDL *in vitro* model. By spatially patterning PDL cells and osteoblasts next to each other, we successfully created the PDL-alveolar bone transition zone or enthesis at a cellular level.

The STOMP devices consisting of a removable patterning rail and holding clips that fit on to a post array, were crucial in generating and maintaining this region-specific localization of cells in a collagen matrix. This study was carried out in collaboration with the Theberge Lab at the University of Washington, Department of Chemistry, where this STOMP technique was developed. The STOMP tissues were generated by pipetting the cell-collagen solutions into the designated areas of the open microfluidic channel of the patterning rail. Surface tension and capillary forces hold the cell-collagen solution within the walls of the open channel of the patterning rail without it dripping or trickling down, until the solution transitions from a fluid to hydrogel state (Lee et al. 2020). Capillary pins in the open microfluidic channels serve to hold and restrain the cell-collagen

solutions in the respective zones they are pipetted in until gelation, thus leading to formation of cell and site-specific, localized zones and the entheses between them.

The STOMP PTCs are a critical advancement in the field of *in vitro* periodontal model systems. Currently no satisfactory *in vitro* 3D model systems exist in the periodontal mechanobiology field which is highly dependent on *in vitro* systems for periodontal mechanistic studies. Hence, 2D systems continue to be the mainstay (Yang et al. 2015). Considering the centrality of 3-dimensional cell-cell and cell-ECM connections in assessing biological mechanisms within the periodontium, our model fills this long-standing gap (Kang et al. 2013). In the quest to engineer physiologically relevant periodontal tissues for i*n vitro* research and for application in *in vivo* periodontal regeneration, newer techniques like bioprinting and microfluidic organ-on-a-chip models are being harnessed (Aveic et al. 2021, Huang et al. 2023). Yet, in our review of literature, we did not come across any *in vitro* models that incorporated geometrically patterned cellular zones and entheses in 3D like our model. This model represents a significant innovation, and it can be harnessed for conducting mechanistic studies, orthodontic research, drug development, genetic studies and for developing biologics for periodontal therapies.

Our *in vitro* cellular enthesis model provides an alternative or addition to animal studies, facilitating scalable, economic and rapid reductionist hypothesis testing compared to animal models. This will be a valuable option since studies on interfaces and entheses in the periodontium have been predominantly or only carried out in animal models (Lin et al. 2017). Additionally, similar to PTCs in chapter 3, the STOMP PTCs could also be explored for *in vivo* transplantation to regenerate the periodontium. Prefabricated *in vitro* PDL grafts with patterned site-specific distribution of cell types as in the STOMP PTCs, will provide the necessary structural organization and cellular paracrine factors needed to regenerate both unmineralized PDL and mineralized alveolar bone areas of the periodontium.

Biological analysis of STOMP PTCs with immunofluorescence imaging revealed phenotype-specific qualitative differences in cellular morphology and stress fiber density and alignment. Imaging of PDL cells in BPB tissues (Figure 4.12, middle panel) revealed cells that were spindle-shaped, aligned and enmeshed with each other. These cells also had F-actin fibers that were thin and arranged parallel to each other in the images. However, the osteoblasts in the bone regions of the BPB PTCs (Figure 4.12, top and bottom panel) appeared more defined or polygonal in shape, less aligned and with prominent F-actin stress fibers. This parallel arrangement of PDL cells and networked less-aligned arrangement of osteoblasts is also well-observed in the brightfield microscope images (Figure 4.14). High density and prominent actomyosin stress fibers were similarly found in osteoblasts resulting from PDL cells treated with osteogenic induction media by Yamamoto et al. 2018. Untreated control PDL cells in this study also had thinner and parallel aligned F-actin stress fibers, identical to that observed in the current study. Thicker actin filaments in differentiated cells and thinner, parallel filaments in undifferentiated mesenchymal stem cells have similarly been observed in other studies as well (Rodriguez et al., 2004; Arnsdorf et al., 2009). These studies have shown that activation of the Rho-ROCK pathway causes stress fiber structure and osteogenic differentiation; similarly, the cells in our patterned PTCs may replicate this phenotype through Rho-ROCK activation. More detailed studies that quantify the cellular and stress fiber parameters and investigate the underlying signaling mechanisms in our STOMP PTCs are needed to corroborate and validate these conclusions.

ALP staining revealed cell-type specific immunofluorescence patterns in STOMP PTCs. The PDL cells showed a diffuse pattern of ALP staining which included both cellular and extra-cellular areas (Figure 4.8, Figure **4.10**, B, Figure 4.14, B). Osteoblasts on the other hand displayed punctate, perinuclear ALP stains, distributed throughout the cytoplasm and confined to cell outlines (Figure 4.8, Figure **4.9**, Figure **4.10**, A, Figure 4.14, A). ALP is an ecto-enzyme i.e. a catalytic protein with its active sites outside the cell. It is covalently bound to phosphatidyl inositol (PI) phospholipid

complexes in the plasma membrane and can be released from the cell membrane by PI-specific phospholipase C. ALPs are expressed in four isoenzyme forms. The first three are tissue-specific with highly restricted expression, comprising of intestinal ALP, placental ALP and germ cell ALP. The fourth isoenzyme is tissue nonspecific alkaline phosphatase (TNAP) which is expressed in wide variety of tissues, but it is especially abundant in the liver, bone, kidney and periodontium (Kawase et al., 1988, Aubin and Liu 1996). TNAP is also expressed on the plasma membrane of osteoblasts, odontoblasts and hypertrophic chondrocytes, while also being highly expressed on the membranes of the matrix vesicles that bud from these cells (Hoshi et al. 1997, Miao et al., 2002). Hence, ALP expression is often used as a marker of differentiated osteoblasts. Our finding of ALP being localized specifically to the perinuclear and cytoplasmic regions of the osteoblasts is consistent with the cell membrane expression of ALP in osteoblasts. However, further studies are needed to confirm and differentiate between cytoplasmic versus cell membrane expression of ALP in the osteoblasts of our model.

PDL cells are known for their ability to produce ALP in levels much greater than cells in other soft connective tissues (Kawase et al. 1988, Yamaguchi et al. 1995). Unlike osteoblasts, we observed that ALP staining pattern of PDL cells was quite diffuse and included both cellular and extra-cellular areas (Figure 4.8, Figure 4.10, B, Figure 4.14, B). This observation may imply that perhaps the cells are secreting the enzymes in the extracellular space or there could be ALP embedded matrix vesicles in the ECM. Two pools of ALP were indeed found by Groeneveld et al. (1996) in their electron microscopy study of the periodontium – one bound to cells and the other associated with the collagenous ECM. Their biochemical data indicated approximately 10% ALP activity was firmly bound to the ECM and the other 90% arose from the plasma membranes. Although ALP is mostly associated with mineralization, it has wide ranging physiological functions (Aubin and Liu 1996). Kawase et al. (1988) hypothesize that the ALP produced by PDL cells might be related to the regulation of mineralization within the periodontium. ALP degrades the inorganic

pyrophosphoric acid that suppresses calcification. The preferential localization of ALP in ECM around PDL cells and on the cell membranes of osteoblasts may relate to ALP's ability to either suppress or initiate mineralization in respective zones by modulating its inhibitory effect on pyrophosphoric acid. Further studies to explore phenotype-specific localization of ALP and its location-specific functions, may provide insight on the long-standing question of how the PDL maintains its non-mineralized state despite its location between two hard tissues.

We have documented the engineering of a multi-layered PTC model. However, the limitations of this study include the fact that characterization of cell types used in the model and quantification of cell structural elements have not been done. These could be carried out in future studies based on this model.

## 4.6 CONCLUSION AND FUTURE DIRECTIONS

In this chapter, we demonstrated the engineering of a spatially patterned 3D *in vitro* tissue construct, using the suspended tissue open microfluidic patterning technique. A PDL-alveolar bone transition zone or enthesis at a cellular level was created by spatially patterning PDL cells and osteoblasts next to each other. This model represents a significant development over existing models, of which most are in 2D.

The patterned PTCs can be utilized for a variety of assays including measurement of contractile forces and studying cell morphology and structural analysis using immunofluorescent staining, as demonstrated in this chapter. Such analyses are necessary to investigate and understand periodontal biology and behavior, thus positioning our model suitably to execute periodontal research projects. For instance, we observed that the contractile force generated by the PPP constructs was highest, followed by that of BPB and BBB tissue constructs, although differences were not statistically significant. We also qualitatively observed differences in periodontal cell and

osteoblast F-actin structure and alkaline phosphatase distribution. To summarize, cell or ECM distribution of ALP was related to osteoblast or PDL phenotype, and these cells were in turn associated with thicker and thinner F-actin filaments respectively. Thus, these observations lead us to develop a hypothesis that differences in actin cytoskeleton structure and alkaline phosphatase function between PDL cells and osteoblasts determine the contractile force generated by each tissue-type. The STOMP model thus can be further used to test this hypothesis and understand how the cytoskeletal machinery and ECM regulation by enzymes like alkaline phosphatase alter cell phenotype and tissue behavior. Additionally, these STOMP PTCs can also be subjected to tensile stretching to investigate mechanical loading effects localized within the zones and interfaces of the disparate cell types, similar to experiments on the unpatterned PTCs in Chapter 3. The PDL-alveolar bone interface is one between a hard and soft tissue. A future objective will be to develop the current model such that the mineralized osteoid tissue interfaces with PDL cells to generate a biomimetic model. A graded transition of physical properties and cellular composition to mimic *in vivo* PDL behavior, will also be a goal.

## 4.7 REFERENCES

Arnsdorf, E.J., Tummala, P., Kwon, R.Y., Jacobs, C.R., 2009. Mechanically induced osteogenic differentiation—the role of RhoA, ROCKII and cytoskeletal dynamics. J Cell Sci. 122, 546–553.

Aubin JE, Liu F. The osteoblast lineage. In Principlesof Bone Biology. Edited by J.P. Bilezikian, L.G. Raisz, and G.ARodan. 1996. Academic Press, San Diego. pp. 51–67.

Aveic S, Craveiro RB, Wolf M, Fischer H. Current Trends in In Vitro Modeling to Mimic Cellular Crosstalk in Periodontal Tissue. Advanced Healthc Mater. 2021;10(1):2001269.

Galli M, Yao Y, Giannobile WV, Wang HL. Current and future trends in periodontal tissue engineering and bone regeneration. Plast Aesthet Res. 2021;8.

Groeneveld MC, Van den Bos T, Everts V, Beertsen W. Cell-bound and extracellular matrix-associated alkaline phosphatase activity in rat periodontal ligament. J Periodontol Res. 1996;31(1):73-9.

Hoshi K, Amizuka N, Oda K, Ikehara Y, Ozawa H: Immunolocalization of tissue non-specific alkaline phosphatase in mice. Histochem Cell Biol 1997; 107: 183—191.

Huang L, Liu B, Cha JY, Yuan G, Kelly M, Singh G, Hyman S, Brunski JB, Li J, Helms JA. Mechanoresponsive properties of the periodontal ligament. J Dent Res. 2016;95(4):467-75.

Kang KL, Lee SW, Ahn YS, Kim SH, Kang YG. Bioinformatic analysis of responsive genes in two-dimension and three- dimension cultured human periodontal ligament cells subjected to compressive stress. J Periodontal Res 2013;48(1):87–97.

Kawase T, Sato S, Miake K, Saito S. Alkaline phosphatase of human periodontal ligament fibroblast-like cells. Adv Dent Res. 1988;2(2):234-9.

Lee UN, Day JH, Haack AJ, Bretherton RC, Lu W, DeForest CA, Theberge AB, Berthier E. Layer-by-layer fabrication of 3D hydrogel structures using open microfluidics. Lab Chip. 2020;20(3):525-36.

Lin JD, Jang AT, Kurylo MP, Hurng J, Yang F, Yang L, Pal A, Chen L, Ho SP. Periodontal ligament entheses and their adaptive role in the context of dentoalveolar joint function. Dent Mater. 2017;33(6):650-66.

Miao D, Scutt A: Histochemical localization of alkaline phosphatase activity in decalcified bone and cartilage. J Histochem Cytochem 2002; 50: 333—340.

Rodriguez, J.P., Gonzalez, M., Rios, S., Cambiazo, V., 2004. Cytoskeletal organization of human mesenchymal stem cells (MSC) changes during their osteogenic differentiation. J. Cell. Biochem. 93, 721–731.

Yamaguchi M, Shimizu N, Shibata Y, Abiko Y. Effects of different magnitudes of tension-force on alkaline phosphatase activity in periodontal ligament cells. J Dent Res. 1996;75(3):889-94.

Yamamoto T, Ugawa Y, Yamashiro K, Shimoe M, Tomikawa K, Hongo S, Kochi S, Ideguchi H, Maeda H, Takashiba S. Osteogenic differentiation regulated by Rho-kinase in periodontal ligament cells. Differentiation. 2014;88(2-3):33-41.

Yang L, Yang Y, Wang S, Li Y, Zhao Z. In vitro mechanical loading models for periodontal ligament cells: From two-dimensional to three-dimensional models. Arch Oral Biol. 2015;60(3):416–424.doi:10.1016/j.archoralbio.2014.11.012.

# CHAPTER 5. SUMMARY AND FUTURE DIRECTIONS

## 5.1 SUMMARY AND FUTURE DIRECTIONS

Investigating the mechanical and biochemical pathways that regulate periodontal cellular and tissue behavior, is essential for developing and improving clinical interventions in periodontal and orthodontic fields. Due to the sheer number of biological pathways and mediators involved, and their complex inter-relationships, the study of periodontal mechanobiology becomes very challenging. Hence, bioengineering modalities to develop *in vitro* PDL models are being increasingly employed in periodontal research to investigate cellular response to mechanical loading (Li et al. 2019). Reductionist approaches at both single cell level and 3D tissue levels are necessary to integrate mechanistic insights on periodontal behavior for clinical problem solving.

In chapter 2, using the novel reference-free traction-free microscopy technique, black dots, I have quantified single cell contractile forces of periodontal cells for the first time. This technique also facilitated characterization of stress fibers and differentiating between cell phenotypes based on their contractile force. Considering the importance of F-actin structure, composition and tension in determining fate and function (McBeath et al. 2004, Putra et al. 2023), these findings add critical new information to the periodontal field. Using the BD technique, we were also able to demonstrate effects of the important inflammatory mediator TNF-$\alpha$ on myofibroblast differentiation and the actin cytoskeleton. These findings can be used to regulate the progenitor role played by aSMA positive cells to differentiate into osteoblasts, cementoblasts, and periodontal ligament fibroblasts (Meng et al. 2010, San Miguel et al. 2010, Roguljic et al. 2016, Matthews et al. 2020). This can have potential applications to regenerate desired periodontal layers and to also initiate or inhibit orthodontic tooth movement.

In chapter 3 I have engineered a 3D *in vitro* PDL model that has two important features – 1) it recapitulates key elements of native periodontal architecture and 2) it includes a magnet-based tensile stretching system to assess effects of mechanical loads on periodontal tissue. Our innovative platform is a first of its kind 3D PDL model that facilitates exploration of macro-scale tissue behavior and its links with underlying structural changes. We have demonstrated effects of tensile stretching that included collagen remodeling by cells, increase in cell count, increase in F-actin production and expression of myofibroblasts using our model system. Our model also facilitates convenient and direct measurement of tissue-generated contractile force, thus enabling studies on biomechanical and viscoelastic periodontal tissue behaviour. In the present study we have applied continuous, uniaxial tensile stretch. With further experimentation our model can be suitably modified to either apply cyclic tensile stresses or compressive force.

PTC models with varying ECM stiffnesses can be cast by modifying the collagen matrix concentration to explore ECM-stiffness and tissue contractile force based cell phenotype determination. Mapping stiffness or force values to their cell differentiation effects is a powerful tool to elicit clinical need-based directed cell differentiation such as either osteogenic or osteoclastogenic response within the periodontium. This has profound translational implications for a host of clinical issues including for repair and regeneration of periodontitis-afflicted tissues, determination of optimum orthodontic force to effectuate tooth movement, retention after orthodontic treatment and implant osseointegration. Thus, this PDL model has multi-purpose research applications and translational potential. With the molecular level configurations embodying the physiologic cell-ECM architecture, we can expect that our model would recapitulate the cellular behavior patterns expected in native tissue with greater accuracy than existing models.

In chapter 4, I used the suspended tissue open microfluidic patterning (STOMP) system to create a spatially patterned 3D tissue construct of the periodontal ligament using two different cell types. The two cell types were– a) PDL cells obtained from extracted premolars of healthy patients, and b) osteoblastic cells obtained by treating PDL cells with osteogenic induction medium. I was able to create a bone-PDL-bone tissue construct model and cellular entheses between the periodontal and bone cell layers. Reproducing this multi-layered configuration along with the entheses between the layers is a critical step towards building a biomimetic 3D *in vitro* PDL model. Additionally, such a model, with region-specific pre-assembly and priming of cells in a 3D matrix, has also been long sought as a transplantation graft for *in vivo* periodontal regeneration. Hence, the regenerative capacity of this model can be further tested and developed using animal models. This model represents a significant innovation, and it can be harnessed for conducting mechanistic studies, orthodontic research, drug development, genetic studies and for developing biologics for periodontal therapies. Another future objective will be to develop the current model such that the mineralized osteoid tissue interfaces with PDL cells to generate a biomimetic model. A graded transition of physical properties and cellular composition to mimic *in vivo* PDL behavior, will also be a goal.

Overall, my research has demonstrated how bioengineering techniques can be harnessed to study periodontal cell structure, mechanical properties, function and behavior at both single cell and 3D levels. The data from these studies can be used to develop directed cell differentiation techniques by targeting cell structural elements. This has utility for regenerating specific periodontal layers and to accelerate tooth movement during orthodontic treatment and inhibiting tooth movement during the retention phase of orthodontics. Future studies to establish stronger links between cell structure and function are warranted to be able to develop the directed cell differentiation modality for clinical applications.

## 5.2 REFERENCES

Matthews BG, Wee NK, Widjaja VN, Price JS, Kalajzic I, Windahl SH. αSMA osteoprogenitor cells contribute to the increase in osteoblast numbers in response to mechanical loading. Calcif Tissue Int. 2020;106(2):208-17.

McBeath R, Pirone DM, Nelson CM, Bhadriraju K, Chen CS. Cell shape, cytoskeletal tension, and RhoA regulate stem cell lineage commitment. Dev Cell. 2004;6(4):483-95.

Meng Y, Han X, Huang L, Bai D, Yu H, He Y, Jing Y. Orthodontic mechanical tension effects on the myofibroblast expression of alpha-smooth muscle actin. The Angle Orthodontist. 2010;80(5):912-8.

Putra VD, Kilian KA, Knothe Tate ML. Biomechanical, biophysical and biochemical modulators of cytoskeletal remodelling and emergent stem cell lineage commitment. Commun Biol. 2023;6(1):75.

Roguljic H, Matthews BG, Yang W, Cvija H, Mina M, Kalajzic I. In vivo identification of periodontal progenitor cells. J Dent Res. 2013;92(8):709-15.